7-2015

Fundamental Studies of Magnetoconvective Forces and Density Gradients in a Microfluidic Environment

Adam James Kreidermacher
University of Arkansas, Fayetteville

Fundamental Studies of Magnetoconvective Forces and Density Gradients in a

Microfluidic Environment

A dissertation submitted in partial fulfillment
of the requirements for the degree of
Doctor of Philosophy in Chemistry

by

Adam Kreidermacher
Saint Mary's University of Minnesota
Bachelor of Arts in Chemistry, 2008

July 2015
University of Arkansas

This dissertation is approved for recommendation to the Graduate Council.

_____
Dr. Ingrid Fritsch
Dissertation Director

_____   _____
Dr. Colin Heyes   Dr. David Paul
Committee Member   Committee Member

_____
Dr. Steve Tung
Committee Member

Abstract

Magnetoconvection is a promising phenomenon for developing new electrochemical-based microfluidic flow devices with unique capabilities, such as easily switching flow direction and adjusting flow speeds and flow patterns as well as avoiding bubble formation. In order to develop these devices it is necessary to study the underlying forces. Four contributions toward fluid flow were considered. The first and foremost is the magnetohydrodynamic force ($\mathbf{F_B}$), which is the magnetic component of the Lorentz force and governed by the right hand rule. It generates the majority of the convention, and is the most well-known. The second is the gravitational force ($\mathbf{F_g}$), which causes convection under non-uniform solution density. In electrochemical systems, it is induced by the change in solution composition near an anode or cathode caused by the oxidation or reduction of electroactive species. The third is the magnetic gradient force ($\mathbf{F_{\nabla B}}$), and is present when there are paramagnetic species, which are easily produced in electrochemical systems, and a non-uniform magnetic field. The fourth is the paramagnetic concentration gradient force ($\mathbf{F_{\nabla C}}$), the magnitude of which lies in controversy. To study these forces, a solution containing microbeads and redox species were placed in an electrochemical cell, and fluid motion was monitored with bead video microscopy in presence and absence of an externally applied magnetic field. To study density gradients, the ferricyanide-ferrocyanide redox couple was used without a magnet. To study all the forces, the effect on fluid flow in the presence and absence of a magnet during deposition and stripping at electrodes in solutions containing paramagnetic Cu(II) and diamagnetic Pb(II) ions was performed.

Acknowledgements

I would like to thank my family for their support over the years.

I would like to thank my advisor Dr. Ingrid Fritsch for giving me advice during my research and while writing this dissertation. I would also like to thank my committee members, Dr. David Paul, Dr. Colin Heyes, and Dr. Steve Tung for their input during committee meeting.

I would like to thank Dr. Feng Gao for his work on the FCS experiments.

I would like to thank Dr. Anupama Aggarwal, Dr. Vishal Sahore, and Menja Hu for the fabrication of the microelectrode array chips.

Table of Contents

List of published papers

Chapter 3: 3D Imaging of Flow Patterns in an Internally-Pumped Microfluidic Device: Redox Magnetohydrodynamics and Electrochemically-Generated Density Gradients

This chapter was published as:

F. Gao, A. Kreidermacher, I. Fritsch, C.D. Heyes, 3D Imaging of Flow Patterns in an Internally-Pumped Microfluidic Device: Redox Magnetohydrodynamics and Electrochemically-Generated Density Gradients, Analytical Chemistry, 85 (2013) 4414-4422.

1. Introduction to Density Gradients and Magnetoconvective Forces

1.1 Introduction

Microfluidics is the handling of small volumes of fluids on the microliter to picoliter scale. It is used for developing small-scale, automated devices for miniaturized total analysis systems or lab-on-a-chip applications like assays, separations, and drug discovery [1, 2]. It has the advantages of reduced reagent and energy consumption as well as increased portability [3].

There are several ways to pump fluids in microfluidics. Mechanical pumps, like syringe and peristaltic pumps are one type. They are difficult to miniaturize because of the need to fabricate moving parts [1]. Switching the direction of flow is difficult with mechanical pumps and often requires valves. Electrokinetic pumping applies an electric field to cause flow. However, flow rates are dependent on the physicochemical properties of the channel walls and high voltages are required (up to 5 KV) [4], which can cause bubble formation due to oxidation and reduction of water [5, 6].

A different approach, using magnetic fields to induce magnetoconvection, provides unique possibilities for the manipulation of fluid flow on a chip [7]. The problem is that until recently it had not been studied in small volumes confined to dimensions like those of lab-on-a-chip devices. Previous work by others to develop micropumps makes use of the magnetic portion of the Lorentz force, the magnetohydrodynamic (MHD) force ($\mathbf{F_B}$), but those studies suffer from bubble formation and electrode corrosion [8].

One way to avoid bubble formation and electrode corrosion in magnetoconvection systems is the use of an alternating $\mathbf{j}$ and magnetic field, called AC MHD. In principal, charging of the electrode's double layer results in migration of ions in solution, creating the $\mathbf{j}$ vector, but requires continual variation of potential or current and the magnetic field (in phase with the

current) to sustain unidirectional fluid flow. Studies of AC MHD have been reported that still generate bubbles from the electrolysis of water because those require an amplitude of the potential as high as 20 V to achieve reasonable flow rates. Using a higher frequency produces higher current for lower potentials and therefore can eliminate bubble formation, but can cause inductive heating [9-11].

The addition of redox species resolved the issue of bubble formation, and can be used with microelectrodes [12, 13]. Work in our laboratory has improved on this by using redox MHD in small volumes, and is ongoing, showing the ability to produce flat flow profiles [14] and stirring [15]. Our laboratory has shown that convection due to redox-MHD is useful in enhancing trace metal analysis [16-18], can be used to pump fluids in a microchannel [19, 20], and can pump a fluid plug on a chip without requiring channel sidewalls [21, 22]. The primary force driving convection in redox-MHD experiments is $\mathbf{F_B}$. The equation for it is shown in Figure 1, where $\mathbf{j}$ is the ionic current density, and $\mathbf{B}$ is the magnetic flux density.

Positive $\mathbf{j}$ is defined as the direction of movement of positive ions. When positive and negative ions are moving in opposite directions they have an additive affect. The ion flux can be generated by electron transfer reactions at the electrodes. Without added electroactive species, the only available electron transfer reaction is the electrolysis of solvent, producing bubbles, oxidation of anode electrode materials, leading to corrosion, or reduction or oxidation of background electrolyte with large overpotentials. Two co-planar band electrodes, one serving as working electrode and the other as counter electrode in the presence of a magnetic field perpendicular to the plane of the electrodes (as shown in Figure 1) can provide linear flow between the working and counter due to $\mathbf{F_B}$ [14, 23].

3
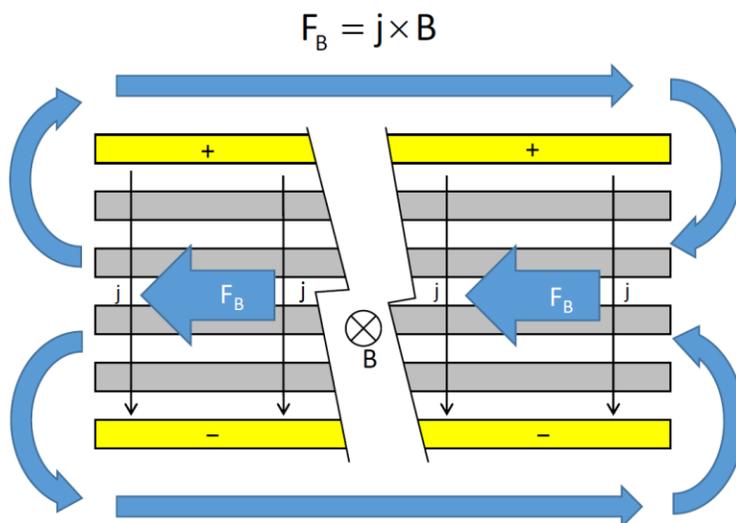
Figure 1. Diagram of magnetohydrodynamics in the reinforcing flow configuration. The two outer electrodes (yellow) of a coplanar, parallel band array are oppositely biased (one as cathode and one as anode), and produce a current $\mathbf{j}$. The array lies on a magnet with field, $\mathbf{B}$, pointing downward. A force, $\mathbf{F_B}$, and therefore fluid flow, is generated between and parallel to the activated electrodes. Equation for $\mathbf{F_B}$ shown.

Monitoring fluid movement during redox MHD experiment can give us valuable insight into how the other magnetoconvective, and electrochemically generated density gradient based forces generate convection. These three forces, which include the gravitational force ($\mathbf{F_g}$), the magnetic gradient force ($\mathbf{F_{\nabla B}}$), and the paramagnetic concentration gradient force ($\mathbf{F_{\nabla C}}$) can produce convection under experimental conditions that also produce $\mathbf{F_B}$.

We have recently demonstrated the use of microspheres or microbeads to track fluid flow in small, confined volumes on a chip during redox-MHD and consequently have discovered interesting effects on fluid motion [23-25]. With this ability we are now in a position to quantitatively study these other forces in the microfluidics environment, as well, which until now have been only minimally addressed. If we can obtain quantitative information, it would allow us to predict how they will influence fluid flow in small volumes.
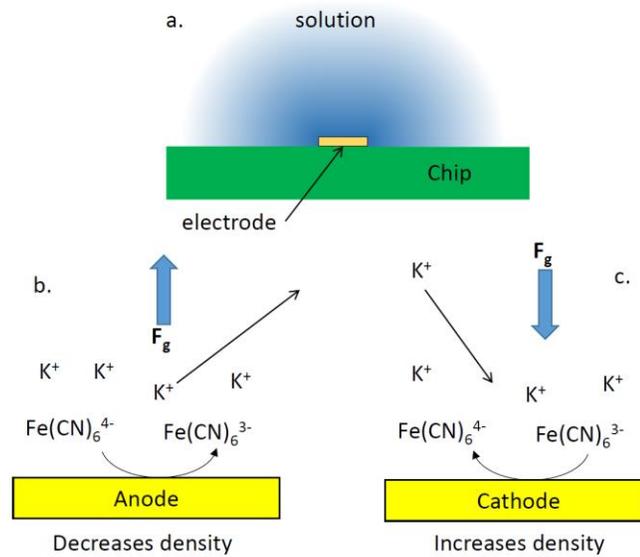
Figure 2. Development of diffusion layer upon electrochemical conversion at an electrode in solution containing redox species, such as $Fe(CN)_6^{4-}$ and $Fe(CN)_6^{3-}$ in an electrolyte like KCl. (a) Overall view of production of a species (blue) at the electrode and its diffusion outward from the electrode. (b) Illustration of how density gradients develop as a result of the electrochemical conversion. In the case of a solution containing $Fe(CN)_6^{4-}$ and $Fe(CN)_6^{3-}$, the volume element becomes less dense at the anode as a net movement of K^+ migrates away and it becomes more dense at the cathode as a net movement of K^+ migrates toward the electrode to compensate charge.

$\mathbf{F_g}$ in electrochemical systems is created in the diffusion layer when the oxidation or reduction changes the charge on an electroactive species. Ions then move in or out to compensate for the change in charge. If ions move in to compensate charge (because an electroactive species of higher charge is produced), then density of that fluid element increases (and neighboring fluid elements decrease in density). If ions move away (because an electroactive species of lower charge is produced), then density of that fluid element decreases (and vice versa for the neighboring fluid elements). Fluid movement created by density gradients is called natural convection. Thermally induces density gradients are also capable of producing convention in microfluidic systems. They been characterized and used to perform polymerase chain reactions by Krishnan et. al. [26] Often the onset of natural convection is delayed from when the current is

first applied. This is due to the fact that the gradients must build up so they are strong enough to overcome the viscous dampening. Previous work in heterogeneous, electrochemical solution based systems used disk microelectrodes in large volumes [27-29]. The effects of natural convection have also been simulated to generate concentration profiles that resemble experimental results [29]. In addition, studies were performed with a coplanar, concentric disk and ring electrodes on a microfluidic chip shows horizontally moving solution converging to a point at the disk electrode [30]. However, the impact of different shapes on natural convection has not been addressed. Band microelectrodes were chosen here to investigate this phenomenon further, because they primarily produce parallel ion movement toward the electrode edge caused by a two-dimensional (2D) mass transport pattern, when looking at the center of the long edge of the electrode, rather than the radially inward or outward convention caused by a three-dimensional (3D) mass transport pattern of a disk electrode. This makes the resulting parallel fluid flow of a band electrode easier to quantify than at a disk.

The ability to monitor density gradients is important not only to understand the effects of natural convection resulting from electrochemical detection in microfluidic devices for analysis, but also to explore the gradient forces of $\mathbf{F_{\nabla C}}$ and $\mathbf{F_{\nabla B}}$. The focus here is using density gradients for this latter purpose. These two gradient forces can be most easily studied by offsetting other forms of convection, such as those due to $\mathbf{F_g}$ and $\mathbf{F_B}$. An example of this strategy has been demonstrated by Leventis and Gao [31]. The challenge will be to design conditions to vary the relative magnitude of the different forces and their directions in order to study their effects.

The interaction between paramagnetic particles and a non-uniform magnetic field causes $\mathbf{F_{\nabla B}}$. It can be described by the equation in Figure 3 [7], where C_p is the paramagnetic species

6

concentration, N_A is Avogadro's number, m^* is magnetic moment of the paramagnetic species, k is Boltzmann constant, and T is the temperature. Due to the term $(\mathbf{B \cdot \nabla})\mathbf{B}$ in the equation, $\mathbf{F_{\nabla B}}$ has a complicated relationship with $\mathbf{B}$, but $\mathbf{F_{\nabla B}}$ usually points towards the higher magnetic flux density. This can be seen in Figure 3 which shows the magnitude and direction of $\mathbf{F_{\nabla B}}$ with respect to different locations around a disk magnet.
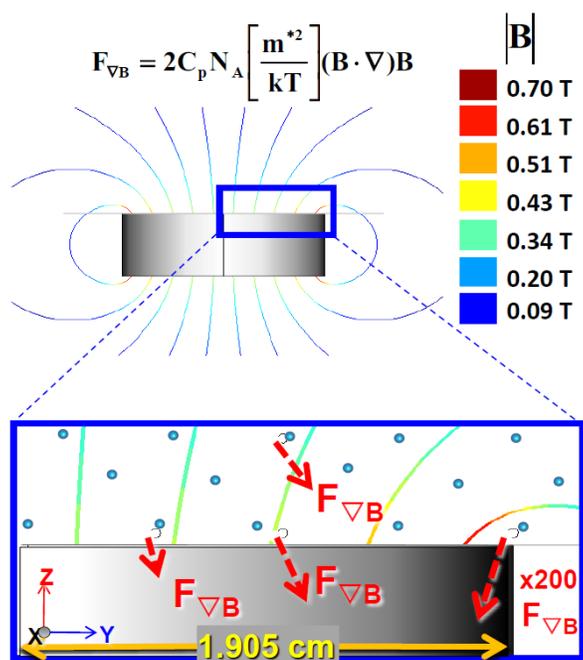
Figure 3. The magnetic field gradient force ($\mathbf{F_{\nabla B}}$) acts on fluid containing paramagnetic species with uniform concentration. The magnitude of B is scaled by color for different field lines in the y-z plane for a NdFeB disk magnet. Relative magnitudes of $\mathbf{F_{\nabla B}}$ vectors are shown to-scale by length and with multiplier where indicated. Used with permission from M.C. Weston, M.D. Gerner, I. Fritsch, Magnetic Fields for Fluid Motion, Analytical Chemistry, 82 (2010) 3411-3418. Copyright 2010 American Chemical Society.

It has been proposed that a non-uniform concentration of paramagnetic species, which occurs between the electrode and bulk solution during a one-electron heterogeneous electron transfer event in electrochemical conversion, will interact with a magnetic field to create $\mathbf{F_{\nabla C}}$. The paramagnetic species are drawn toward the highest concentration by the force $\mathbf{F_{\nabla C}}$ [31].

This force is defined by the equation in Figure 4 [7]. The magnitude and direction of $\mathbf{F}_{\nabla C}$ in a

non-uniform concentration of paramagnetic species can be seen in Figure 4. However, there is

controversy in the literature over the magnitude of this force. Experimental results have been

interpreted to demonstrate both its impact [31, 32], and lack of impact [33, 34].
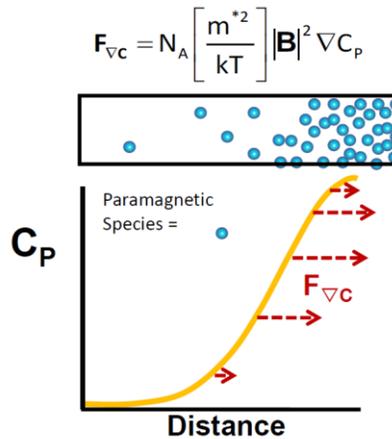
Figure 4. The concentration gradient force ($\mathbf{F}_{\nabla C}$) acts on fluid containing non-uniform concentration of paramagnetic species and is independent of magnetic field direction. The relative magnitudes and directions for $\mathbf{F}_{\nabla C}$ at different locations along the concentration gradient are drawn to-scale for a uniform B field (not shown). Reprinted with permission from M.C. Weston, M.D. Gerner, I. Fritsch, Magnetic Fields for Fluid Motion, Analytical Chemistry, 82 (2010) 3411-3418. Copyright 2010 American Chemical Society.

Magneto convective forces, particularly $\mathbf{F}_B$ have been studied previously using the

ferricyanide-ferrocyanide redox couple. One form, ferricyanide, is paramagnetic, the other form,

ferrocyanide, diamagnetic As a result, $\mathbf{F}_{\nabla B}$ and $\mathbf{F}_{\nabla C}$ only effect ferricyanide. The magnitude of

$\mathbf{F}_{\nabla B}$ is proportional to the ferricyanide concentration, and $\mathbf{F}_{\nabla C}$ points towards the higher

ferricyanide concentration.

Alternatives to Ferricyanide-ferrocyanide are copper and lead deposition and stripping.

the velocity of microbeads added to the solution were monitored while experiments with the two

metals were performed under different conditions. Copper and lead were chosen because oxidation of the metal to the ionic species, the highest concentration gradients of ions will be produced experimentally, presumably providing the largest gradient forces, as well. Because Cu(II) is paramagnetic and Pb(II) is diamagnetic, the forces $\mathbf{F_{\nabla C}}$ and $\mathbf{F_{\nabla B}}$ should be significant only in the Cu(II) solutions in the presence of a magnetic field, where only the latter requires a non-uniform magnetic field. $\mathbf{F_{\nabla C}}$ and $\mathbf{F_{\nabla B}}$ are present in Pb(II) solutions, but it is orders of magnitude weaker and in the opposite direction, in this case it can be assumed that $\mathbf{F_{\nabla C}}$ and $\mathbf{F_{\nabla B}}$ do not affect fluid movement in Pb(II) solutions. Further insight is possible by comparing bead movement when the current is on to movement after it is turned off when the forces $\mathbf{F_{\nabla C}}$, $\mathbf{F_{\nabla B}}$, and $\mathbf{F_g}$ persist after the current and $\mathbf{F_B}$ have ended. $\mathbf{F_g}$ and $\mathbf{F_{\nabla C}}$ will continue until convection and diffusion create a homogenous solution. This particular effect has not been employed previously. Also, $\mathbf{F_g}$ is different from the other forces due to the fact that no magnetic field is required.

It is important to consider different approaches to study magnetoconvective forces by following fluid movement with beads added to the solution. Particle image velocimetry (PIV) is a common method. With PIV a laser illuminates beads in a single plain using florescence or light scattering. The illuminated beads can be tracked using PIV [35] or single particle tracking velocimetry (PTV) analysis. Guidelines for and the use of PIV to follow fluid flow have been reviewed [36, 37]. The emphasis in PIV has been on two-dimensional visualization. To get an accurate velocity measurement the particle has to travel three times the particles diameter, and resolution is limited as a result. Very high spatial resolution (1 μm) has been demonstrated using 0.2 μm particles by Meinhart et al. [38], but more typical PIV measurements are limited to 1 μm

particles and as a result poorer resolution (see ref [39] and references within). Another method is bead video microscopy. In bead video microscopy all the beads in the solution are illuminated, but only the beads in the focal region are tracked by PIV software. Bead movement recorded with bead video microscopy can be analyzed using PIV software, however. A limitation of PIV and bead video microscopy is that movement is measured in 2D and any movement out of the focal plane of the microscope cannot be measured. An approach that can measure 3D movements is fluorescence correlation spectroscopy (FCS). This works by monitoring a focal region of about 0.3 μm in the x and y directions and 1 μm in the z direction. When a fluorescent bead enters the focal region of the excitation beam, the fluorescence increases, when it leaves, it decreases. The speed at which the florescence increases and decreases is due in this case to mainly three factors, the fluid velocity, the diffusion of the beads, and the concentration of the beads [40], providing bead velocity data with high spatial resolution [41-43]. However, there are two main limitations to this method. The first limitation is that the direction of the bead movement cannot be obtained [44]. The second is that the speed is measured in only one small volume element at a time, which means getting a clear spatial map of the bead speed is time consuming. When FCS is paired up with bead video microscopy, both the direction of the bead movement and high spatial resolution of the speed can be obtained

The chapters that follow are designed to be self-contained manuscripts, with introductory sections that give further background and purpose for the dissertation. Thus, some redundancy is present.

In Chapter 2, natural convection induced by electrochemically-generated density gradients at microband electrodes was studied using bead video microscopy during the reduction

and oxidation of the ferricyanide-ferrocyanide redox couple inside the microfluidic reservoir under potential control at gold band electrodes. It was found that the convection was observed at shorter times with higher applied currents, and with higher concentrations and larger electrode areas when a mass transfer limiting potential was applied.

In Chapter 3 FCS and video-microscopy (with particle tracking velocimetry (PTV) and PIV processing approaches) are used together to follow both MHD-based and density gradient-based convection in three dimensions, in contrast to the two dimensions from bead video microscopy alone. FCS provides high spatial resolution down to 2 μm, with low time resolution, while bead video-microscopy provides directional information and better time resolution with lower spatial resolution. This chapter was published in *Analytical Chemistry* [45], and its supporting information in Chapter 3S.

In Chapter 4, experiments with copper and lead in a small volume system consisting of microband electrodes on an insulated silicon chip were performed to explore magnetoconvective and gravitational forces. Two electrode configurations were investigated: (1) single band, where copper or lead was deposited on one microband electrode with counter and reference electrodes distant, and (2) two parallel bands, separated by a known gap, where copper or lead was simultaneously deposited at one microband electrode and stripped off another microband, parallel and near the former. Comparing experiments using paramagnetic Cu(II) to experiments using diamagnetic Pb(II) can give insight into the extent to which magnetoconvective forces influence fluid flow.

In Chapter 5, magnetoconvective and gravitational forces were studied with different magnet arrangements, which allow the magnitude and gradient of the magnetic flux density to

11

vary, altering the magnitude and direction of the magnetoconvective forces. Conditions and

geometries were similar as for the system in Chapter 4, except that only copper deposition and

stripping with two parallel bands was used.

Chapter 6 provides an overall summary of the impact of these studies on the

understanding of density gradients and magnetoconvective forces and their influence on fluid

movement in microfluidic systems. Future directions are also discussed.

1.2 References

[1] N.T. Nguyen, X.Y. Huang, T.K. Chuan, MEMS-micropumps: A review, J. Fluids Eng.-Trans. ASME, 124 (2002) 384-392.

[2] D. Figeys, D. Pinto, Lab-on-a-chip: A revolution in biological and medical sciences, Analytical Chemistry, 72 (2000) 330A-335A.

[3] N.A. Polson, M.A. Hayes, Microfluidics - Controlling fluids in small places, Analytical Chemistry, 73 (2001) 312A-319A.

[4] D.J. Harrison, A. Manz, Z.H. Fan, H. Ludi, H.M. Widmer, Capillary Electrophoresis and Sample Injection Systems Integrated on a Planar Glass Chip, Analytical Chemistry, 64 (1992) 1926-1932.

[5] K. Ching-Te, L. Cheng-Hsien, A Bubble-Free AC Electrokinetic Micropump Using the Asymmetric Capacitance-Modulated Microelectrode Array for Microfluidic Flow Control, Microelectromechanical Systems, Journal of, 18 (2009) 38-51.

[6] S.L. Zeng, C.H. Chen, J.C. Mikkelsen, J.G. Santiago, Fabrication and characterization of electroosmotic micropumps, Sensors and Actuators B-Chemical, 79 (2001) 107-114.

[7] M.C. Weston, M.D. Gerner, I. Fritsch, Magnetic Fields for Fluid Motion, Analytical Chemistry, 82 (2010) 3411-3418.

[8] S.Z. Qian, H.H. Bau, Magneto-hydrodynamics based microfluidics, Mech. Res. Commun., 36 (2009) 10-21.

[9] A.V. Lemoff, A.P. Lee, An AC Magnetohydrodynamic Micropump, Sensors and Actuators B-Chemical, 63 (2000) 178-185.

[10] J.C.T. Eijkel, C. Dalton, C.J. Hayden, J.P. Burt, A. Manz, A circular ac magnetohydrodynamic micropump for chromatographic applications, Sensors and Actuators B-Chemical, 92 (2003) 215-221.

[11] J. West, B. Karamata, B. Lillis, J.P. Gleeson, J. Alderman, J.K. Collins, W. Lane, A. Mathewson, H. Berney, Application of magnetohydrodynamic actuation to continuous flow chemistry, Lab on a Chip, 2 (2002) 224-230.

[12] K.M. Grant, J.W. Hemmert, H.S. White, Magnetic field driven convective transport at inlaid disk microelectrodes - The dependence of flow patterns on electrode radius, Journal of Electroanalytical Chemistry, 500 (2001) 95-99.

[13] N. Leventis, X.R. Gao, Nd-Fe-B Permanent Magnet Electrodes, Theoretical Evaluation and Experimental Demonstration of the Paramagnetic Body Forces, J. Am. Chem. Soc., 124 (2002) 1079-1088.

[14] V. Sahore, I. Fritsch, Flat Flow Profiles Achieved with Microfluidics Generated by Redox-Magnetohydrodynamics, Analytical Chemistry, 85 (2013) 11809-11816.

[15] V. Sahore, I. Fritsch, Microfluidic rotational flow generated by redox-magnetohydrodynamics (MHD) under laminar conditions using concentric disk and ring microelectrodes, Microfluidics and Nanofluidics, 18 (2015) 159-166.

[16] E.A. Clark, I. Fritsch, S. Nasrazadani, C.S. Henry, Analytical Techniques for Materials Characterization, in: R.K. Ulrich, W.D. Brown (Eds.) Advanced Electronic Packaging 2nd edition, IEEE Press, Piscataway, NJ, 2006, pp. 725-791.

[17] E.C. Anderson, I. Fritsch, Factors Influencing Redox Magnetohydrodynamic-Induced Convection for Enhancement of Stripping Analysis, Analytical Chemistry, 78 (2006) 3745-3751.

[18] M.C. Weston, E.C. Anderson, P.U. Arumugam, P.Y. Narasimhan, I. Fritsch, Redox Magnetohydrodynamic Enhancement of Stripping Voltammetry: Toward Portable Analysis Using Disposable Electrodes, Permanent Magnets, and Small Volumes, Analyst, 131 (2006) 1322-1331.

[19] Z.P. Aguilar, P. Arumugam, I. Fritsch, Study of Magnetohydrodynamic Driven Flow Through LTCC Channel with Self-Contained Electrodes, Journal of Electroanalytical Chemistry, 591 (2006) 201-209.

[20] P.U. Arumugam, E.S. Fakunle, E.C. Anderson, S.R. Evans, K.G. King, Z.P. Aguilar, C.S. Carter, I. Fritsch, Characterization and Pumping - Redox Magnetohydrodynamics in a Microfluidic Channel, Journal of the Electrochemical Society, 153 (2006) E185-E194.

[21] M.C. Weston, C.K. Nash, I. Fritsch, Redox-Magnetohydrodynamic Microfluidics Without Channels and Compatible with Electrochemical Detection Under Immunoassay Conditions, Analytical Chemistry, 82 (2010) 7068-7072.

[22] V. Sahore, I. Fritsch, Redox-Magnetohydrodynamics, Flat Flow Profile-Guided Enzyme Assay Detection: Toward Multiple, Parallel Analyses, Analytical Chemistry, 86 (2014) 9405-9411.

[23] E.C. Anderson, M.C. Weston, I. Fritsch, Investigations of Redox Magnetohydrodynamic Fluid Flow at Microelectrode Arrays Using Microbeads, Analytical Chemistry, 82 (2010) 2643-2651.

[24] M. Weston, C. Nash, J. Homesley, I. Fritsch, Maximizing Flow Velocities in Redox-Magnetohydrodynamic Microfluidics Using the Transient Faradaic Current, Analytical Chemistry, 84 (2012) 9402-9409.

[25] M.C. Weston, I. Fritsch, Manipulating Fluid Flow on a Chip Through Controlled-Current Redox Magnetohydrodynamics, Sensors and Actuators B-Chemical, 173 (2012) 935-944.

[26] N. Krishnan, N. Agrawal, M.A. Burns, V.M. Ugaz, Reactions and Fluidics in Miniaturized Natural Convection Systems, Analytical Chemistry, 76 (2004) 6254-6265.

[27] X.P. Gao, J. Lee, H.S. White, Natural-Convection at Microelectrodes, Analytical Chemistry, 67 (1995) 1541-1545.

[28] C. Amatore, C. Pebay, L. Thouin, A.F. Wang, Cyclic Voltammetry at Microelectrodes. Influence of Natural Convection on Diffusion Layers as Characterized by in Situ Mapping of Concentration Profiles, Electrochemistry Communications, 11 (2009) 1269-1272.

[29] C. Amatore, C. Pebay, L. Thouin, A.F. Wang, J.S. Warkocz, Difference between Ultramicroelectrodes and Microelectrodes: Influence of Natural Convection, Analytical Chemistry, 82 (2010) 6933-6939.

[30] V. Sahore, A. Kreidermacher, I. Fritsch, Electrochemically Generated Density Gradient-Induced Natural Convection in Microfluidic Systems, Journal of Electrochemical Society, (2015) in preperation.

[31] N. Leventis, X.R. Gao, Nd-Fe-B permanent magnet electrodes. Theoretical evaluation and experimental demonstration of the paramagnetic body forces, J. Am. Chem. Soc., 124 (2002) 1079-1088.

[32] N. Leventis, A. Dass, Demonstration of the Elusive Concentration-Gradient Paramagnetic Force, J. Am. Chem. Soc., 127 (2005) 4988-4989.

[33] J.M.D. Coey, F.M.F. Rhen, P. Dunne, S. McMurry, The Magnetic Concentration Gradient Force - Is it Real?, Journal of Solid State Electrochemistry, 11 (2007) 711-717.

[34] T. Weier, K. Eckert, S. Muhlenhoff, C. Cierpka, A. Bund, M. Uhlemann, Confinement of Paramagnetic Ions Under magnetic Field Influence: Lorentz Versus Concentration Gradient Force Based Explanations, Electrochemistry Communications, 9 (2007) 2479-2483.

[35] Prasad, Ajay, Particle image velocimetry, 2000.

[36] S.J. Lee, S. Kim, Advanced Particle-Based Velocimetry Techniques for Microscale Flows, Microfluidics and Nanofluidics, 6 (2009) 577-588.

[37] R. Lindken, M. Rossi, S. Grosse, J. Westerweel, Micro-Particle Image Velocimetry (mu PIV): Recent Developments, Applications, and Guidelines, Lab on a Chip, 9 (2009) 2551-2567.

[38] C. Meinhart, S. Wereley, J. Santiago, PIV Measurements of a Microchannel Flow, Experiments in Fluids, 27 (1999) 414-419.

[39] C. Cierpka, C.J. Kaehler, Particle imaging techniques for volumetric three-component (3D3C) velocity measurements in microfluidics, Journal of Visualization, 15 (2012) 1-31.

[40] S.A. Kim, P. Schwille, Intracellular Applications of Fluorescence Correlation Spectroscopy: prospects for neuroscience, Curr. Opin. Neurobiol., 13 (2003) 583-590.

[41] D. Magde, E. Elson, W. Webb, Fluorescence Correlation Spectroscopy .2. Experimental Realization, Biopolymers, 13 (1974) 29-61.

[42] E. Elson, D. Magde, Fluorescence Correlation Spectroscopy .1. Conceptual Basis and Theory, Biopolymers, 13 (1974) 1-27.

[43] D. Magde, W. Webb, E. Elson, Fluorescence Correlation Spectroscopy .3. Uniform Translation and Laminar-Flow, Biopolymers, 17 (1978) 361-376.

[44] T.J. Arbour, J. Enderlein, Application of Dual-Focus Fluorescence Correlation Spectroscopy to Microfluidic Flow-Velocity Measurement, Lab on a Chip, 10 (2010) 1286-1292.

[45] F. Gao, A. Kreidermacher, I. Fritsch, C.D. Heyes, 3D Imaging of Flow Patterns in an Internally-Pumped Microfluidic Device: Redox Magnetohydrodynamics and Electrochemically-Generated Density Gradients, Analytical Chemistry, 85 (2013) 4414-4422.

2. Electrochemically Generated, Density Gradient Induced Fluid Flow in Small Volumes with Microband Electrodes

2.1. Abstract

Natural convection induced by electrochemically-generated density gradients is of interest because it can disorder concentration profiles, leading to deviations from the classic equations derived for static solutions, and disrupt fluid flow profiles in microfluidic settings, impacting micro total analysis applications with opportunities to generate localized stirring. Here, such convection was induced at various sized microband electrodes on an insulated silicon chip under different conditions and is compared to results previously reported for a disk-ring geometry. The horizontal fluid motion as monitored by video microscopy of microbeads added to the solution is easier to quantify than at the disk-ring geometry because of simpler flow to or from the straight (instead of curved) edge of the electrode. A greater magnitude of convection is also achieved for bands than for the disks in the previous studies where the band widths (15, 40, 90, and 625 μm) have a similar scale as the diameters of disks, because of the larger band areas (due to their length of 2000 μm). A cathodic or anodic potential or current was applied to microband electrodes in a ferrocyanide/ferricyanide solution to produce a change in fluid density near the electrode, resulting in natural convection. Conditions included different concentrations of redox species (95.2 mM, 47.6 mM, and 9.52 mM) under potential control and different constant currents (80 μA, 60 μA, 40 μA, and 20 μA) for a fixed concentration in an electrochemical cell with dimensions of 5.5 mm × 12.6 mm × 0.810 mm. The stronger convection at the band electrodes (with horizontal speeds as high as 25 μm/s for a 90 μm wide band) as compared to the disk (with horizontal speeds of 6 μm/s for a 76 μm diameter disk) leads to a greater deviation from theoretical currents for static solutions with a more impactful effect for microfluidic applications in less time and with lower concentrations of redox species.

2.2. Introduction

Substantial natural convection can be produced by electrochemically-generating density gradients at band microelectrodes in a small volume of static solution. Previous work used disk microelectrodes in large [1-4] and small volumes [5]. In addition, the effects of natural convection have been simulated to generate concentration profiles that resemble experimental results [3]. However, the impact of different shapes on natural convection has not been addressed.   Band microelectrodes were chosen here to investigate this phenomenon further, because they primarily produce parallel ion movement toward the electrode edge caused by a 2-dimensional diffusion pattern rather than the radially inward convection caused by a 3-dimensional diffusion pattern of a disk electrode. This makes the resulting parallel fluid flow of a band electrode easier to quantify than at a disk. Convection caused by density gradients specifically in a microfluidic setting are of interest as a means of localized stirring without the use of high voltages or moving parts. Also, density gradient based convection can cause the electrochemical signal to deviate from theory based on diffusion because it affects the flux of redox species to the electrode surface. A summary of the impact of the natural convection on applications and fundamentals is described in our earlier paper[6]. Studies have been performed previously on band electrodes in nearly identical electrochemical conditions to induce magnetohydrodynamic-based convention; however, those studies did not address natural convection because the majority of the density gradient effects were obscured by the convection due to the presence of the magnetic field [4, 7].

Natural convection is caused by density gradients that are created in the diffusion layer when the oxidation or reduction changes the charge on an electroactive species. If counterions move in to compensate charge (because of a change in the charge of the electroactive species),

then the density of that fluid element increases (and neighboring fluid elements decrease in density). If counterions move away (because an electroactive species of lower charge is produced), then the density of that fluid element decreases (and vice versa for the neighboring fluid elements). Fluid movement created by density gradients is called natural convection. For the redox couple used in these studies, when ferrocyanide ($[Fe(CN)_6]^{4-}$) is oxidized at the anode and ferricyanide ($[Fe(CN)_6]^{3-}$) is reduced at the cathode, a net movement of potassium counter ions move toward the cathode and away from the anode, producing a lower volume element near the anode and higher density volume element near the cathode. Whether the fluid element becomes less or more dense upon oxidation or reduction of the electroactive species depends on the concentration, charge, and mobility of all of the ionic species.

Often, the visual onset of natural convection is delayed from when the current is first applied, a phenomenon called Rayleigh-Benard convection [8], This can be seen with both ring and band electrodes. This is due to the fact that the gradients must build up so that the buoyant forces are great enough to overcome the viscous dampening.

Here the effects of electrochemically generated density gradient based fluid movement around gold microband electrodes in a small volume, microfluidic environment are studied, using the $Fe(CN)_6^{3-}$ - $Fe(CN)_6^{4-}$ redox couple. The fluid movement is tracked using bead video microscopy in addition to the electrochemical response.

2.3. Experimental

2.3.1. Chemicals and Materials

All chemicals were reagent grade and used as received. Aqueous solutions were prepared with high purity deionized water from Ricca Chemical Co. (Arlington, TX), resistivity 18 MΩ-cm. Potassium ferricyanide ($K_3Fe(CN)_6$) was obtained from EM Science (Gibbstown, NJ) and potassium ferrocyanide trihydrate ($K_4Fe(CN)_6 \cdot 3H_2O$) was purchased from J.T. Baker (Phillipsburg, NJ). The potassium chloride was acquired from VWR (Radnor, PA). The 10-μm polystyrene latex microspheres (sulfonated, 2.5 wt% dispersion in water) were obtained from Alfa Aesar (Ward Hill, MA). Electrical connection of the potentiostat to on-chip contact pads was made using an edge connector (solder contact, 20/40 position, 0.05 in. pitch) from Sullins Electronics Corp. (San Marcos, CA). Glass microscope slides were acquired from VWR (Radnor, PA).

2.3.2. Microelectrode Array Design and Fabrication

The microelectrode array chips were fabricated using the procedure found in Anderson et al [4] with the exception that a Radio Corporation of America (RCA) clean process was used to clean the silicon wafer prior to fabrication and the thickness for chromium and gold was 10 and 100 nm respectively. The RCA procedure involves an organic clean (using 5:1:1 mixture of DI $H_2O:NH_4OH:H_2O_2$ maintained at 75 °C) followed by an oxide stripping process (50:1 mixture of DI H_2O: HF at 27 °C) to remove the native grown silicon oxide (~50 nm). There are two different designs of 2.54 cm × 2.54 cm chips used in the experiments. One (Figure 1c) has 16 individually addressable microband electrodes measuring 2000 μm in length having widths of either 15 μm, 40 μm, or 90 μm, with 35 μm, 60 μm, and 110 μm gaps separating them,
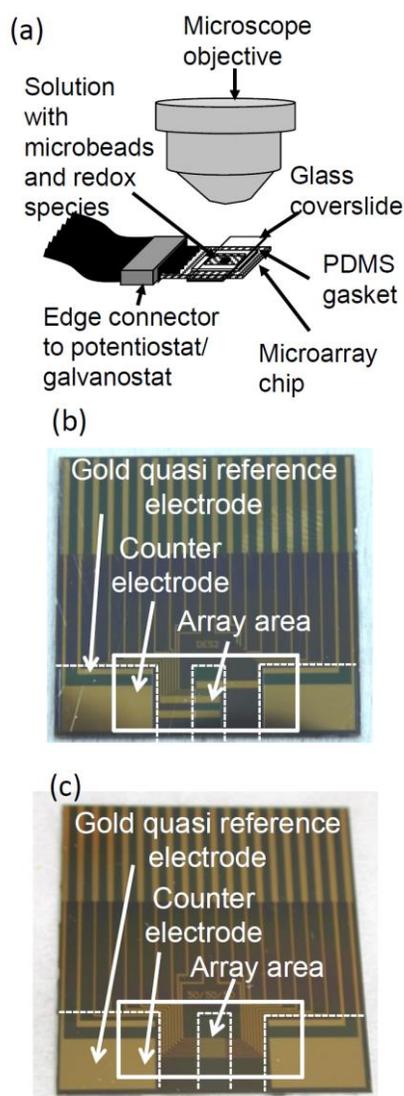
Figure 1. (a) Side view diagram of the experimental setup for the density gradient experiments. (b) One design of microfluidic chip used in the density gradient experiments. The array area which is patterned with 16 gold microband electrodes in the array having lengths of 2000 μm and one of the following widths: 15, 40, or 90 μm. There are two identical gold counter and two identical gold quasi-reference electrodes, one counter and quasi-reference electrode on either side of the array area. Dashed outlines emphasize the edge of the BCB insulating layer. Solid line shows the location of the PDMS wall. (c) A second design of microfluidic chip used in the density gradient experiments. The array area is patterned with 8 gold, individually-addressable, microband electrodes having lengths of 2000 μm. three have widths of 625 μm and the other five have a width of 40 μm. There are two identical gold counter (5000 × 8000 μm) and two identical gold quasi-reference electrodes (800 × 6000 μm), one counter and one quasi-reference electrode on each side of the array area. Dashed outlines emphasize the edge of the BCB insulating layer. Solid line sows the location of the PDMS wall.

respectively. The second design (Figure 1b) has three, 625 μm wide electrodes separated by 675 μm. Between two of the 625 μm electrodes were six, 40 μm bands with 60 μm spacing. Only the 625 μm electrodes were used in the second design and they were 2000 μm long. All of the experiments, with the exception of the electrode size study, were performed with the 625-μm wide electrodes, because they produce the most dramatic electrochemically-induced density gradient flow. The quasi-reference electrode was one of the medium-sized (800 × 6000 μm) bare gold electrodes labeled in Figure 1b and c. The counter electrode was one of the large (5000 × 8000 μm) gold electrodes labeled in Figure 1b and c.

2.3.3. Experimental setup

An 810 μm PDMS gasket with an opening of 5.5 mm ×12.6 mm was set on top of the chip, and solution delivered into the opening. Due to a thin layer of solution between the PDMS gasket and the microscope slide the thickness of the cell varies between experiments, and is within a range of 1000 to 1200 μm. Stock solutions were made with $K_3Fe(CN)_6$ and $K_4Fe(CN)_6$ concentrations, each of 100 mM, 50 mM, and 10 mM each, with 100 mM potassium chloride. The 10 micron polystyrene latex beads in a 2.5% by weight solution were added with a 20 to 1 stock solution to bead solution ratio. Resulting in solutions with $K_3Fe(CN)_6$ and $K_4Fe(CN)_6$ concentrations of 95.2 mM, 47.6 mM, and 9.52 mM each with 95.2 mM potassium chloride. All solutions contained 95.2 mM KCl, and an equimolar amount of $K_3Fe(CN)_6$ and $K_4Fe(CN)_6$. Unless stated otherwise, the concentration of $K_3Fe(CN)_6$ and $K_4Fe(CN)_6$ was 95.2 mM each. A glass microscope slide was placed on the solution surrounded by the gasket to make an electrochemical cell. The cell was placed under a microscope as shown in Figure 1a.

2.3.4. Electrochemical Control

All electrochemical experiments involved a three electrode configuration. The counter (5000 × 8000 μm) and quasi-reference (800 × 6000 μm) electrodes were both much larger than the working electrodes and located at a substantial distance away so as not to perturb the density gradients at the working electrode (the counter electrode and reference electrodes were 3200 μm and 4500 μm away, respectively) from and on one side of the array as shown in Figure 1b. The

working electrode was always located in the array area. For the electrode size study, the electrodes were 2000 μm long with widths of 15, 40, 90, and 625 μm. For all other studies the working electrode was 2000 μm long by 625 μm wide. A CHI 650A potentiostat (CH Instruments, Austin, TX) was used for chronoamperometry, (CA). An oxidizing potential of 0.3 V was applied for 60 s for all CA experiments except in one set of experiments when a reducing potential of -0.3 V was applied for 60 s before going to open circut. A CHI 760A potentiostat was used for the chronopotentiometry experiments where anodic currents of -50, -40, -30, and -20 μA were applied for 60 s, and are below the mass transfer limit. Both CA and CP experiments had a 2 s quiet time at 0 V.

2.3.5. Bead Video Microscopy Analysis

The bead movement was observed with a Nikon Eclipse ME600P microscope, and movies were recorded using a Sony Handycam digital camera (model no. HDR-XR500V, 30 frames per second with 720 × 480 pixels per frame). Every tenth frame recorded in a 5 s video segment was extracted as a still image and loaded on to DynamicStudio v.3.00 software (Dantec Dynamics, Copenhagen, Denmark) for particle image velocimetry (PIV) analysis as described in Scrape et al. [9]. Velocities were measured using the numeric data used to make the PIV image,

and multiple points on the image were measured to get an average. The standard deviation was used to determine the length of the error bars. The velocity measurement was conducted along a line 150 μm right of the area where the horizontal movement converges or diverges. Studies with beads immobilized on a glass slide were used to measure the depth of focus for the microscope used in all the experiments, which gave a value of 150 μm. A vertical profile of horizontal velocity could be obtained by varying the focus of the microscope throughout the height of the electrochemical cell.

2.4. Results and Discussion

2.4.1. Overview of Measurements and Flow Paths Caused by Electrochemically-Generated Density Gradients

Before engaging in discussion about fluid motion due to electrochemically-induced density gradients, it is necessary to consider the contribution of other factors that could lead to bead movement and changes in current or potential during oxidation and reduction. For example, the microbeads used here have a negative charge due to sulfonate moieties on the surface. One would expect such beads to move toward the anode due to electrophoresis. This phenomenon must not play a significant role because microbeads of other compositions (e.g. amines at pH 6, which should be positively charged) exhibit similar behavior as the negatively charged ones in our high ionic strength solution. Convection due to electroosmosis also has been ruled out, despite the fact that a SiO_2 surface (a common material in microfluidic channels pumped by electroosmosis) lies between the working and counter electrodes. Electroosmosis requires large applied potentials and a large surface-to-volume ratio–two features that our experiment does not have. Other experiments that are reported elsewhere for similar microchip

24

geometries but without redox species in solution [10] do not exhibit the same fluid flow because a diffusion layer cannot be established at the electrode surface. Likewise, temperature gradients that induce density gradients caused by resistive heating of the electrode are not of significance here because the fluid moves in the opposite direction when the direction of the current of the same magnitude is reversed.

The cause of the electrochemically generated density gradients is the movement of ions. At the anode, the density gradients that lead to natural convention are caused by the migration of potassium, $Fe(CN)_6^{3-}$, $Fe(CN)_6^{4-}$ and chloride ions to compensate for the oxidation of $Fe(CN)_6^{4-}$. As discussed previously the majority of the composition comes from the potassium ion [6]. Table 1 lists the transference numbers. Which were calculated using the equation 1, where t_i is the transference of ion j. μ_i and μ_j are the mobilities of ions i and j. The result is a less dense solution near the electrode. At the cathode, the direction of the migration is reversed and a more dense solution is the result.

$$t_j = \frac{|z_i|\mu_i C_i}{\sum_j |z_j|\mu_j C_j} \tag{1}$$

Table 1. Transference numbers for solutions with $K_3Fe(CN)_6$ and $K_4Fe(CN)_6$ concentrations of 95.2 mM, 47.6 mM, and 9.52 mM each. With a KCl concentation of 95.2 mM in all three solutions. Ion mobilities are from Bard and Falkner [11].

Ion	Transference at 95.2 mM	Transference at 47.6 mM	Transference at 9.52 mM	Mobility of ion / m^2 s^{-1} V^{-1}
$Fe(CN)_6^{3-}$	0.115	0.098	0.045	3.49×10^{-08}
$Fe(CN)_6^{4-}$	0.126	0.108	0.050	2.86×10^{-08}
Cl^-	0.087	0.149	0.343	7.91×10^{-08}
K^+	0.671	0.645	0.563	7.62×10^{-08}

We observe the effect of density gradients on the current response at band electrodes in our small volume microelectrochemical system shown in Figure 1a. When a potential is applied at a bare gold electrode that is different than that of the surrounding static solution without redox species, a charging current is produced and is expected to fall off exponentially with time [11]. When in the presence of an electroactive species that undergoes fast electron transfer kinetics at the applied potential, the superimposed faradaic current also falls off with time, but in a diffusion-limited fashion (following the Cottrell equation for a macroelectrode in a semi-infinite solution, that dependence is with the square root of time). However, the experimentally observed current such as under our conditions does not follow this diffusion-limited model. Figures 2 and 3 provide a general overview of the electrochemical and fluid velocity responses that take place at a gold band electrode in an electrolyte solution containing $Fe(CN)_6^{3-}$ / $Fe(CN)_6^{4-}$ upon oxidation and reduction, respectively.

When the electrode serves as an anode and electrochemically converts $Fe(CN)_6^{4-}$ to $Fe(CN)_6^{3-}$ which is accompanied simultaneously with a net charge compensation by potassium ions leaving the region, the fluid elements at the electrode becomes less dense than the surrounding solution. The current (Figure 2a) reaches a minimum at time t_{min}, then increases until a second maximum (where the first maximum occurs at the beginning of the potential step) is reached at time t_{max}, followed by subsequent dampened oscillations until a steady state is achieved. The current response is consistent with the response from concentric disk and ring electrodes in a similar solution composition and small volume cell [6]. The cell height of 1000 to 1200 μm exceeds the length of the diffusion layer for the longest experiments reported here, 60 s (245 μm, using the Einstein equation and assuming a diffusion coefficient of 5×10^{-6} cm^2/s). However, the fluid flow is restricted due to the close proximity of top of the cell. This facilitates

the oscillatory behavior that is typical of such confined spaces. Such oscillations are not seen when a large volume is used [3]. Volgin et al. [12] reviewed natural convective instabilities in enclosed electrochemical systems with electrodes on opposing walls (floor and ceiling of the cell), where only the current was monitored for evidence of convection. They describe a critical time, t_c, when convection begins, just before there is a measurable deviation from the Cottrell curve, which occurs at t_v. The current deviates from the Cottrell curve when the convection becomes strong enough to alter the diffusion layer at the electrode surface. However, because it is impossible to determine that time from the current alone, the emergence of convection is often judged on the basis of t_v or when the current reaches the minimum, t_{min}. The minimum is reached once the current increase due to convection is stronger than the decrease in current due to the lengthening of the diffusion layer. The current reaches a maximum at t_{max}, which occurs at the steepest concentration gradient as happens when the diffusion length thins when the fluidics bring bulk solution to the surface. After t_{max} bulk solution moving in reduces the density gradient force and the convection slows and as a result the current drops. Subsequent minima and maxima occur with reduced magnitude until a steady state is reached.

The significant contribution that we make here is the simultaneous monitoring of the fluid flow and comparison of that with the electrochemical response. Figure 2b and c show velocity vectors obtained from PIV analysis of microbead movement at two different heights in the cell. Because only horizontal flow can be visualized with the approach we use here, fluid motion at different heights in the cell need to be monitored to determine the overall fluid
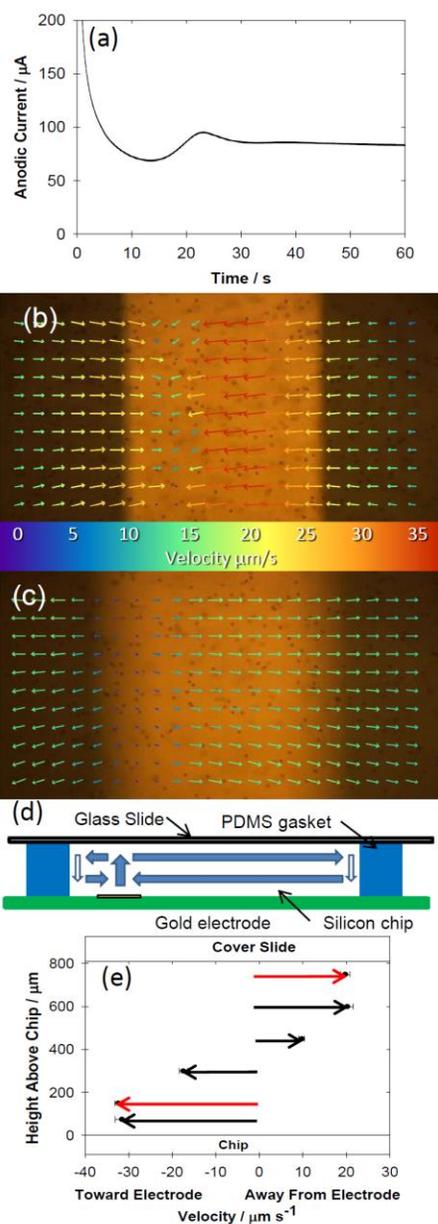
Figure 2. Fluid movement due to electrochemically-generated density gradients at a 625 μm electrode with an oxidizing potential. (a) Representative CA response. (b) PIV image of resulting bead movement at 150 μm above the chip surface. (c) PIV image of resulting bead movement at 750 μm above the chip surface. (d) Schematic of overall flow circulation generated by the electrochemically-induced density gradients, indicated by blue arrows. The outlined arrows were not observed. Downward movement is necessary to balance the fluid flow for which the exact location is not known. (e) Vertical flow profile. Bead movement was analyzed at from 55 - 60 s after the potential was applied The solution contained 95.2 mM $K_3Fe(CN)_6$, 95.2 mM $K_4Fe(CN)_6$, and 95.2 mM KCl (with microbeads), and the on-chip counter and on-chip quasireference electrodes were used in a three-electrode configuration.

circulation including the implied vertical movement that drives the horizontal movement. Near the chip surface, the fluid moves horizontally in opposite directions toward the electrode (Figure 2b), replacing solution that has risen to the top. Near the lid of the cell, the microscope slide, the horizontal movement is away from the electrode (Figure 2c), displaced by the solution that has risen to the top. The locus of vertical movement of less dense solution that drives the circulation appears as a thin strip in the PIV images, which is the region where the horizontal movement converges near the bottom and diverges near the top of the cell. The vertical movement is not at the center of electrode because the chip is not completely level. This is especially noticeable closer to the lid (Figure 2c). A simple diagram of the overall fluid circulation is given in Figure 2d.

The vertical circulation was further evaluated by quantifying the horizontal fluid motion at 150 μm from the convergent line at 75, 150, 300, 450, 600 and 750 μm heights above the 625 μm wide band anode (Figure 2e). Each height was examined during separate experiments and at the same time of 55 to 60 s from the start of the potential step. This time corresponds to the last five seconds of the current response in Figure 2a. Fluid moves away from the electrode at 75, 150 and 300 μm above the chip surface with velocities of 31.5 ± 1.5, 32.4 ± 0.8 and 17.4 ± 0.9 μm s^{-1}, respectively. The solution changes direction between 300 and 450 μm above the chip surface, approximately halfway to the lid. The solution moves away from the electrode at 450, 600, and 750 μm above the chip surface with velocities of 9.7 ± 0.7, 20.2 ± 1.4, and 19.8 ± 1.8 μm s^{-1} respectively.

Studies performed with coplanar, concentric disk and ring electrodes under the same conditions [6], show similar trends. The exceptions are that the horizontally moving solution converges radially to a point at the disk electrode, and the velocities are much slower because the

smaller currents (limited by the smaller electrode areas) produce a slower evolution of density gradients at the disk and ring electrodes. Thus, it is easier to quantify the fluid flow for the band electrode case here.

When the electrode serves as a cathode and electrochemically converts $Fe(CN)_6^{3-}$ to $Fe(CN)_6^{4-}$, which is accompanied simultaneously with a net charge compensation by potassium ions migrating into the region, the fluid elements at the electrode become more dense than the surrounding solution. Unlike the anodic case, the cathodic current (Figure 3a) does not undergo oscillations and behaves more as if it is diffusion limited. The behavior is due to the fact that the more dense solution spreads outward, driving the convection, and does not interact with the top of the cell. This behavior is also consistent with our previous work using concentric disk and ring electrodes [6]. Volgin et al. [12] also report this more stable system, but do not account for spreading of the more dense solution because their cathode covers the entire area of the floor. However, we can clearly observe bead movement near the chip surface (75 μm) but in the opposite direction of that for the anodic case, and the velocity is greatly diminished (Figure 3b). At 600 μm above the chip surface and at the same time (Figure 3c), the PIV image shows horizontal fluid movement in the reverse direction, ,as it displaces the solution falling toward the cathode. Figure 3d, illustrates the general circulation of the solution and Figure 3e quantifies the vertical flow profile, where the measurements were taken 150 μm from the convergent/divergent line. Fluid moves away from the electrode at 75 and 150 μm above the chip surface with velocities of 10.6 ± 1.2 μm s^{-1} and
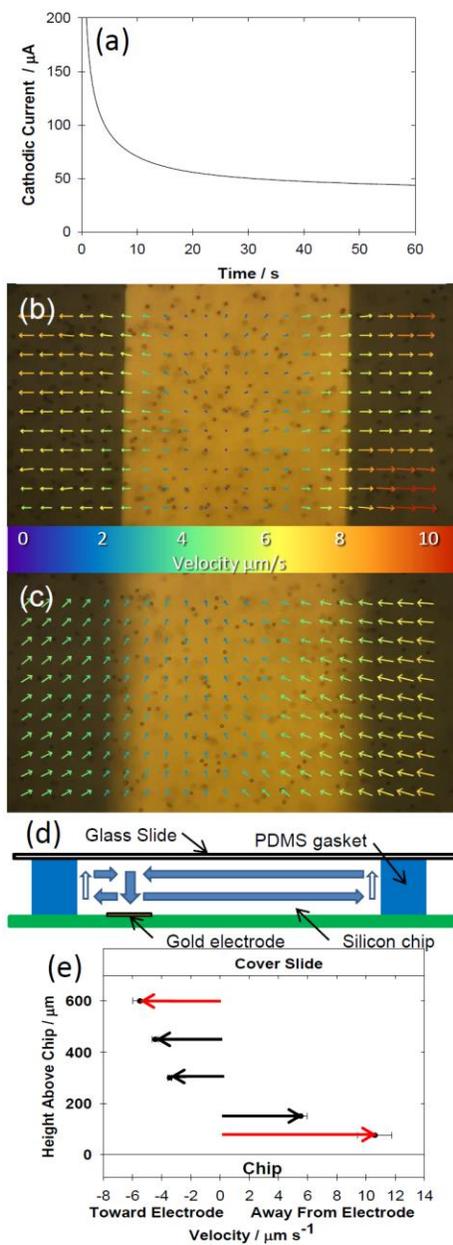
Figure 3. Fluid movement due to electrochemically-generated density gradients at a 625 μm electrode with a reducing potential (a) Representative CA response. (b) PIV image of resulting bead movement at 75 μm above the chip surface (c) PIV image of resulting bead movement at 600 μm above the chip surface (d) Schematic of overall flow circulation generated by the electrochemically-induced density gradients, indicated by blue arrows. The outlined arrows were not observed. Upward movement is necessary to balance the fluid flow for which the exact location is not known. (e) Vertical flow profile. Bead movement was analyzed at from 55 - 60 s after the potential was applied. The solution contained 95.2 mM $K_3Fe(CN)_6$, 95.2 mM $K_4Fe(CN)_6$, and 95.2 mM KCl (with microbeads), and the on-chip counter and on-chip quasireference electrodes were used in a three-electrode configuration.

5.5 ± 0.5 µm s^{-1}, respectively. The solution changes direction between 150 and 300 µm above the chip surface, at a lower level than for the anode case. The solution moves away from the electrode at 300, 450, and 600 µm above the chip surface with velocities of 3.4 ± 0.1, 4.4 ± 0.2, and 5.5 ± 0.5 µm s^{-1} respectively. These "snapshots" of fluid velocity were taken at the same time (55 to 60 s) after applying the potential as in the anodic case. Because the electrochemical reaction generates greater convective instability at the anode than at the cathode for this chemical system, the focus of the rest of this chapter is on convection due to the anodic process.

2.4.2 Density Gradient Calculations in Ferricyanide and Ferrocyanide

At the anode, the density gradients that lead to natural convention are caused by the migration of the positive and negative ions to compensate for the oxidation of $Fe(CN)_6^{4-}$ to $Fe(CN)_6^{3-}$. A simple one-dimensional concentration profile during a diffusion limited experiment, and before the onset of natural convection can be calculated. For these calculations, concentration values of 100 mM $K_3Fe(CN)_6$, 100 mM $K_4Fe(CN)_6$, and 100 mM KCl.

The first step is to calculate the concentration profile of $Fe(CN)_6^{3-}$ and $Fe(CN)_6^{4-}$. The concentration profile can be found for $Fe(CN)_6^{3-}$ using equation 2 below [11], where D_O is the diffusion coefficient of $Fe(CN)_6^{3-}$, d is the distance from the electrode, C_O is the concentration of $Fe(CN)_6^{3-}$ at a certain distance from the electrode, C_O^* is the bulk concentration of $Fe(CN)_6^{3-}$, and C_R^* is the bulk concentration of $Fe(CN)_6^{4}$. The value of **t** for these calculations is 10 s.

$$C_O = C_O^* + C_R^* \operatorname{erfc} \left[\frac{d}{2(D_O t)^{1/2}} \right] \tag{2}$$

Equation 3 was used to solve for the concentration profile for $Fe(CN)_6^{4-}$, where C_R is the

concentration of $Fe(CN)_6^{4-}$ at a certain distance from the electrode, and D_R is the diffusion

coefficient of $Fe(CN)_6^{4-}$.

$$C_R = C_R^* - C_R^* \text{erfc}\left[\frac{d}{2(D_R t)^{1/2}}\right]$$ (3)

The second step is to compensate for the change in charge that occurs during the

oxidation and reduction. To keep the model simple, it was assumed that only the potassium and

chloride ions migrate. The difference in charge between the the redox species in the bulk solution

and those in the diffusion layer at different locations from the electrode, z_d, is calculated by using

equation 4, where z_O is the charge of $Fe(CN)_6^{3-}$, and z_R is the charge of $Fe(CN)_6^{4-}$.

$$z_d = (z_O C_O + z_R C_R) - (z_O C_O^* + z_R C_R^*)$$ (4)

The fraction of the charge that is compensated by the K^+ or Cl^- ions is found by

calculating the transference number for both ions using the equation 1. The transference numbers

obtained in this way are: $t_{Cl} = 0.1149$, $t_K = 0.8851$.

The concentration of K^+ or Cl^- can be calculated using equation 5. Where C_i is the

concentration of K^+ or Cl^-.at a certain distance from the electrode, C_i^* is the bulk concentration of

K^+ or Cl^-, and t_i is the transference number of K^+ or Cl^-.

$$C_i = C_i^* + t_i z_d$$ (5)

Figure 4a has the concentration profiles of $Fe(CN)_6^{3-}$, $Fe(CN)_6^{4-}$, K^+, and Cl^-.. In this model, the $Fe(CN)_6^{3-}$ and $Fe(CN)_6^{4-}$ only move by diffusion. All the $Fe(CN)_6^{4-}$ at the electrode is oxidized to $Fe(CN)_6^{3-}$. The K^+, and Cl^- move by migration to account for the change in charge when $Fe(CN)_6^{4-}$ is oxidized to $Fe(CN)_6^{3-}$. The concentrations approach the bulk concentration as the distance from the electrode increases. The concentration of K^+ starts out well below the bulk concentration and increases to slightly above the bulk concentration before returning to the bulk concentration levels. This is due to the fact that $Fe(CN)_6^{3-}$ has a higher diffusion coefficient than $Fe(CN)_6^{4-}$.

The force caused by density gradients ($\mathbf{F_g}$) is the acceleration due to gravity multiplied by the difference between the density at a certain position (ρ) and the bulk density (ρ^*). The force caused by density gradients can be found using equation 6, where g is the acceleration due to gravity, m_K is the molar mass of K^+, m_{Cl} is the molar mass of Cl^-, and m_R is the mass of $Fe(CN)_6^{3-}$, and $Fe(CN)_6^{4-}$.

$$\mathbf{g}(\rho - \rho^*) = \mathbf{F_g} = \mathbf{g}\{m_K(C_K - C_K^*) + m_{Cl}(C_{Cl} - C_{Cl}^*) + m_R(C_O + C_R - C_O^* - C_R^*)\} \qquad (6)$$

Figure 4b has a graph of $\mathbf{F_g}$ vs. the distance from the electrode. Negative force indicates the force is in the upward direction. As expected, the force near the electrode is upward for oxidation, which is supported by the upward motion observed above the electrode during experiments. The K^+ and Cl^- move in opposite directions to balance the charge caused by the $Fe(CN)_6^{3-}$ and $Fe(CN)_6^{4-}$. K^+ moves out to create the upward force while Cl^- moves in and reduces the force. An unexpected result is the downward force farther away from the electrode. This is due to the fact that $Fe(CN)_6^{3-}$ has a higher diffusion coefficient than $Fe(CN)_6^{4-}$. As a

34

result, the $Fe(CN)_6^{4-}$. approaches bulk concentration at distances where $Fe(CN)_6^{3-}$. is still above

the bulk concertation. The net result is near the end of the diffusion layer the combined

$Fe(CN)_6^{3-}$ and $Fe(CN)_6^{4-}$ concentrations is higher than in bulk solution. The force pushing

downward is weaker than the force pushing upward. Convection caused by the simulated force

would only become visible at longer times when the diffusion layer is thicker, simaler to what is

observe experimentally. However, the model has 2 main limitations, it does not account for

confined volume where the lid is concerned, and it also assumes that the fluid flow does not

affect concentrations. In order to overcome these limitations more work would needs to be done

to fully explain the velocity response to the density gradients.
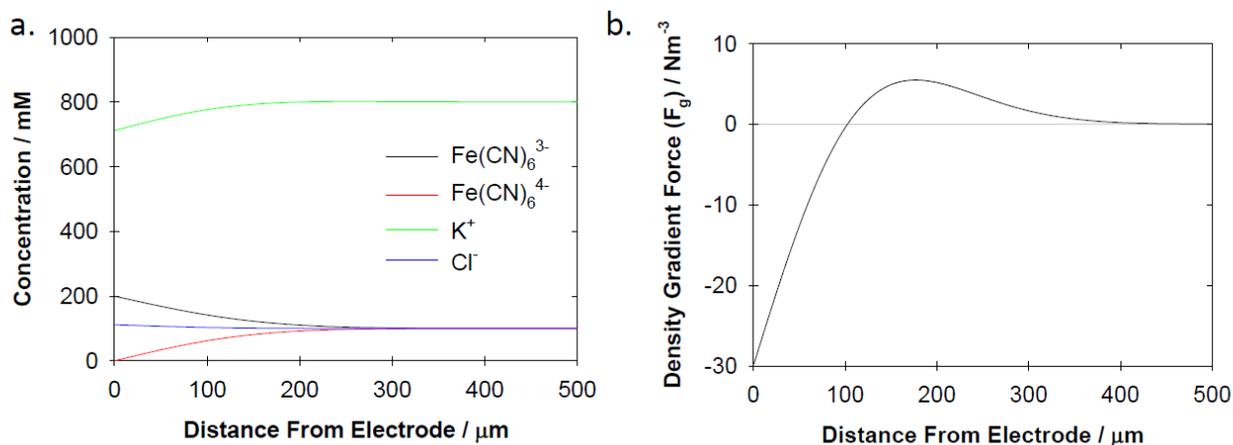
Figure 4. (a) Calculated concentrations of ferricyanide, ferrocyanide, potassium, and chloride ions as a function of distance from electrode 10 s after the beginning of applied potential. (b) Calculated magnitude of F_g as a function of distance from electrode using the concentrations from part a.

3.4.3. Factors that Affect Convection Due to Electrochemically-Generated Density

Gradients
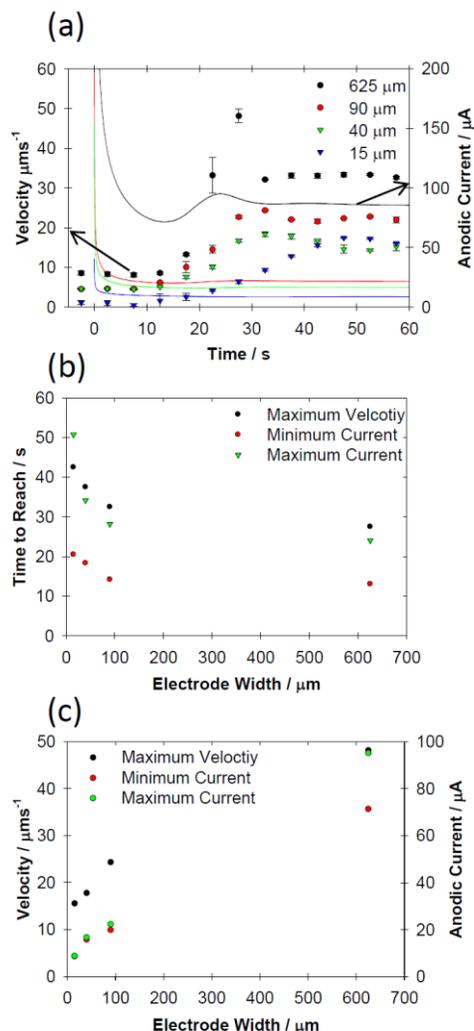
Figure 5. (a) Dependence of current (solid curves) and fluid movement (markers) on time for different widths of microband electrodes (625, 90, 40, and 15 μm) just before and during an anodic potential step. The fluid movement was determined by the speed of beads at a distance of 150 μm from the electrode chip and located 150 μm to the left of where the fluid was rising. For the 625 μm electrode the fluid was rising over the center of the electrode. For the 90, 40, and 15 μm electrode the fluid was rising over the right edge of the electrode. (b) The times it takes to reach the maximum velocity, minimum current, and maximum current are shown for each electrode width, obtained from data in (a). (c) Values of the maximum velocity magnitude, minimum current, and maximum current are shown for each electrode width, obtained from the data in (a).

The magnitude of the density gradients that influence the velocity of the natural convection should be proportional to the current (the turnover rate of redox species in solution). Three factors were investigated to vary the current. One is electrode width (Figure 5) during an applied potential experiment, where current initially depends on the diffusional flux. A second is the starting concentration of redox species (Figure 6) during an applied potential experiment, where current initially depends on the bulk concentration. And a third (Figure 7) is the application of a constant current (as long as it remains below the mass transfer limit to ensure 100% current efficiency) to directly control the evolution of concentration with time.

Consideration of the band width of the electrodes for a fixed concentration and cell geometry provides insight into how concentration gradients (and therefore density gradients) form and dissipate with the different effects of radial and linear diffusional flux, as well as natural convection. The electrode widths investigated were 625 μm, 90 μm, 40 μm, and 15 μm (all electrodes are 2000 μm long). The electrode areas are 1.25 mm^2, 0.038 mm^2, 0.080 mm^2, and 0.050 mm^2. Figure 5a shows an overlay of the evolution of current and fluid speed as a function of time for a potential step experiment at each of these band widths for 95.2 mM concentrations of $K_3Fe(CN)_6$ and $K_4Fe(CN)_6$. The behaviors of both the current and velocity are similar for all of the widths, but with less dramatic features that extend over a longer time frame as the band width narrows. The current reflects the same trends with a minimum, t_{min}, preceding a (second) maximum, t_{max}, as was described in the previous section. The fluid speed begins to increase over the background just about 10 s after the potential was applied, which occurs even before t_{min} in the current. The velocities reach a maximum at increasing times as band width increases, from 28 s for the 625 μm width to 37 s for the 40 μm width, and appear about 5 s after t_{max} for the

current, except at the 15 µm band because it has not yet reached a velocity maximum within the 60 s experiment time. A reason why the velocity reaches a maximum shortly after the current reaches a maximum is that although changes in convection start near the electrode they move out into solution where they are observed with a time delay. The times it takes to reach the minimum and maximum currents, as well as the maximum velocities as function of band width are summarized in Figure 5b. The values of these maxima and minima are plotted in Figure 5c. The larger the electrode width, the greater the relative differences between the current value at t_{min} and t_{max}. Also, the larger electrodes produce earlier maxima in fluid velocity due to the increased current resulting in larger density gradients at earlier times. Then it drops to an approximate steady state that in general has a higher magnitude for the larger widths. At long times, the velocities appear to reach a steady state that for three of the electrodes depends on the width. Only the 15 µm band does not fit this trend because the velocity has yet to reach steady state. The diffusion length of about 245 µm at 60 s greatly exceeds the smallest dimension for the three smallest band electrodes, so that radial diffusion would dominate mass transfer, and therefore aid in diluting the concentration gradients as well. This is not the case with the 625 µm electrode, to which linear diffusion would dominate flux. Thus, it is surprising that fluid velocity is easily observed at the smaller electrodes. The height of the cell relative to the width of the electrode might contribute to suppressing convection more at the large electrode than at the narrow ones, however.
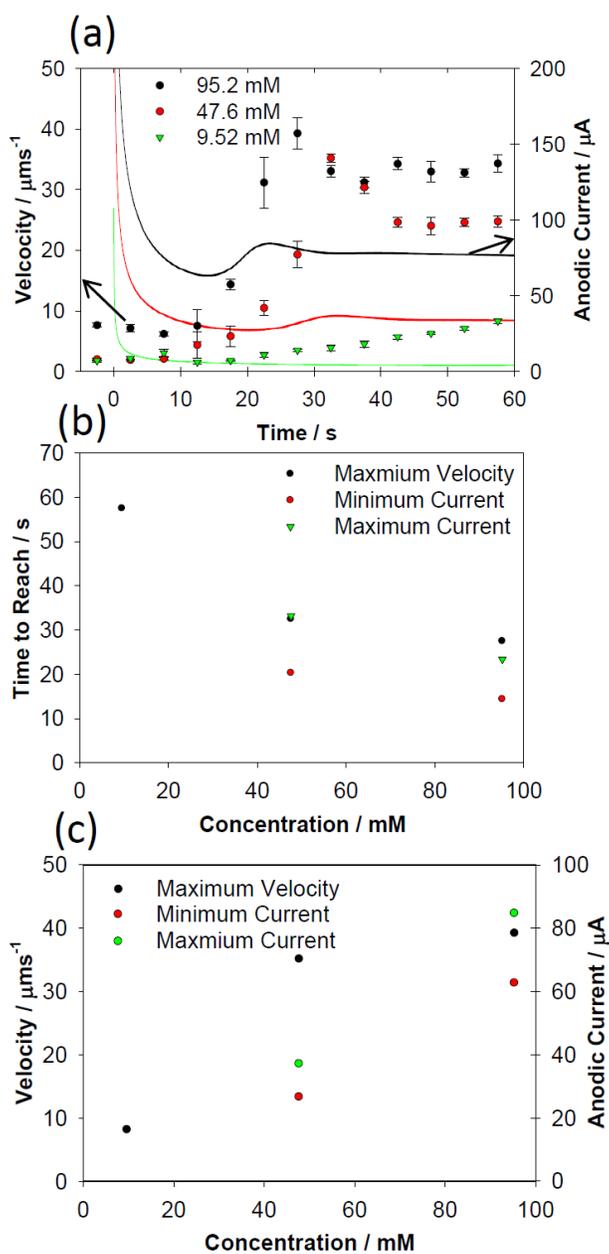
Figure 6. (a) Dependence of current (solid curves) and fluid movement (markers) on time at a 625 μm band electrode for different concentrations of $K_3Fe(CN)_6$ and $K_4Fe(CN)_6$ (each at 95.2 mM, 47.6 mM, and 9.53 mM) in a solution containing 95.2 mM KCl (and microbeads) during an anodic potential step. The fluid movement was determined by the speed of beads at a distance of 150 μm from the electrode chip and located 150 μm to the left of where the fluid was rising. (b) The times it takes to reach the maximum velocity, minimum current, and maximum current are shown for each concentration, obtained from data in (a). (b) Values of the maximum velocity, minimum current, and maximum current are shown for each concentration, obtained from data in (a).

To eliminate the variations in diffusional mass transfer to the different band widths and the impact of the different ratios of width to cell height on convection, a series of experiments at three different concentrations at an electrode at a fixed width of 625 μm was performed. Figure 6a overlays the time dependence of bead velocity with that of current for solutions containing 95.2 M KCl and equimolar concentrations of $K_3Fe(CN)_6$ and $K_4Fe(CN)_6$ of 95.2 mM, 47.6 mM, and 9.52 mM. The time to reach t_{min} and t_{max} in the current and the maximum velocity are shown in Figure 6b, with the values plotted in Figure 6c. The higher concentrations produced faster and larger maximum velocities, due to the increased current, similar to the electrode size study. The relationship of velocity with concentration of redox species could be complicated by the different net mobilities of ions to compensate for the oxidation at the electrode. Table 1 lists the transference numbers for these different solutions. As redox concentrations dectease the transference number of K^+ and Cl^- increase while the transference number for $Fe(CN)_6^{3-}$ and $Fe(CN)_6^{4-}$ decrease. The changes would result in a slight increase in density gradients at lower concnetrations, assuming the current was the same. In addition, the viscosities of the different solutions can also be different, suppressing natural convection at the higher concentrations.
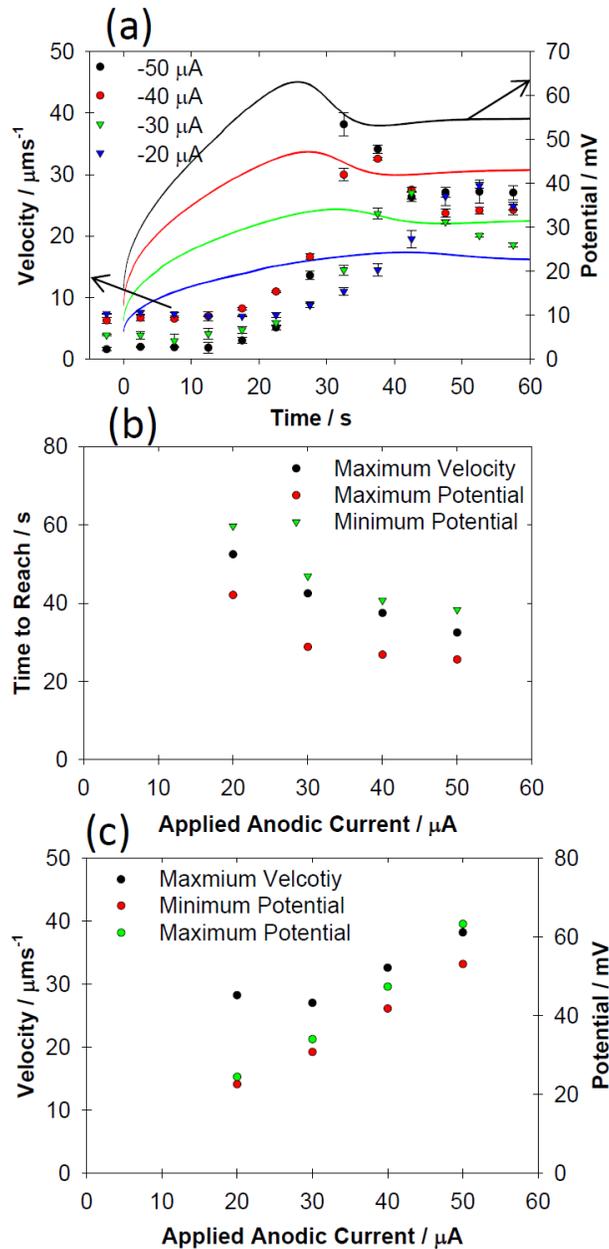
Figure 7. (a) Dependence of potential (solid curves) and fluid movement (markers) on time for different applied anodic currents (-50 μA, -40 μA, -30 μA, and -20 μA). The fluid movement was determined by the speed of beads at a distance of 150 μm from the electrode chip and located 150 μm to the left of where the fluid was rising. (b) The time it takes to reach the maximum velocity, maximum potential, and minimum potential are shown for each applied current, obtained from data in (a). (c) Values of the maximum velocity, maximum potential, and minimum potential are shown for each applied current, obtained from data in (a).

To avoid differences in viscosities and transference numbers that occur for different concentrations, a series of studies was performed where the concentration (at 95.2 mM for $K_3Fe(CN)_6$ and $K_4Fe(CN)_6$) and electrode size (625 µm) were fixed and current was controlled, instead. Figure 7a follows fluid velocity and corresponding changes in potential over time for different applied currents (50 µA, 40 µA, 30 µA, and 20 µA). As with each current response in the applied potential studies, there is a maximum and minimum in each potential response for the applied current studies. In an equimolar solution of $K_3Fe(CN)_6$ and $K_4Fe(CN)_6$ vs. a quasireference electrode in the same solution, the potential at the working electrode should be zero. This is essentially the case for all of the experiments in Figure 7a. As $Fe(CN)_6^{4-}$ is converted to $Fe(CN)_6^{3-}$, the potential shifts more positive, as would be expected based on the Nernst equation ($E = E° +(RT/nF) \ln[(Fe(CN)_6^{3-}]/[Fe(CN)_6^{4-}]$, where $E°$ is the standard electrode potential, R is the idea gas constant, T is the absolute temperature, n is the number of electron equivalents per mole, and F is the Faraday constant). Perturbation to the concentration at the electrode surface because of natural convection would bring a higher concentration of $Fe(CN)_6^{4-}$ from the bulk solution, and shift the potential more negative, resulting in the potential maximum. Further depletion of $Fe(CN)_6^{3-}$ reverses the potential, providing a minimum at t_{min}. These times and the time to reach the maximum velocity are shown in Figure 7b, with the values plotted in Figure 7c. The maximum fluid velocity occurs at a time between t_{max} and t_{min}, with an approximate 5 s delay from t_{max}. As expected, higher currents produced faster and larger maximum velocities. The final velocities (except for the smallest current) are proportional to the applied current.
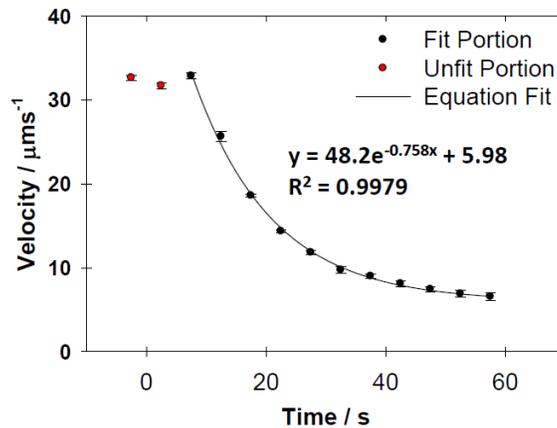
Figure 8. Magnitude of the fluid speed (towards the electrode) with time after the current has ended for the 625 μm wide electrode in figure 5a. The equation $y = Ae^{-Bx} + C$, is fit to the black points, where x is in units of s and y is in units of μm/s and the value for $A = 48.2 \pm 1.3$ μms^{-1} B $= 0.758 \pm 0.0033$ s^{-1}, and $C = 5.98 \pm 0.32$ μms^{-1}, and $R^2 = 0.9979$. The oxidizing potential had been applied for 60 s, when it was turned off

Figure 8, shows density gradient based convention as a function of time after the current has stopped The experiment was a continuation of the 625 μm electrode experiment from Figure 5a. The velocity remains constant for 10 s after the current ended and then decreases exponentially. It has a half-life of 0.914 s. The 10 s delay could be due to the time it takes the less dense fluid to reach the top of the cell where it spreads outward and dissipates. Assuming a velocity of 33 μm/s, which is the horizontal speed, it would take 25 s to travel from the floor to the ceiling of the cell. The actual vertical speed could be faster over the electrode, reaching the top in less time, and the density gradient can be further offset by diffusive equilibration.

To get a better idea of what is going on, a simple Couette flow simulation was conducted, where the bottom plate is moved at a constant velocity until $t = 0$ when the bottom plate stops and fluid movement dissipates due to viscous drag. If density gradient based convection is being dissipated by viscous drag, then this model should reasonably explain the experimental results.

43

Equation 3-119 from White [13], was modified it so it would give the velocity after the bottom plate stops moving at t=0 and substituted out t^* (dimensionless time variable) for vt/h^2 to give equation 7 where h is the cell height (1000 μm), y is the height above the bottom plate, which is where velocity is measured (150 μm), U_0 is the velocity of the bottom plate (40 μm s^{-1}), u is the fluid velocity, and v is the kinematic viscosity for the ferri-ferrocyanide solution used (measured to be 1.022 mm^2 s^{-1} at room temeprature). Values of 1 to 500 were used for n. The bottom plate velocity of 40 μm s^{-1} was chosen so a velocity at 150 μm above the plate would be close to the experimental results at t=0.

$$\frac{u}{U_0} = \frac{2}{\pi} \sum_{n=1}^{\infty} \frac{1}{n} \exp\left(-n^2\pi^2 \frac{vt}{h^2}\right) \sin\frac{n\pi y}{h} \qquad (7)$$

The resulting plot of velocity vs. time is in Figure 9, and does not fit the exponential decay seen in Figure 8. The shape of the curve appears to fit with a velocity remaining constant for a short period of time before dropping off. But, the time remaining constant is much shorter and the drop off is more rapid than the experimental results. Therefore the exponential decay seen is not due to momentum of the fluid being dissipated by viscous drag, but is due to the less dense fluid at the top spreading outward at the lid, and therefore the horizontal motion, slows down. A more detailed model is required to fully describe the experimental results.
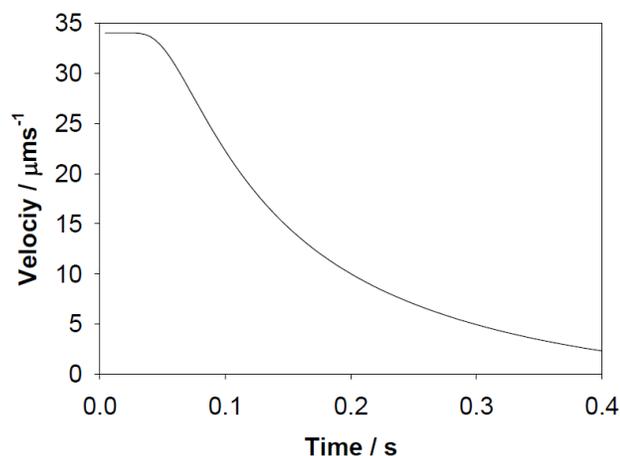
Figure 9. Plot of velocity as a function of time for the simple Couette flow model.

2.5. Conclusions

The effects of convection induced by electrochemically generated density gradients have been studied with band microelectrodes in a microfluidic environment. Because fluid movement was visualized during the electrochemical experiments, a better understanding of natural convection was possible. We have found that natural convection occurs for electrodes of smaller dimensions, for lower concentrations, and at shorter time scales than previously reported by monitoring current alone [14]. Increases in fluid velocity track increases in current, whether it is produced by increased concentration or electrode size at a mass-transport limited applied potential, or by directly applying a constant current. However, the velocity does not necessarily scale linearly with current. The complex interplay of factors can explain these results. For example, mass transfer dominated by diffusion at early times is influenced by natural convection at later times. Also, the transference numbers also evolve while concentration gradients develop. There is also a change in viscosity that will accompany increases in density that will alter the

45

localized fluid velocities. In addition, the close proximity of the lid of the cell plays an important role in determining the overall fluid circulation. Computer simulations of these systems are especially needed for a more quantitative understanding. Nonetheless, these multiple factors provide a great deal of flexibility in tuning the magnitude of convection for microfluidic applications.

2.6. Acknowledgements

2.7. References

[1] X.P. Gao, J. Lee, H.S. White, Natural-Convection at Microelectrodes, Analytical Chemistry, 67 (1995) 1541-1545.

[2] C. Amatore, C. Pebay, L. Thouin, A.F. Wang, Cyclic Voltammetry at Microelectrodes. Influence of Natural Convection on Diffusion Layers as Characterized by in Situ Mapping of Concentration Profiles, Electrochemistry Communications, 11 (2009) 1269-1272.

[3] C. Amatore, C. Pebay, L. Thouin, A.F. Wang, J.S. Warkocz, Difference between Ultramicroelectrodes and Microelectrodes: Influence of Natural Convection, Analytical Chemistry, 82 (2010) 6933-6939.

[4] E.C. Anderson, M.C. Weston, I. Fritsch, Investigations of Redox Magnetohydrodynamic Fluid Flow at Microelectrode Arrays Using Microbeads, Analytical Chemistry, 82 (2010) 2643-2651.

[5] V. Sahore, Microfluidics Guided by Redox-Magnetohydrodynamics (MHD) for Lab-on-a-Chip Applications, University of Arkansas, Ann Arbor, 2013, pp. 235.

[6] V. Sahore, A. Kreidermacher, I. Fritsch, Electrochemically Generated Density Gradient-Induced Natural Convection in Microfluidic Systems, Journal of Electrochemical Society, (2015) in preperation.

[7] M.C. Weston, I. Fritsch, Manipulating Fluid Flow on a Chip Through Controlled-Current Redox Magnetohydrodynamics, Sensors and Actuators B-Chemical, 173 (2012) 935-944.

[8] P.H. Kao, R.J. Yang, Simulating Oscillatory Flows in Rayleigh-Benard Convection Using the Lattice Boltzmann Method, Int. J. Heat Mass Transf., 50 (2007) 3315-3328.

[9] P.G. Scrape, M.D. Gerner, M.C. Weston, I. Fritsch, Redox-Magnetohydrodynamics for Microfluidic Control: Remote from Active Electrodes and Their Diffusion Layers, Journal of The Electrochemical Society, 160 (2013) H338-H343.

[10] C.K. Nash, Modified-Electrodes for Redox-Magnetohydrodynamic (MHD) Pumping for Microfluidic Applications, Chemistry and Biochemistry, University of Arkansas, 2014.

[11] A.J. Bard, L.R. Faulkner, Electrochemical Methods : Fundamentals and Applications, 2nd ed ed., Wiley, New York, 2001.

[12] V.M. Volgin, A.D. Davydov, Natural-Convective Instability of Electrochemical Systems: A Review, Russian Journal of Electrochemistry, 42 (2006) 567-608.

[13] F.M. White, Viscous Fluid Flow Third Edition, McGraw-Hill Higher Eduation, New York NY, 2006.

[14] K. Ngamchuea, S. Eloul, K. Tschulik, R.G. Compton, Advancing from Rules of Thumb: Quantifying the Effects of Small Density Changes in Mass Transport to Electrodes. Understanding Natural Convection, Analytical Chemistry, (2015).

3. 3D Imaging of Flow Patterns in an Internally-Pumped Microfluidic Device: Redox Magnetohydrodynamics and Electrochemically-Generated Density Gradients

Reproduced with permission from

F. Gao, A. Kreidermacher, I. Fritsch, C.D. Heyes, 3D Imaging of Flow Patterns in an Internally-Pumped Microfluidic Device: Redox Magnetohydrodynamics and Electrochemically-Generated Density Gradients, Analytical Chemistry, 85 (2013) 4414-4422.

3.1 Abstract

Redox magnetohydrodynamics (MHD) is a promising technique for developing new electrochemical-based microfluidic flow devices with unique capabilities, such as easily switching flow direction and adjusting flow speeds and flow patterns as well as avoiding bubble formation. However, a detailed description of all the forces involved and predicting flow patterns in confined geometries is lacking. In addition to redox-MHD, density gradients caused by the redox reactions also play important roles. Flow in these devices with small fluid volumes has mainly been characterized by following microbead motion by optical microscopy either by particle tracking velocimetry (PTV) or by processing the microbead images by particle image velocimetry (PIV) software. This approach has limitations in spatial resolution and dimensionality. Here we use fluorescence correlation spectroscopy (FCS) to quantitatively and accurately measure flow speeds and patterns in the ~5−50 μm/s range in redox-MHD-based microfluidic devices, from which 3D flow maps are obtained with a spatial resolution down to 2 μm. The 2 μm spatial resolution flow speeds map revealed detailed flow profiles during redox-MHD in which the velocity increases linearly from above the electrode and reaches a plateau across the center of the cell. By combining FCS and video-microscopy (with PTV and PIV processing approaches), we are able to quantify a vertical flow of ~10 μm/s above the electrodes as a result of density gradients caused by the redox reactions and follow convection flow patterns. Overall, combining FCS, PIV, and PTV analysis of redox-MHD is a powerful combination to more thoroughly characterize the underlying forces in these promising microfluidic devices.

3.2. Introduction

Microfluidic devices are of interest for a range of analytical applications in chemistry, physics, and the life sciences and involve handling small volumes of fluids in confined spaces. While mechanical pumps are usually used for controlling the fluid flow, they can be quite expensive and difficult to miniaturize, and, due to the required pressure, the coupling of the pump to the channel can be the least controllable aspect of the device [1]. These drawbacks of mechanical pumps generally complicate the engineering of microfluidic devices. The electroosmotic approach for directing fluid flow is growing in popularity and does not share these drawbacks, but the fluid velocity is sensitive to the physicochemical properties of the walls along the flow path and is most suitable for narrow cross sections (up to ∼100 μm) [2, 3]. One novel way of achieving localized control of solution flow without moving parts, with fluid velocities similar to electroosmotic pumping (a few μm/s to a few mm/s) but over larger volumes, and without the requirement for sidewalls is by magnetohydrodynamics (MHD) [4, 5]. MHD-based fluid flow is the result of the (body) force, $\mathbf{F_B}$, induced by the cross product of an ionic current density, $\mathbf{j}$, and a magnetic flux density, $\mathbf{B}$, and obeys the right hand rule [6-8].

$$\mathbf{F} = \mathbf{j} \times \mathbf{B} \qquad (1)$$

(See footnotes in ref [9] for choice of notation.)

Redox-MHD offers unique capabilities; it avoids bubble formation and electrode corrosion because the ionic current, $\mathbf{j}$, results from electroactive redox species added to the system that oxidize and reduce at the electrodes [10-12]. A variety of fluid compositions are compatible with electrochemistry, and thus pumping both aqueous and nonaqueous solutions is

possible. Redox-MHD has the flexibility of creating flow patterns simply by activating different electrodes on the device in a programmable fashion [9]. Thus, it can switch flow direction easily and has the capability to mix fluids under laminar flow conditions. Also, by controlling the current, it can finely tune fluid velocities to a few μm/s [13].

However, quantitatively predicting flow velocities from eq 1 in a microfluidic system caused by redox-MHD is not an easy task. First, calculating the ionic current density in a particular region of space at a particular time, $\mathbf{j}$(x,y,z,t), in an asymmetric electrochemical cell, based on the net current passing through the electrodes, is not trivial. Second, the geometry of the system, including wall placement relative to the location of active electrodes, greatly affects the flow pattern and velocity. Quantifying velocity in small volumes from picoliters to microliters with micrometer spatial resolution is needed to study the different forces that affect solution flow and mixing and to guide the design of new redox-magnetoconvective-based microfluidic devices.

An attractive method to evaluate fluid flow in such small systems can be accomplished by directly visualizing particles in the flow path using particle image velocimetry (PIV) or single particle tracking velocimetry (PTV) analysis. Guidelines for and the use of particle image velocimetry (PIV) to follow fluid flow have been reviewed [14, 15]. The emphasis in PIV has been on two dimensional visualization. Demonstration of PIV in two dimensions for very high spatial resolution (1 μm) in a microfluidic device was reported by Meinhart et al. [16]. using only one observation window and 200 nm diameter particles, but more typical PIV measurements are limited to 1 μm particles and therefore poorer resolution (see ref [17] and references therein). There remains a strong need for three dimensional imaging, especially for more complex microfluidic systems having asymmetry in terms of geometry or applied forces, such as in the

redox-MHD device described herein. The advantages and disadvantages for particle imaging methods for microfluidics in three dimensions have been recently reviewed by Cierpka and Kahler [17].

In systems involving magnetoconvective effects in small volumes containing redox species, there are only a few reports of visualizing fluid flow using tracer particles or microbeads [9, 18-21]. A promising approach is astigmatism PTV, which requires only one observation window and a single camera [22]. Visualization at a 30 μm spatial resolution was demonstrated, using 5 μm fluorescent beads in a 500 μm wide channel and conventional pumping. This method has been used to image magnetoconvective fluid flow in three dimensions but in a cell of much larger dimensions, $10 \times 10 \times 20$ mm3, than is typical for a microfluidic device [20]. Higher resolution imaging in devices having smaller dimensions remains challenging. Koenig et al. [18] describe a laser Doppler profile sensor that promises submicrometer spatial resolution with a long-working distance to assess microenvironments in larger volumes. However, velocity profiles in a magnetoconvective system were only demonstrated at 15 μm spatial resolution with 2 μm fluorescent particles, also in a relatively large volume of a 20 mm cuboid cell. Very low concentrations of particles were necessary so that only a single tracer particle was present in the measurement volume at a time. With this low data rate, time-resolved velocities (2.5 s) were possible only at a fixed position (200 μm ± 25 μm from the electrode) and required large numbers of replicates (25×). In that same paper (Koenig), PIV was used to validate the Doppler approach. Although in theory, these other approaches are capable of measuring fluid flow in smaller cells, the smallest cells involving magnetoconvection that have been studied thus far (350 μm deep cell9) have used the simple method of tracking individual 10 μm microbeads with optical video microscopy with an estimated depth of correlation of about ≥20 μm and a lateral

resolution of about ≥10 μm. Although such particle tracking is highly accurate, it is very time-consuming, especially when overall fluid flow patterns in a single image need to be visualized, and it only provides two dimensional, two-component velocity information (2D2C) and three-dimensional, two-component velocities (3D2C) through acquiring data by focusing at different heights. We have recently demonstrated that the videos can be processed with software used for PIV to visualize flow patterns in 2D more easily, although the spatial resolution decreases because of the need to follow groups of beads and the effect of following blurred bead movement above and below the focal plane [23]. (Note that from here on, we will use the term "PIV" to refer to the processing of optical microscopy videos of microbeads.)

Fluorescence correlation spectroscopy (FCS) offers both high sensitivity and high spatial resolution [24-26], because it uses a diffraction-limited focal volume in all three dimensions and fluorescence detection. It has been shown that FCS can be used to obtain quantitative and accurate flow velocity maps in 3D in microfluidic devices [27-35]. In most literature reports, fluid motion has been imaged within devices employing mechanical pumps with relatively high flow speeds of 50 μm/s−10 cm/s. Additionally, flow direction information can be obtained using dual-focus30 FCS and fast imaging times can be realized using a spinning disk confocal microscopy setup [36], although these instruments require more technical expertise or are more expensive than conventional FCS, which can be performed on any scanning confocal fluorescence microscope (SCFM). The optimization and limitations of FCS for measuring flow has been systematically studied for microfluidic devices with pumps using compressed N2 or gravity for velocities between hundreds of μm/s and hundreds of mm/s [36], but such optimization has not yet been done for the slower flow velocities that are accessible by redox-MHD.

Here we used a SCFM and conventional FCS to image 3D flow patterns of a microelectrode array-based, redox-MHD microfluidic device and obtained accurate flow velocities from 5 to 50 μm/s and at 2 μm spatial resolution. We combined FCS and optical video microscopy/PIV-processing approaches to both validate our data and to obtain directional information. We verify that, when using bead sizes that are compatible with both FCS and PIV (1 μm), the same velocities are obtained but that FCS also provides 3D information at higher spatial resolution and can extract the vertical component of velocity. The 2 μm spatial resolution flow map obtained by FCS revealed a flow profile between the active electrodes that increases rapidly and reaches a plateau across the center of the redox-MHD flow channel. Moreover, because the third, vertical component of the velocity can be extracted from the combination of FCS and PIV, we are also able to quantify flow due to convection caused by the electrochemically generated density gradients in small sample volumes ($\sim$30 μL) directly over the electrodes. Overall, this unique combination of electrochemical pumping and optical analytical techniques allows us to obtain low fluid flow velocities (down to a few μm/s) with novel flow profiles and to accurately quantify both flow speed and direction with high spatial resolution in 3D, all with relatively simple experimental apparatuses.

3. Experimental

Complete experimental details are provided in the Appendix. Briefly, FCS is acquired using a Microtime 200 microscope (Picoquant GmbH, Berlin, Germany). This system consists of a 3D piezo scanner (PI, Berlin, Germany) with subnanometer spatial resolution, 485 and 640 nm DPSS lasers (Picoquant), a UplanApo 60x/1.3W objective (Olympus, Japan), a 100 μm pinhole and single photon avalanche diode (SPAD) detectors (MPI, Microphotonic devices, Bolzano,Italy) [37]. 3D imaging is performed by taking fluorescence intensity traces as a

function of time at multiple points in the X−Y plane at a given Z position, adjusting the Z

position and repeating the trace collection until all the required X-Y-Z coordinates have been

sampled. The schematic of the microfluidic setup as monitored by FCS is given in Figure S1. A

user macro was written in SymPhoTime (Picoquant) to calculate and extract the FCS curves

from each trace. Homemade software was written in Igor Pro (WaveMetrics, Inc., Oregon) to

import the extracted FCS traces and fit each with a combined diffusion and flow model [34], as

follows

$$
G(\tau) = G(0) \cdot \frac{1}{\left(1 + \frac{\tau}{\tau_D}\right)\left(\left(1 + \left(a^{-2}\right)\frac{\tau}{\tau_D}\right)^{1/2}\right)} \cdot \exp\left\{-\left(\frac{\left(v_x^2 + v_y^2\right)\tau^2}{r_0^2}\right) \cdot \frac{1}{1 + \frac{\tau}{\tau_D}}\right\} \cdot
$$

$$
\exp\left\{-\left(\frac{\left(v_z^2\right)\tau^2}{z_0^2}\right) \cdot \frac{1}{1 + \left(a^{-2}\right)\frac{\tau}{\tau_D}}\right\} + G(\infty) \tag{2}
$$

where τ represents the correlation lag time, τ_D represents the bead diffusion time in the confocal

laser focus, and v_x, v_y, and v_z represent the flow speeds through the laser focus in the X, Y, and Z

axis. $a = z_0/r_0$ is the elongation of the detection volume in the Z axis relative to the X-Y axes and

is used to describe 3D diffusion. r_0 is the Gaussian laser focus waist in the X or Y axis, and z_0 is

the Gaussian laser focus waist in the Z axis. G(0) is the amplitude of the autocorrelation function

at $\tau = 0$, which is equal to $1/<N>$ ($<N>$ is the average number of beads in the laser focus), and G(

∞) is the amplitude of the correlation function for the largest τ (chosen so that $G(\infty)$ is usually

0). In our experiments, eq 2 is simplified by setting $v^z = 0$ for horizontal flow or $v_x = 0$ and $v_y = 0$

for vertical flow, as discussed later and in the Appendix.

For PIV/PTV analysis, bead movement was observed with a Nikon Eclipse ME600P microscope equipped with a CF plan 10×/0.30 objective, and videos were recorded using a Sony Handycam digital camera (model no. HDR-XR500V, 30 frames/s with 720 × 480 pixels/frame). The microscope was focused halfway between the microelectrode chip and coverslip, and the viewing region was centered halfway between the active electrodes. DynamicStudio v.3.00 software (Dantec Dynamics, Copenhagen, Denmark) was used to obtain flow velocities. These were depicted graphically using PrestoVectors, a software developed previously by us [23], so that vector length and color are coded according to their speed.

3.4. Results and Discussion

3.4.1. Properties of the Microfluidic Device.

In this study, we use the term microfluidic device in its most general sense of having at least one dimension on the micrometer length scale (in this case, z). The height of the microfluidic cell used here is ~200 μm, which is smaller than has been reported for redox-MHD devices. This allows us to take advantage of the high resolution 3D imaging capabilities to evaluate redox-MHD fluid flow in strongly confined geometries, which holds promise for highly efficient, low-volume lab-on-a-chip applications, and yet is relatively unexplored. Figure 1 shows images of the microelectrode array chip used at various magnifications.

Figure 1(a) shows the whole microelectrode array chip, where the individually addressable contact pads are connected via leads to individual electrodes in the microelectrode array. Figure 1(b) is an optical image of the microelectrode array. Figures 1 (c) and (d) were acquired at higher magnification using the SCFM by monitoring the reflection of a 640 nm laser. The 640 nm light is not absorbed by the fluorescent beads in the solution but is reflected strongly by the gold

electrodes, and less so from the silica substrate, providing in situ (i.e., with the fluorescent beads already loaded) high resolution imaging of the electrodes. Based on these images, it is verified that the electrodes have widths of ~40 μm and center-to-center distances of ~100 μm between two adjacent electrodes, consistent with the design parameters for the microelectrode array chip. In our FCS setup, the electrodes run parallel to the Y axis, and, thus, once the microelectrode array is imaged, we identified and numbered electrodes from left to right in the X axis by manually moving the microscope stage in 100 μm intervals to set up the imaging coordinates.
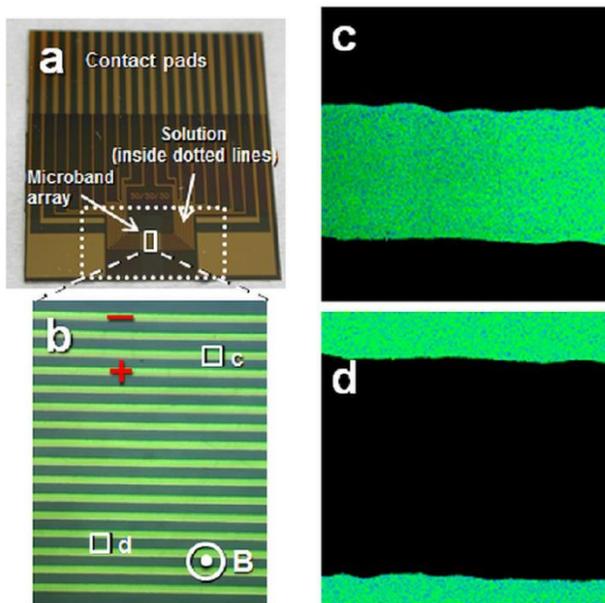
Figure 1. (a) Image of complete microelectrode chip. (b) 10× magnification of microelectrode array region of chip. (c) and (d) 60× magnification of a single electrode and the gap between 2 electrodes obtained using reflected 640 nm laser light with a total imaging area of 80 μm × 80 μm. The edge−edge distance for the two neighbor electrodes are ~60 μm, and the electrode width is ~40 μm. In (b) the cathode and anode are labeled with − and +, respectively. In order to minimize the depletion of redox species at the electrodes, switching of the polarity of the electrodes alternately after each Z slice, which changes the direction of the ionic current, is used during 3D FCS flow speed imaging (Figure S4). The direction of the magnetic field is also given.

A reinforcing flow configuration, where parallel microband electrodes are oppositely polarized, was selected, as it has a flow profile that has been recently characterized [9]. It also results in unidirectional flow to simplify the assignment of flow vectors. Furthermore, a two-electrode configuration was used, rather than using more distant large counter and reference electrodes on the chip [38], to confine the electric field to a narrow, well defined region in the microfluidic device. Finally, the electronic current (at a constant applied voltage) as a function of time was determined (Figure S2). The current decreases rapidly within the first 20 s after applying the potential and then reaches a relatively stable value; thus velocities were only determined after this initial 20 s settling time. It was also found that activating electrodes 1 and 4, which have a separation of ~260 μm provided the maximum flow velocity for this device, as determined by video microscopy and PIV analysis (Figure S3). A trend of increased speed with electrode separation, followed by a subsequent decrease with increased spacing was observed and is consistent with previous studies [9, 38], although the exact maximum of 260 μm separation observed is less than previous studies, a consequence of the smaller device dimensions used here. All our subsequent experiments are carried out using electrodes 1 and 4 as the active electrodes.

3.4.2. Optimization of FCS Parameters.

The major goals of this research are to (1) demonstrate that a combined FCS and PIV analysis can be used to simply and accurately quantify flowpatterns in a novel electrochemically pumped (redox-MHD) microfluidic device, (2) evaluate the limits of velocity sensitivity for such analyses, and (3) extend the quantification to three-dimensional convective forces resulting from electrochemically generated density gradients above the electrodes. In order to accomplish these goals, it is necessary to optimize the conditions to ensure comparisons between the analytical

methods are valid and that the effects of experimental variables are thoroughly understood. While the optimization of FCS parameters have been previously reported for diffusing species [39] and pressure-pumped microfluidic devices with relatively fast flow velocities [36], it has not been studied for redox-MHD-based microfluidic devices, and particularly for flow velocities below ~100 μm/s.
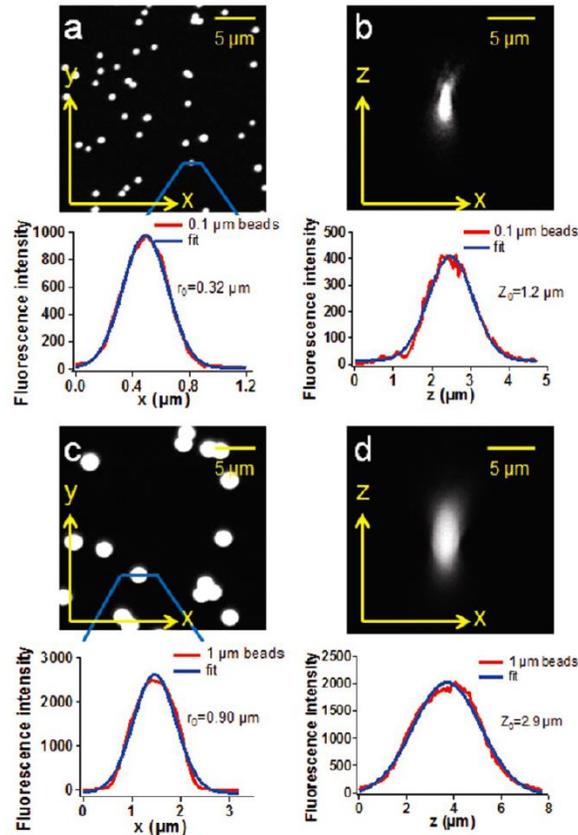
Figure 2. Fluorescence intensity images of (a, b) 0.1 μm and (c, d) 1 μm immobilized beads. (a) and (c) are X-Y scans, and (b) and (d) are X-Z scans showing the 3D point spread functions (PSF). The r_0 values to be used in eq 2 are 0.32 and 0.9 μm for 0.1 μm beads and 1 μm beads, respectively. The z_0 values are 1.2 and 2.9 μm for 0.1 μm beads and 1 μm beads, respectively.

FCS analysis requires knowledge of the effective illumination width, r_0, and height, z_0, for each fluorescent species. To determine these parameters, we immobilized two different sized beads (0.1 and 1 μm) on a glass coverslip at high dilution and imaged them (Figure 2). As

expected, the 0.1 μm beads appeared as diffraction-limited spots with r0 = 0.32 μm – the width of the beam profile at $1/e^2$ of the maximum intensity. For the 1 μm beads, r_0 is 0.90 μm. That is to say that, although the diffraction-limited confocal laser focus is only ~0.3 μm wide, the 1 μm bead will be illuminated for the whole 0.9 μm distance that is excited by the laser. This is an important parameter in order to extract the flow velocity from eq 2. In order to calculate 3D diffusion and to perform vertical flow analysis, we also need to know the waist of the beam in the Z axis. An X-Z scan of the immobilized beads was acquired, and a value of z0 = 1.2 μm for 0.1 μm beads and 2.9 μm for 1 μm beads was found; the larger z0 for the 1 μm beads is expected due to the convolution of the bead with the similarly sized Gaussian illumination beam in the Z axis.

For 0.1 μm beads in the absence of an applied voltage, the obtained FCS curves can be fit to a diffusion-only model with υ_x, υ_y, and υ_z =0 (Figure S5, red curve). With 0.1 μm beads in the presence of an applied voltage and magnet, the beads can both diffuse and flow by redox-MHD (Figure S5, blue curve). The 1 μm beads are too large to show diffusion on these time scales and thus show no autocorrelation function in the absence of an applied voltage. In the presence of an applied voltage, they show only flow (i.e., $\tau_D \approx \infty$ in eq 2) (Figure S5, green curve). The fact that the FCS curves show excellent fits to this equation supports our expectation that redox-MHD based solution flow is laminar along the microelectrode direction perpendicular to the optical axis and will be further supported with particle tracking methods below.

It is well-known that collection statistics for FCS influence the signal:noise ratio; the noise in the FCS curves (Figure S5) not only decreases as the square root of the collection time but also depends on other experimental parameters such as binning time and fluorophore

concentration and brightness[36, 39]. The duration of each FCS point collection time multiplied

by how many points are collected determines both the total collection time and the error in the

recovered diffusion and flow parameters. It is important to balance the experimental time with

obtaining enough statistics for accurate recovery of the flow and/or diffusion, and it is not

immediately obvious what this balance should be. There are two origins of error that need to be

quantified: relative standard deviation between multiple measurements and the error from the

least-squares fitting of the collected FCS curve to eq 2. Figures S6 and S7 characterize the

relative standard deviation (RSD) and the fitting errors associated with taking multiple

measurements as a function of measurement time, when both flow speeds and diffusion

coefficients (τD) of 0.1 μm beads are considered as variables and allowed to be fitted during the

FCS curve fitting. For any given measurement time, the RSD is higher than the fitting error,

although both increase sharply as measurement time decreases below 30 s. RSDs do not drop

much below 10−20% RSD even for long (>100 s) measurement times, while the fitting error is

already <3% at 30 s and continues to drop as measurement time increases. Based on the results

of Figures S6 and S7, we choose a 30 s collection time per point and took 30 μm steps for a wide

field of view and 2 μm steps for higher spatial resolution imaging with a smaller field of view. In

principle, one can collect wide fields of view with high spatial resolution and longer trace length,

but the experimental time would increase accordingly. The FCS imaging process can be

automated to achieve this goal, if required.

In principle, one can either fix the diffusion coefficient, D, and fit only for the flow speed

or simultaneously fit for both parameters in eq 2. We performed both types of analysis and found

that the recovered velocity converges less, and the fitting error is larger when D is fixed rather

than fitted (Figure S8). The reason for this is that there is an inherent error in the recovered D

values, due to the limited statistics (Figure S9), which is compounded to the fitting error in the velocity when it is fixed to an average value. We also confirmed that bead movement between the active electrodes 1 and 4 (in the xdirection) due to electrophoresis is negligible (Figure S10), and therefore the recovered bead flow speeds from FCS and PIV represents flow resulting from redox-MHD.

3.4.3. 3D Imaging of Redox-MHD Flow.

Once the microfluidic device, microscope, and experimental parameters were characterized, we obtained 3D flow maps of the redox-MHD flow in our highly confined geometries. We plot the 3D flow velocity and diffusion coefficient maps from the 0.1 μm beads in solution in Figure 3. The flow velocity varied in all three dimensions but was not parabolic. The highest velocity was recorded closer to the electrode surface than the coverslip surface (the 60 μm plane of a 180 μm thick cell) and was ∼50−60 μm/s, decreasing to 0−10 μm/s at the surfaces and above the active electrodes (labeled as 1 and 4 above the maps). In the central Z plane (90 μm), the flow profile was somewhat flatter, which was supported with higher spatial resolution imaging (as will be shown below). Extracting this flow profile asymmetry in the Z axis highlights the importance of performing 3D imaging of microfluidic cells, which is easily realized using FCS. The diffusion coefficient was 2−5 μm2/s and showed minimal variation across the device, as would be expected, and is in agreement with that expected from the Stokes−Einstein relationship for 0.1 μm spherical particles (∼3 μm2/s). In the Supporting Information, we also provide the fitting errors in both velocity and diffusion coefficient associated with each pixel (Figure S11). The error in the diffusion coefficient is relatively homogeneous across the cell, remaining at 10−20%. The error in the fitted velocity remains at 10−20% until the velocity drops below ∼5 μm/s.
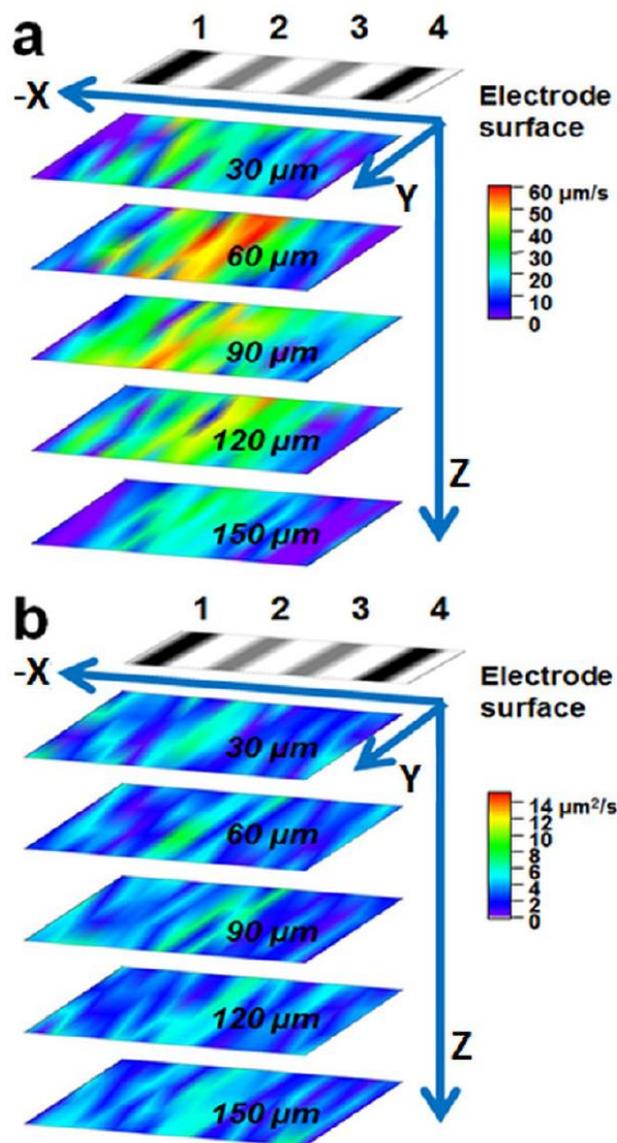
Figure 3. 3D maps for (a) flow speeds and (b) diffusion coefficient obtained from 0.1 μm beads in redox-MHD microfluidic flow cell. The spatial resolution in the X−Y plane is 20 μm and is 30 μm in Z. The relative position of the microelectrodes is also shown above the flow maps. Black colored electrodes are the active electrodes, and gray are the nonactive electrodes. The thickness of the microfluidic cell is ∼180 μm.

The 0.1 μm beads are not visible by optical microscopy for PIV or PTV analysis.

Therefore, in order to compare the FCS results with these more common techniques, we obtained

a 3D flow velocity map using 1 μm beads. Since 1 μm beads show negligible diffusion (based on

the Stokes−Einstein equation, we estimated 1 μm beads to have D ~0.3 μm^2/s), it also allows us to probe the dependency between fitted diffusion coefficients and flow velocities. The flow velocity and error maps are plotted in Figure S12, showing a very similar flow map as for 0.1 μm beads (Figure 3), including the asymmetry in the Z axis, but highlighting negligible dependency on the fitted parameters.

For both flow maps, there are a few discontinuous pixels. A number of sources may account for this, including bead heterogeneity (both in size and brightness) and data collection statistical fluctuations caused by the limited FCS trace collection time and the low bead concentration (this effect is much more obvious for 1 μm beads since they have lower concentration and stronger scattering), as well as possible fluctuations in flow velocities resulting from variations in the rates of oxidation and reduction of the redox species. This latter effect has been quantified in the Supporting Information (Figure S13). From Figure S13, the histograms for fitted flow velocities over time are not symmetric around the average value, showing skew toward lower velocities. This asymmetry may be indicative of fluctuations in the flow caused by the temporal decrease in the current magnitude but requires further study to quantify in more detail. However, this result does suggest that it may be one source of the discontinuity in the pixels obtained in the 3D flow maps.

3.4.4. High Spatial Resolution Imaging of Redox-MHD Flow by FCS.

To highlight the information that can be gleaned from a high spatial resolution imaging approach, as can be obtained from FCS, a 2 μm spatial resolution map of a 20 μm × 160 μm region is imaged in 2D (Figure 4). The diffusion coefficient of beads in each pixel is provided in the Appendix (Figure S14). This 2 μm resolution map shows a more detailed flow profile from
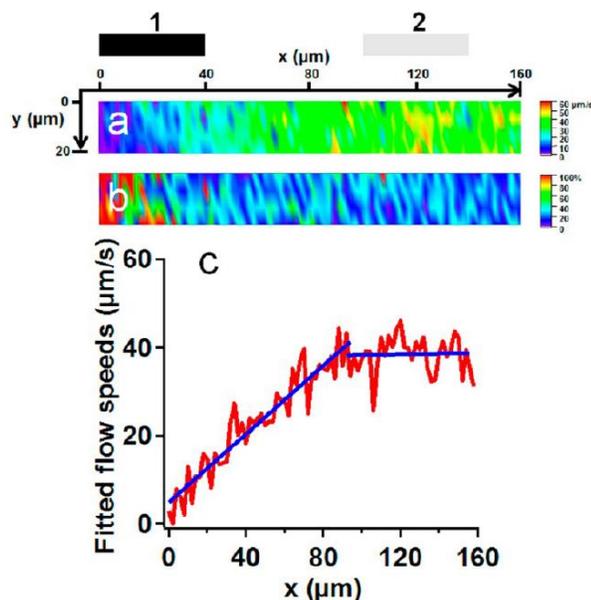
Figure 4. (a) High-resolution (2 μm in X and 5 μm in Y) imaging of redox-MHD flow for a 160 μm × 20 μm area in the X-Y plane, acquired at the center Z-slice of the channel. The position of the active electrode 1 and nonactive electrode 2 are also shown for comparison to the lower resolution, wider field images in Figure 3. (b) Flow speed fitting error map from (a). (c) Flow profile as a function of horizontal distance from the active electrode 1. The dependence linearly increases between 0 and 100 μm and reaches a plateau between 100 and 160 μm.

the central z plane (90 μm), which increases in a linear fashion from 0 to 100 μm (0 being above the active electrode) and then reaches a plateau from 100 to 160 μm (the left half of the channel). The level of detail in the flow profile over the X axis is not as clearly observable in the lower resolution flow maps (with spatial resolution of ~20−30 μm) and highlights the importance of high resolution imaging in revealing the detailed flow patterns in redox-MHD based microfluidic flow cell. To the best of our knowledge, this is the first time that such high resolution imaging in such a strongly confined redox-MHD microfluidic cell has been obtained, which has been realized by the application of FCS. It is interesting that a relatively flat flow profile in the center of the channel can be obtained in such confined geometries and may be promising for a range of applications in the bioanalytical and separation sciences.

3.4.5. Comparison of Redox-MHD Fluid Flow Obtained by FCS and PTV/PIV.

A major reason to image the 1 μm beads by FCS is that, unlike 0.1 μm beads, this size is also visible by wide-field optical video microscopy and can be tracked. Bead tracking with video microscopy is usually performed with larger beads in the range of 5−10 μm for easier visualization [9, 38], but 1 μm beads can be analyzed in this way. To compare, we imaged both 1 and 6 μm beads using video microscopy and performed two types of particle tracking analysis (PIV and PTV). Figure 5 shows the PTV and PIV images and analysis from the redox-MHD flow using 6 and 1 μm beads. As shown in Figure 5, PIV provides a 2D flow velocity map of a large ~1 mm2 area in a single X−Y plane and with a spatial resolution of ~60 μm. The flow velocity maps show that the flow velocities in the center of the cell for both 6 and 1 μm beads are ~50−60 μm/s, consistent with the velocities in the center of the cell obtained in the FCS flow maps (Figure 3). We also observe a slight dependence on bead size, just as we did between the 0.1 and 1 μm beads in FCS. The flow velocity decreases across the X axis from a maximum in the center of the cell toward electrodes 1 and 4 (the active electrodes). Particle tracking velocimetry (PTV) verifies that the velocity of the 6 μm beads gives consistent velocities as those obtained by PIV (Figure 5(b)) when the same sized bead is used.

Table 1. Summary of average flow speeds in center of the channel, determined using different methods.

Method	Bead Speed		
	10μm	1μm	0.1μm
Bead tracking	62 ± 2 μm/s	NA	NA
PIV	58 ± 4 μm/s	52 ± 1 μm/s	NA
FCS	NA	52 ± 3 μm/s	44 ± 6 μm/s

In order to quantitatively compare the data from each method, we used the 60 and 90 μm Z axis layers from the 3D flow maps obtained from FCS because they correspond to the same

imaging region in which the PIV and PTV data were collected. As can be seen from Table 1, the comparison of flow velocities for the 1 μm beads analyzed by FCS and PIV shows consistent results. However, a size dependence on the recovered flow velocities is present for all methods. Surprisingly, the larger beads seem to consistently recover faster velocities, contrary to intuition. It is not yet clear to us why we should see this effect and plan to investigate it further.

One possibility is that the 6 μm beads are sulfonated while the 1 and 0.1 μm beads are carboxylated, but the fact that the size trend is also present between 1 and 0.1 μm beads suggests other factors are involved. Another possibility is that the negatively charged groups of the beads (sulfonate or carboxylate) interact with the flowing electrolytes, leading to reduced friction between the flowing K^+ ions and the negatively charged beads.
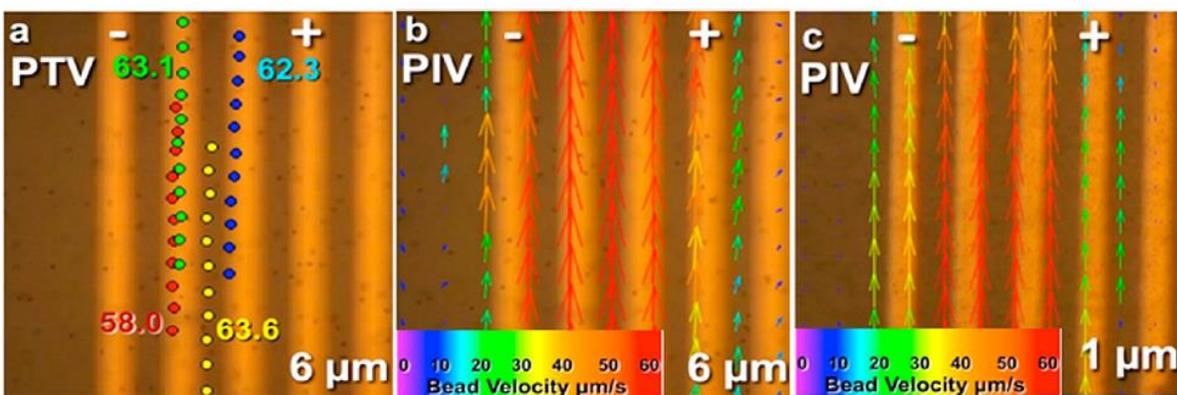
Figure 5. Video microscopy images showing 2D redox-MHD flow imaged using (a) PTV with 6 μm beads and PIV with (b) 6 μm beads and (c) 1 μm beads. PTV shows the trajectory of 4 individual beads, while PIV shows the average velocity of beads within a 50 μm region, plotted as color coded vectors. The cathode and anode are labeled with − and +, respectively. The other electrodes are inactive.

Overall, particle tracking analyses using PIV and PTV have the advantage of visualizing the solution flow in a larger area (1 mm × 1 mm scale) in real time and provide flow direction information but only offer spatial resolution of ∼20−150 μm and in only two dimensions. FCS

has the advantage of high spatial resolution in all three dimensions, although it does not provide

directional information without using a more complex setup, such as dual focus [30]. Combining

these approaches is a powerful combination to provide a more complete characterization of flow

patterns in such microfluidic devices.

3.4.6. Electrochemically Generated Density Gradients Measured with FCS.
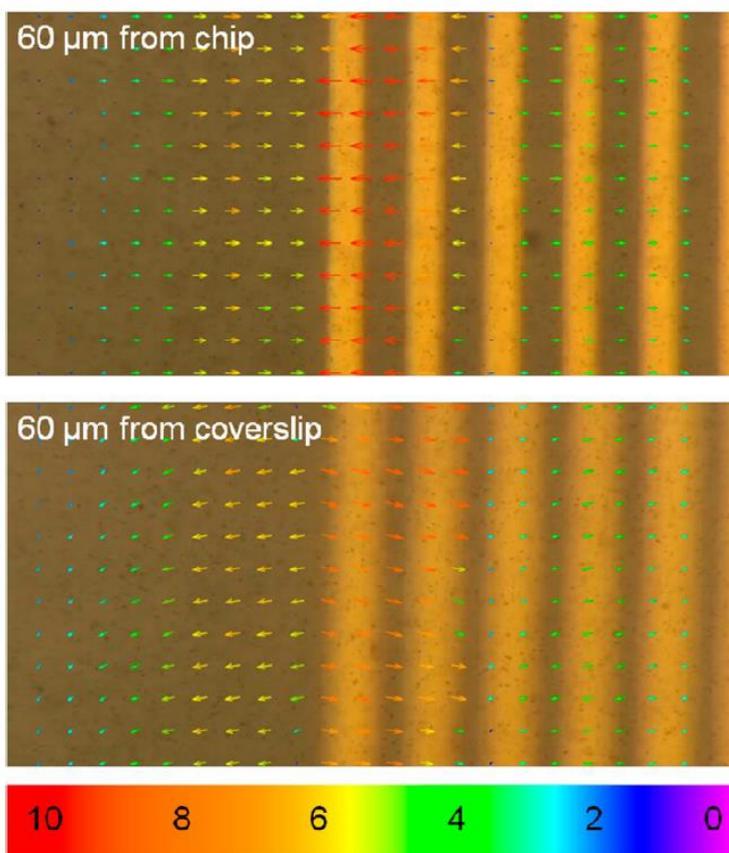
Figure 6. PIV images showing 2D density gradient flow acquired with current but without magnet. The color bar shows the bead speed in μm/s. The electrochemical cell orientation for the PIV/PTV microscope setup is inverted from that in Figure S1 and electrodes1 and 4 served as the anode and cathode, respectively. Therefore, fluid rises over the anode and falls over the cathode, resulting in convection with the same flow direction as that in Figure 7, where the orientation and polarity of the electrodes were reversed.

There is another force involved in redox-MHD flow, which is the convective force caused by density gradients. The density gradients are electrochemically generated during the redox reaction of $Fe(CN)_6^{3-}$ to $Fe(CN)_6^{4-}$ at the cathode and $Fe(CN)_6^{4-}$ to $Fe(CN)_6^{3-}$ at the anode. A slight density difference of fluid elements containing $Fe(CN)_6^{3-}$ and $Fe(CN)_6^{4-}$ is due to movement of the additional K+ counterions needed to balance the accumulated, reduced $Fe(CN)_6^{4-}$ at the cathode or the movement away of the extra K^+ from the oxidized $Fe(CN)_6^{3-}$ at the anode will cause convection in the microfluidic flow cell. In order to follow this process, we performed the experiments under an applied voltage, but without the magnet, and thus redox-MHD will not occur. PIV and/or PTV analysis can be used to follow the horizontal flow, while FCS can be used to quantify both horizontal and vertical flow, based on eq 2. Figure 6 shows the PIV imaging data for the horizontal flow caused by the density gradients. A horizontal flow velocity of ∼10 μm/s is observed close to the electrodes, both near the chip and coverslip surfaces. The flow rapidly decreases as a function of distance from the active electrode. The inverse flow direction near the top and bottom surfaces is strongly indicative of convective flow in the microfluidic flow cell. Using PIV, we are not able to see vertical flow, since the beads move out of focus and become difficult to track. Here, we take advantage of the unique ability of FCS to extract the vertical component of fluid velocity. Figures 7 and S15 show the corresponding flow measurements caused by the density gradients in the FCS microscope with different electrode polarity configurations. The flow directions in Figures 7 and S15 are inferred from the PIV measurements in Figure 6 (and visualized by movies as shown in the Supporting Information). The recovered horizontal flow speeds near the surfaces are ∼5−10 μm/s, which is in good agreement with the PIV experimental results. In the case of vertical flow, flow velocities of ∼10 μm/s are obtained by FCS curve fitting. We verified that there is no horizontal flow

component for electrochemically generated density gradients directly above the active electrodes

(Figure S16). However, with such small velocities, the RSDs are comparable to the average

value, and quantifying convective forces require more in depth study, which we are currently

undertaking.
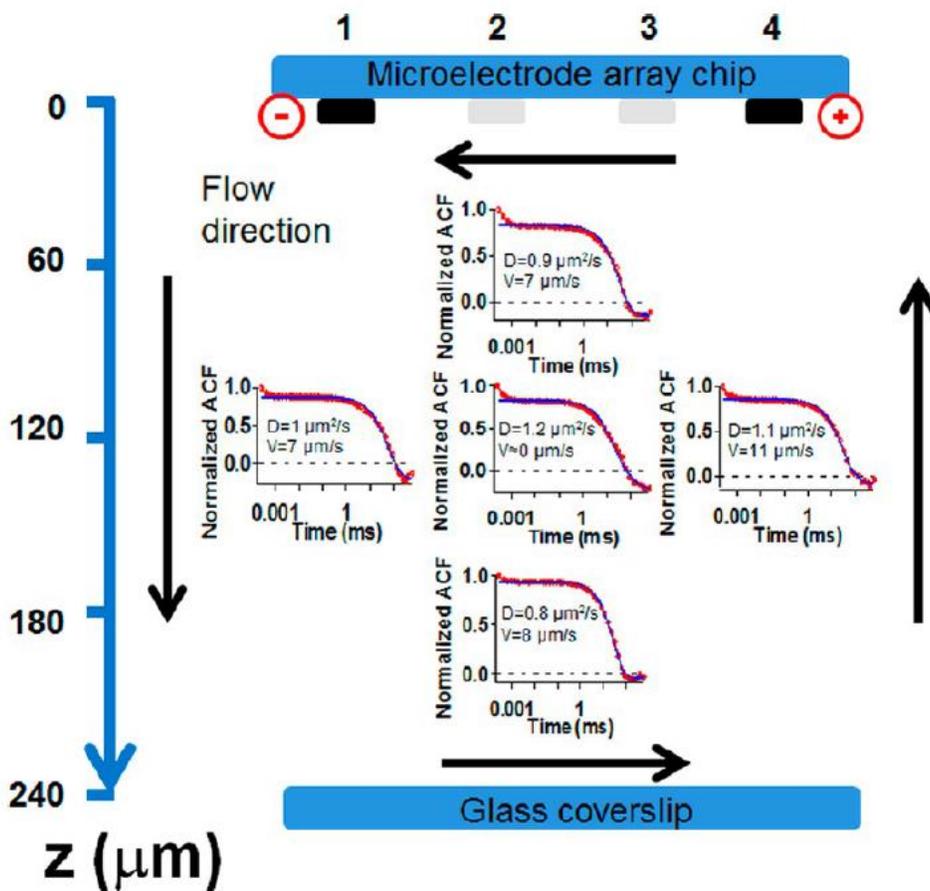
Figure 7. FCS curves showing 3D density gradient flow between the active electrodes 1 and 4 acquired with current but no magnet. The arrangements of the five FCS curves represent where the FCS curves were collected. The flow direction is inferred from the right-hand rule and measured using PIV as shown in Figure 6.

The recovered flow speeds for the center of the flow cell by FCS is ~0 μm/s, indicating

that the solution is not moving (or is moving slower than ~5 μm/s) at this point. This

experimental result, together with the horizontal flow speeds measured near the surfaces (by both

PIV and FCS), strongly suggests convection in the microfluidic cell caused by density gradients, even in such confined geometries and small electrode sizes as used here. Because the density gradient flow depends affect the flow velocity close to the surface and above the active electrodes. As shown in Figures 7 and S15, the flow velocities caused by density gradients are relatively small compared to the redox-MHD flow, although it certainly is not negligible over the active electrodes. However, it appears to not perturb flow in the center of the cell. Convective forces close to the electrode and coverslip may be one source of the asymmetric flow profile in the Z axis (Figure 3), but more work is needed to evaluate this possibility, and we have shown that FCS is a powerful tool for such a study.

3.5. Conclusions

Redox-MHD microfluidics can be easily programmed toward different flow geometries using electronics rather than prespecified microfabrication parameters. Consequently, it is anticipated that devices based on this phenomenon should be much easier to fabricate and miniaturize for lab-on-a-chip applications. For their maximum potential to be realized, the various forces involved must be thoroughly characterized and understood in all three dimensions. We have shown that FCS can be used to obtain quantitative and accurate 3D flow maps with 5−50 μm/s velocities and with up to 2 μm spatial resolution to accurately quantify flow profiles in strongly confined geometries. The combination of FCS and video microscopy with PIV/PTV analysis offers us the combined advantages of three-dimensional and three-component velocity imaging, high spatial resolution, and wide-field imaging in real time. We have uncovered interesting 3D flow profiles underlying both redox-MHD and convection caused by electrochemically generated density gradients in confined geometries. We are confident that this type of analysis will lead to improvements in designing and optimizing redox-MHD devices for a

wide range of analytical and biological applications and include manipulating fluids for multistep assays, controlling solution mixing, and playing a role in biological, pharmaceutical, and chemical separations, all with small sample volumes and less waste.

3.6 Supporting information

Experimental details, effects of time on measured current under constant voltage, separation between active electrodes on flow velocity, and electrode polarity of flow profiles, typical FCS curves, characterization of parameter error dependency on measurement time, PTV data showing negligible bead movement due to electrophoresis, errors in flow maps from FCS fitting, temporal fluctuations in flow velocities, and effect of electrode polarity on convection.

3.7 Acknowledgments

3.8 References

[1] C. Fredrickson, Z. Fan, Macro-to-Micro Interfaces For Microfluidic Devices, Lab on a Chip, 4 (2004) 526-533.

[2] X. Wang, C. Cheng, S. Wang, S. Liu, Electroosmotic Pumps and Their Applications in Microfluidic Systems, Microfluid. Nanofluid., 6 (2009) 145-162.

[3] N. Lebovka, O. Alexeev, Electroosmotic Flow in Micro- and Nanosized Systems, in: S.V. M. (Ed.) Nanoscience: Colloidal and Interfacial Aspects, CRC Press, Boca Raton FL, 2012, pp. 129-164.

[4] S.Z. Qian, H.H. Bau, Magneto-hydrodynamics based microfluidics, Mechanics Research Communications, 36 (2009) 10-21.

[5] M.C. Weston, M.D. Gerner, I. Fritsch, Magnetic Fields for Fluid Motion, Analytical Chemistry, 82 (2010) 3411-3418.

[6] N. Leventis, X. Gao, Magnetohydrodynamic Electrochemistry in the Field of Nd-Fe-B Magnets. Theory, Experiment, and Application in Self-Powered Flow Delivery Systems, Analytical Chemistry, 73 (2001) 3981-3992.

[7] J. Lee, S. Ragsdale, X. Gao, H. White, Magnetic Field Control of the Potential Distribution and Current at Microdisk Electrodes, Journal of Electroanalytical Chemistry, 422 (1997) 169-177.

[8] F. Leventis, M. Chen, X. Gao, M. Canalas, P. Zhang, Electrochemistry With Stationary Disk and Ring-disk Millielectrodes in Magnetic Fields, Journal of Physical Chemistry B, 102 (1998) 3512-3522.

[9] E.C. Anderson, M.C. Weston, I. Fritsch, Investigations of Redox Magnetohydrodynamic Fluid Flow at Microelectrode Arrays Using Microbeads, Analytical Chemistry, 82 (2010) 2643-2651.

[10] Z.P. Aguilar, P. Arumugam, I. Fritsch, Study of Magnetohydrodynamic Driven Flow Through LTCC Channel with Self-Contained Electrodes, Journal of Electroanalytical Chemistry, 591 (2006) 201-209.

[11] P.U. Arumugam, E.S. Fakunle, E.C. Anderson, S.R. Evans, K.G. King, Z.P. Aguilar, C.S. Carter, I. Fritsch, Characterization and Pumping - Redox Magnetohydrodynamics in a Microfluidic Channel, Journal of the Electrochemical Society, 153 (2006) E185-E194.

[12] S. Qian, H. Bau, Magnetohydrodynamic Flow of RedOx Electrolyte, Physics of Fluids, 17 (2005).

[13] M.C. Weston, I. Fritsch, Manipulating Fluid Flow on a Chip Through Controlled-Current Redox Magnetohydrodynamics, Sensors and Actuators B-Chemical, 173 (2012) 935-944.

[14] S.J. Lee, S. Kim, Advanced Particle-Based Velocimetry Techniques for Microscale Flows, Microfluidics and Nanofluidics, 6 (2009) 577-588.

[15] R. Lindken, M. Rossi, S. Grosse, J. Westerweel, Micro-Particle Image Velocimetry (mu PIV): Recent Developments, Applications, and Guidelines, Lab on a Chip, 9 (2009) 2551-2567.

[16] C. Meinhart, S. Wereley, J. Santiago, PIV Measurements of a Microchannel Flow, Experiments in Fluids, 27 (1999) 414-419.

[17] C. Cierpka, C.J. Kaehler, Particle imaging techniques for volumetric three-component (3D3C) velocity measurements in microfluidics, Journal of Visualization, 15 (2012) 1-31.

[18] J. Koenig, S. Muehlenhoff, K. Eckert, L. Buettner, S. Odenbach, J. Czarske, Velocity Measurements Inside the Concentration Boundary Layer During Copper-Magneto-Electrolysis Using a Novel Laser Doppler Profile Sensor, Electrochimica Acta, 56 (2011) 6150-6156.

[19] K. Tschulik, J.A. Koza, M. Uhlemann, A. Gebert, L. Schultz, Effects of Well-Defined Magnetic Field Gradients on the Electrodeposition of Copper and Bismuth, Electrochemistry Communications, 11 (2009) 2241-2244.

[20] M.C. Weston, C.K. Nash, I. Fritsch, Redox-Magnetohydrodynamic Microfluidics Without Channels and Compatible with Electrochemical Detection Under Immunoassay Conditions, Analytical Chemistry, 82 (2010) 7068-7072.

[21] C. Cierpka, T. Weier, G. Gerbeth, M. Uhlemann, K. Eckert, Copper Deposition and Dissolution in Seemingly Parallel Electric and Magnetic Fields: Lorentz Force Distributions and Flow Configurations, Journal of Solid State Electrochemistry, 11 (2007) 687-701.

[22] C. Cierpka, R. Segura, R. Hain, C.J. Kaehler, A simple Single Camera 3C3D Velocity Measurement Technique Without Errors Due to Depth of Correlation and Spatial Averaging for Microfluidics, Measurement Science & Technology, 21 (2010).

[23] P.G. Scrape, M.D. Gerner, M.C. Weston, I. Fritsch, Redox-Magnetohydrodynamics for Microfluidic Control: Remote from Active Electrodes and Their Diffusion Layers, Journal of The Electrochemical Society, 160 (2013) H338-H343.

[24] D. Magde, E. Elson, W. Webb, Fluorescence Correlation Spectroscopy .2. Experimental Realization, Biopolymers, 13 (1974) 29-61.

[25] E. Elson, D. Magde, Fluorescence Correlation Spectroscopy .1. Conceptual Basis and Theory, Biopolymers, 13 (1974) 1-27.

[26] D. Magde, W. Webb, E. Elson, Fluorescence Correlation Spectroscopy .3. Uniform Translation and Laminar-Flow, Biopolymers, 17 (1978) 361-376.

[27] M. Gosch, H. Blom, J. Holm, T. Heino, R. Rigler, Hydrodynamic Flow profiling in Microchannel Structures by Single Molecule Fluorescence Correlation Spectroscopy, Analytical Chemistry, 72 (2000) 3260-3265.

[28] X. Pan, H. Yu, X. Shi, V. Korzh, T. Wohland, Characterization of Flow Direction in Microchannels and Zebrafish Blood Vessels by Scanning Fluorescence Correlation Spectroscopy, Journal of Biomedical Optics, 12 (2007).

[29] X. Pan, X. Shi, V. Korzh, H. Yu, T. Wohland, Line scan Fluorescence Correlation Spectroscopy for Three-Dimensional Microfluidic Flow Velocity Measurements, Journal of Biomedical Optics, 14 (2009).

[30] T.J. Arbour, J. Enderlein, Application of Dual-Focus Fluorescence Correlation Spectroscopy to Microfluidic Flow-Velocity Measurement, Lab on a Chip, 10 (2010) 1286-1292.

[31] Y. Tian, M.M. Martinez, D. Pappas, Fluorescence Correlation Spectroscopy: A Review of Biochemical and Microfluidic Applications, Applied Spectroscopy, 65 (2011) 115A-124A.

[32] K. Kuricheti, V. Buschmann, K. Weston, Application of Fluorescence Correlation Spectroscopy for Velocity Imaging in Microfluidic Devices, Applied Spectroscopy, 58 (2004) 1180-1186.

[33] S. Carlotto, I. Fortunati, C. Ferrante, P. Schwille, A. Polimeno, Time Correlated Fluorescence Characterization of an Asymmetrically Focused Flow in a Microfluidic Device, Microfluidics and Nanofluidics, 10 (2011) 551-561.

[34] E. Haustein, P. Schwille, Fluorescence Correlation Spectroscopy: Novel Variations of an Established Technique, Annual Review of Biophysics and biomolecular Structure, Annual Reviews, Palo Alto, CA, 2007, pp. 151-169.

[35] P.R. Nicovich, R.M. Dickson, Three-dimensional Flow Mapping in Microfluidic Channels with Widefield Cross-correlation Microscopy, Israel Journal of Chemistry, 49 (2009) 293-301.

[36] P. Brister, K. Kuricheti, V. Buschmann, K. Weston, Fluorescence Correlation Dpectroscopy for Flow Rate Imaging and Monitoring - Optimization, Limitations and Artifacts, Lab on a Chip, 5 (2005) 785-791.

[37] N. Durisic, A.G. Godin, D. Walters, P. Grutter, P.W. Wiseman, C.D. Heyes, Probing the "Dark" Fraction of Core-Shell Quantum Dots by Ensemble and Single Particle pH-Dependent Spectroscopy, ACS Nano, 5 (2011) 9062-9073.

[38] M.C. Weston, C.K. Nash, J.J. Homesley, I. Fritsch, Maximizing Flow Velocities in Redox-Magnetohydrodynamic Microfluidics Using the Transient Faradaic Current, Analytical Chemistry, 84 (2012) 9402-9409.

[39] A. Tcherniak, C. Reznik, S. Link, C.F. Landes, Fluorescence Correlation Spectroscopy: Criteria for Analysis in Complex Systems, Analytical Chemistry, 81 (2009) 746-754.

3.S. Supporting Information for 3D Imaging of Flow Patterns in an Internally-Pumped Microfluidic Device: Redox Magnetohydrodynamics and Electrochemically-Generated Density Gradients

3.S1. Experimental Details

3.S1.1. Chemicals and Materials.

All chemicals were reagent grade and used as received. Aqueous solutions were prepared with high purity deionized water from Ricca Chemical Co. (Arlington, TX), resistivity 18 MΩ-cm. Potassium ferricyanide ($K_3Fe(CN)_6$) was obtained from EM Science (Gibbstown, NJ) and potassium ferrocyanide trihydrate ($K_4Fe(CN)_6 \cdot 3H_2O$) was from J.T. Baker (Phillipsburg, NJ). The 6 μm polystyrene latex microspheres (sulfonated, 2.5 wt% dispersion in water) were obtained from Alfa Aesar (Ward Hill, MA). The 1 μm and 0.1 μm fluorescent polystyrene latex microspheres (carboxylated, 2% dispersion in water) were obtained from Invitrogen (Eugene, OR). Electrical connection of the potentiostat to on-chip contact pads was made using an edge connector (solder contact, 20/40 position, 0.05 in. pitch) from Sullins Electronics Corp. (San Marcos, CA). The gasket for creating adhering the coverslip to the electrode chip and forming the side-walls to contain the solution within the cell was made of two layers of scotch permanent double-sided tape from 3M (St. Paul, MN). Loctite Super Glue Gel (Henkel Consumer Adhesives Inc., Düsseldorf, Germany) was used to create a permanent seal between the tape and the 25 mm × 40 mm No. 1 glass coverslip from VWR (Radnor, PA).

3.S1.2. Microelectrode Array Design and Fabrication.

The microelectrode array chips were microfabricated using the procedure reported previously.[1] The 1 in. × 1 in. silicon dioxide-coated silicon chip has 16, 40 μm × 2 mm gold microband electrodes with 60 μm gaps separating them, which are individually addressable through contact pads at the edge of the device. A photolithographically-patterned

77

benzocyclobutene layer over the gold electrodes, leads and contact pads defines the lengths of the electrodes and insulates the leads.

3.S1.3. Magnet.

The magnet used for all studies was a cylindrical NdFeB magnet, 0.75 in. high $\times$ 1 in. diameter (Amazing Magnets, Irvine, CA). The north pole faced the electrochemical cell. The magnetic field of 0.501 T was measured at the surface of the north pole using a dc magnetometer (AlfaLab Inc.).

3.S1.4 Experimental Setup.

For the FCS studies a three-sided gasket made of two layers of double sided tape with an opening of approximately 0.25 in. $\times$ 0.63 in. was attached to the electrode chip's surface with the array in the center and the open end on the 0.63 in. side facing away from the edge connector. A thin layer of super glue (Loctite) was placed on the gasket (the glue does not touch the electrode-containing chip) and allowed to dry for 1-2 min. A coverslip was placed on the glue and pressed together against the rest of the device until set. The glue prevents solution from leaking out and prevents air bubbles from getting in between the coverslip and the tape. The electrochemical cell was positioned onto the microscope stage above the microscope objective with a simple home-made stage adapter molded to the shape of the cell to enable the cell plane to be positioned perpendicular to the optical axis, with the cover slip as the lower surface and the electrode chip as the upper surface. The electrode chip surface is considered to be the $Z = 0$ plane for experiments, and the thickness of the microfluidic cells were approximately $180 - 250$ μm thick, depending on the pressure applied during the curing of the glue. The short axis of the microelectrodes is considered to be the X-axis and the long axis of the microelectrodes is

78

considered the Y-axis. For studies involving MHD, a magnet rested on the backside of the microelectrode chip as shown in Figure S1.
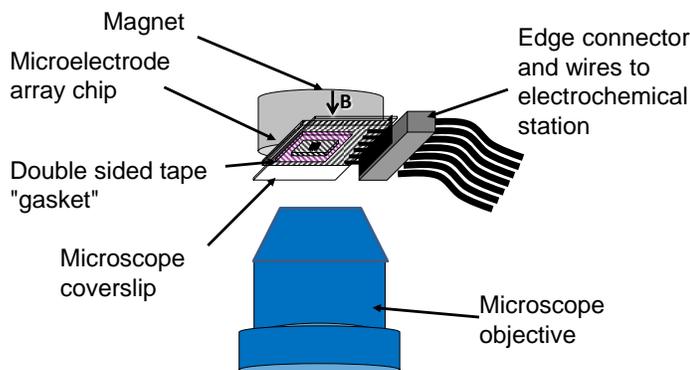
Figure S1 - Schematic of the electrochemical cell placed on an inverted confocal microscope to measure FCS.

The FCS experiments were carried out with a MicroTime 200 fluorescence microscope (Picoquant GmbH, Berlin, Germany), which is based on an Olympus IX71.[2] It uses a 485 nm pulsed laser (PDL 485, Picoquant) at a 20 MHz repetition rate to excite the fluorescent beads using a dichroic mirror (Z488/633rpc, Chroma) to send the beam through a water immersion objective (Olympus, Apochromat 60x, NA 1.3) to achieve a diffraction-limited laser focus. The laser power was ~0.5 µw. In principle, it is not necessary to use a pulsed laser; one can simply use a continuous-wave laser for FCS. However, using a pulsed laser allows one to correct the FCS curve for afterpulsing of the detector using a fluorescence lifetime filter for more accurate fitting.[3] The fluorescence is collected by the same objective and passed through the dichroic mirror and a 100 µm diameter pinhole. A fluorescence filter (520/35, Chroma) is placed in front of Single Photon Avalanche Diode Detector (SPAD, MPI, Microphotonic devices, Bolano, Italy) to reject background fluorescence and scattered laser light. The objective is positioned on a sub-nanometer precision 3D piezo scanning stage (PI, Berlin, Germany).

For optical video microscopy of the beads, the electrochemical cell was oriented differently to account for the upright geometry of the video microscope (see below for experimental details on video microscopy). The device was placed on top of the magnet and below the microscope objective with the coverslip on the topside (i.e. an inverted version of Figure S1). The construction of the cell was otherwise similar to that for the FCS studies, except the glue was omitted because the solution did not leak out with the upright orientation and the shorter duration of the experiments.

The redox solution used in all experiments contained 0.2 M $K_3Fe(CN)_6$ and 0.2 M $K_4Fe(CN)_6$. This solution was inserted through the open end of the gasket to complete the electrochemical cell. For FCS studies, the suspension of microbeads was pipetted into the redox solution to achieve a 10× dilution (from 2% to 0.2 wt % dispersion) and thereby diluted each form of the redox couple to 0.18 M. For bead video microscopy experiments, the suspension of microbeads was pipetted into the redox solution to achieve a 20× dilution (from 2% to 0.1 wt % dispersion) but the diluted concentration of each form of the redox couple was also 0.18 M.

3.S1.5 Electrochemical Control.

A CHI 650A potentiostat (CH Instruments, Austin, TX) was used for chronoamperometry (CA) in a two-electrode configuration. The working electrode was the 40×2000 μm electrode farthest away from the edge connector and labeled "1" in the figures. The combined counter/quasi-reference electrode was a parallel 40×2000 μm electrode spaced 260 μm from the working electrode and labeled "4" in the figures, with two, inactive 40×2000 μm electrodes in between it and the working electrode. A potential step of +0.4 V (electrode 1 is the anode) or -0.4 V (electrode 1 is the cathode) was applied between the working and the combined

counter/quasi-reference electrodes and the current was monitored as a function of time. The sign convention for the electronic current that is used here is as follows: positive electronic current corresponds to cathodic processes at electrode 1 and negative electronic current corresponds to anodic processes at electrode 1. (The opposite processes take place at electrode 4.) Positive ionic current in solution, however, is in the direction of net positive ion motion (away from the anode and toward the cathode).

3.S1.6. FCS Analysis.

The MicroTime 200 microscope and data collection is controlled by the SymPhoTime software (Picoquant). The 3D high resolution flow speeds map is made by taking multi-point fluorescence intensity traces in the X-Y plane at various Z positions/layers. Multi-point FCS experiments for each Z position started 20 s after the potential had been applied to the electrodes to ensure equilibration (i.e. the electronic current was outside of the transient region of the faradaic response and essentially at pseudo-steadystate), and photon trajectories were recorded for 20 s or 30 s each. After a set of traces in the X-Y plane were acquired, the Z position was moved by 30 µm and the current was reversed (by reversing the polarity of the active electrodes) to minimize extensive depletion of redox species due to the electrochemical reaction, and therefore prevent a net compositional change. After collecting multi-point FCS data on 5 or 6 Z layers that we called as one Z-stack experiment, the scanning stage will be moved along X-axis for collecting multi-point FCS data on the consecutive Z-stack imaging area, for achieving a total imagine area of ~400 µm × 80 µm × 200 µm in X, Y, and Z. A user macro was written in SymPhoTime to calculate and extract the FCS curve from each trace. Home-made software was written in Igor Pro (WaveMetrics, Inc, Oregon) to import each extracted FCS trace sequentially, and fit each with a combined diffusion and flow model[4] (equation S1).

$$G(\tau) = G(0) \cdot \frac{1}{\left(1 + \dfrac{\tau}{\tau_D}\right)\left(\left(1 + \left(a^{-2}\right)\dfrac{\tau}{\tau_D}\right)^{1/2}\right)} \cdot \exp\left\{-\left(\frac{\left(v_x^2 + v_y^2\right)\tau^2}{r_0^2}\right) \cdot \frac{1}{1 + \dfrac{\tau}{\tau_D}}\right\} \cdot$$

$$\exp\left\{-\left(\frac{\left(v_z^2\right)\tau^2}{z_0^2}\right) \cdot \frac{1}{1 + \left(a^{-2}\right)\dfrac{\tau}{\tau_D}}\right\} + G(\infty)$$

(S1)

where τ represents the correlation lag time, τ_D represents the bead diffusion time in the confocal laser focus, and v_x, v_y and v_z represent the flow speeds through the laser focus in the X, Y and Z axis. $a = z_0/r_0$ and is the elongation of the detection volume in the Z-axis relative to the X-Y axes, and is used to describe 3D diffusion. r_0 is the Gaussian laser focus waist in the X or Y axis, and z_0 is the Gaussian laser focus waist in the Z axis. G(0) is the amplitude of the autocorrelation function at $\tau = 0$, which is proportional to 1/<N> (<N> is the average number of beads in the laser focus), and G(∞) is the amplitude of the correlation function for the longest τ (chosen so that G(∞) is usually 0). For display purposes, all FCS curves are normalized to 1 at $\tau = 0$. From the fitted value of t $_D$, the diffusion coefficient is extracted using the Stokes-Einstein relation $D = \frac{r_0^2}{4\tau_D}$, and the flow speed υ is directly obtained from the fitting.

It has been shown that the flow velocity is proportional to the applied current.[5] Although we only take FCS measurements once the current has settled (after ~20 s of applying the voltage), there is still a slow but steady decrease in the current during the FCS data acquisition time in a single Z-plane (from 20 s to 200 s). In order to account for this small decrease over time, the recovered flow velocities are normalized to the same current across each imaging point in the sample. The exact current is recorded for each FCS imaging pixel, and the

recovered velocities are normalized to 20 µA in all PIV and FCS analyses for data consistency and comparison.

In our microelectrochemical cell, we observed that both 0.1 µm beads and 1 µm beads rise over time in the redox solution, although 0.1 µm beads rise much more slowly (we were able to image for 1-2 h before noticing a significant drop in the concentration, thus the rising speed caused by buoyancy is estimated to be less than 0.03 µm/s for both 0.1 µm and 1 µm beads. Hence the rising beads will not affect our redox-MHD flow speeds measurements on the order of 5-50 µm/s). The experimental time for a single X-Y plane layer to be imaged in an FCS experiment is ~400-550 s depending on the trace length and the total experimental time is 3-6 hours, also depending on the experimental parameters (FCS point acquisition time and spatial resolution). To ensure that the same level of statistics is acquired at each point, the redox/bead solution in the microfluidic cell was replaced with a fresh one every 1-2 h when needed.

3.S1.7. Video Microscopy of Bead Movement and PTV and PIV Analysis.

The bead movement was observed with a Nikon Eclipse ME600P microscope equipped with a CF plan 10×/0.30 objective, and videos were recorded using a Sony Handycam digital camera (model no. HDR-XR500V, 30 frames/s with 720×480 pixels/frame). The microscope was focused halfway between the microelectrode chip and coverslip (~ 150 µm from the chip) and the viewing region was centered halfway between the active electrodes. For PIV analysis, every tenth frame recorded over a 5-s video segment was extracted as a still image and loaded into DynamicStudio v.3.00 software (Dantec Dynamics, Copenhagen, Denmark). A series of PIV analyses was applied to each group of frames, consisting of: (1) subtracting the "Image Mean" from the group; (2) interpolating the remainder into "(N-1) Double Frames"; and (3) using the

"Average Correlation" calculation for each "double frame" pair. From this 2D velocity map (which represents the velocities at the center of the channel in the Z axis), an average velocity is determined by averaging the individual velocities at the center of the channel, half way between the active electrodes (1 and 4) with a 150 μm width, and averaged over 250 μm in Y (i.e. the center $3 \times 5 = 15$ velocity vectors).

Velocity results calculated in DynamicStudio were verified by PTV of individual beads using World-in-Motion v.6.0 (Physics Curriculum & Instruction, Lakeville, Minnesota). Every 10th frame from a 3.67 s segment (11 frames total) was cropped to a 560×420 pixels for compatibility. Four clearly visible beads were tracked across all 11 frames to get an average and standard deviation of 10 velocity measurements for each bead. The velocities and standard deviation for each bead were pooled together to get an overall average.

Prior studies for a similar geometry and flow pattern demonstrated that the magnitude of MHD-driven fluid flow is proportional to the current.[6] Thus, to account for variations of electrode current from chip-to-chip and from electrode cleanliness day-to-day, the bead speeds here were normalized to a 20 μA current. For example, if a pseudo-steady state current of 27 μA were measured over the period that the fluid flow was evaluated, the reported fluid speeds would be determined by multiplying the empirically-obtained speeds by a factor of 0.74 (e.g. 20 μA/27 μA).

3.S2. Supporting Results and Discussion

3.S2.1 Current vs Time at Constant Applied Voltage.

At a constant applied voltage, the current drops sharply within the first 20 s and then levels out, although it does decrease slightly during the ~550 s measurement time. The FCS experiment is started after this initial drop in current after ~20 s (Figure S2).
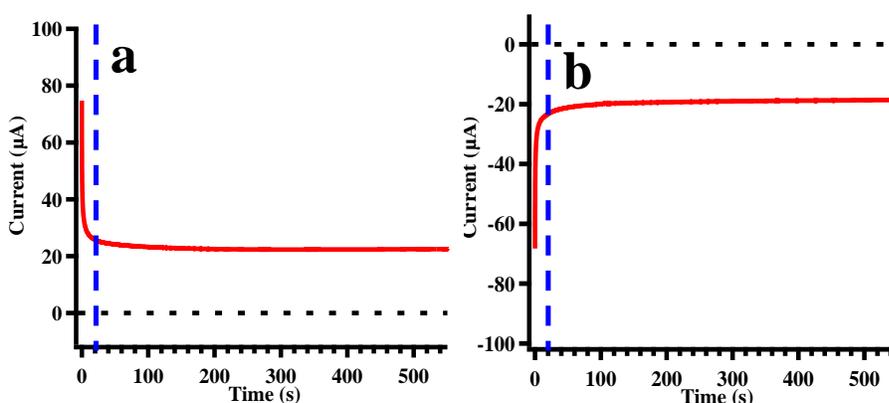
Figure S2 - Examples of chronoamperograms obtained during FCS studies of redox-MHD fluid flow, showing the dependence of positive and negative electronic current on time.

3.S2.2 Flow Velocity as a Function of Electrode Separation.

The flow velocity of redox-MHD depended on the separation between active electrodes (Figure S3). This was determined by switching on various electrodes relative to electrode 1, and measuring the velocity by PIV. The measured current at the time when speeds were analyzed for each distance are indicated by each data point. The higher current shown at the smallest distance is enhanced because of redox cycling. The experimental setup was similar to that used for the other PIV and PTV studies in the main text, except that the concentration of the redox species was 0.1 M rather than 0.2 M, and thus the measured velocity is approximately half that from 0.2

85

M concentrations used for the main experiments. This discrepancy occurred due to measuring

these data before optimizing the redox species concentration, but the trend should be unaffected;

only the absolute recovered velocities are affected. The maximum speed occurred when the

active electrodes were ~260 µm apart, which corresponds to activating electrodes 1 and 4 of the

electrode array described in Figure 1 of the main text, and therefore this separation was used for

all studies reported in the paper.
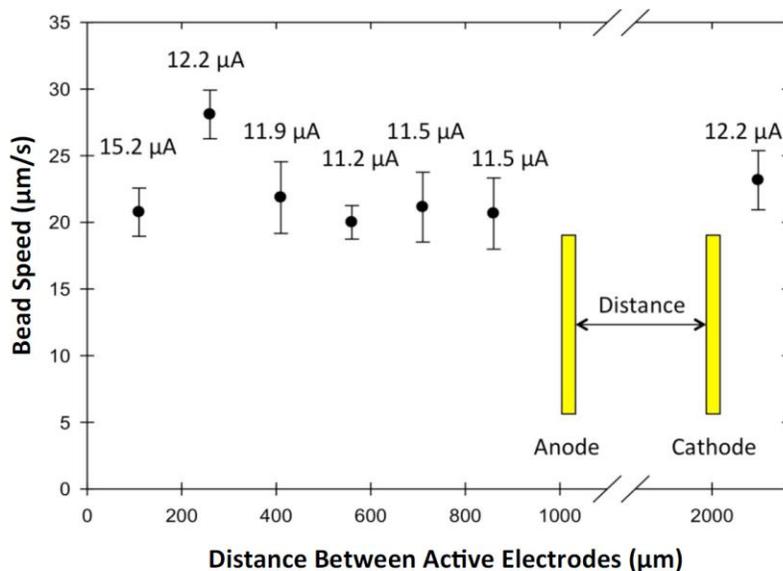
Figure S3 - Effect of separation between active electrodes (the working anode and the combined counter/quasi-reference counter cathode) on redox-MHD fluid flow, as determined by PIV analysis of the motion of 10 µm beads.

3.S2.3. Dependence of Flow Speed as a Function of Z Position with Negative and Positive

Electronic Current.

Because the FCS flow maps take a relatively long time to acquire with high resolution,

we chose to alternate the electrode polarity between each Z plane, rather than refreshing the

86

solution, to minimize depletion of redox species at the electrodes which would cause the current

magnitude to drop and velocity to decrease proportionally. Figure S4 confirms that, although

switching the voltage polarity will change the direction of the electronic current, and therefore

the direction of the ionic current and flow direction (by the right hand rule), it does not

significantly change the flow velocity (as long as the current magnitude remains unchanged),

within the error of the FCS measurements.
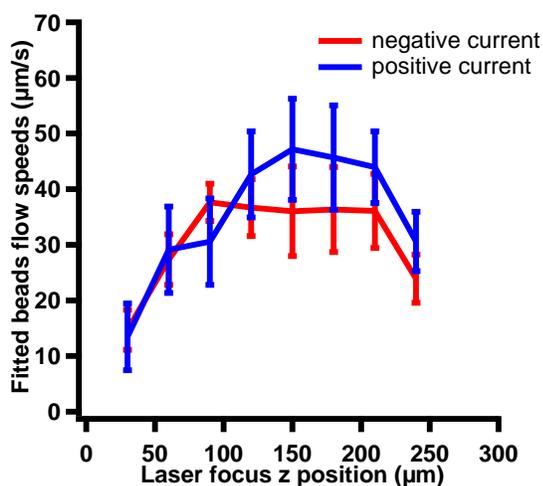
Figure S4 - Fitted flow speeds of 0.1 μm beads as a function of focal position from the chip
surface highlighting that they are independent of current polarity.

3.S2.4. Example FCS curves and fitting to equation S1 (equation 2 in the main text).
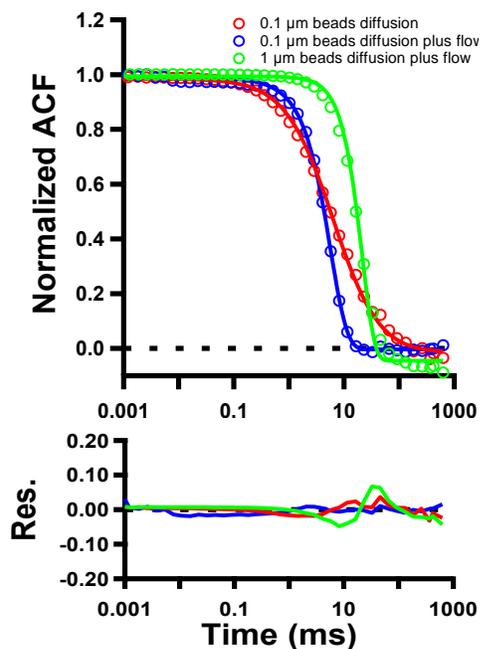
Figure S5 - Example FCS curves showing diffusion-only and diffusion-plus-flow, together with fits to equation 2 to obtain diffusion coefficients and flow speeds at a given position. The fitting residues are shown below the FCS curves.

3.S2.5. Optimizing FCS Experimental Parameters.
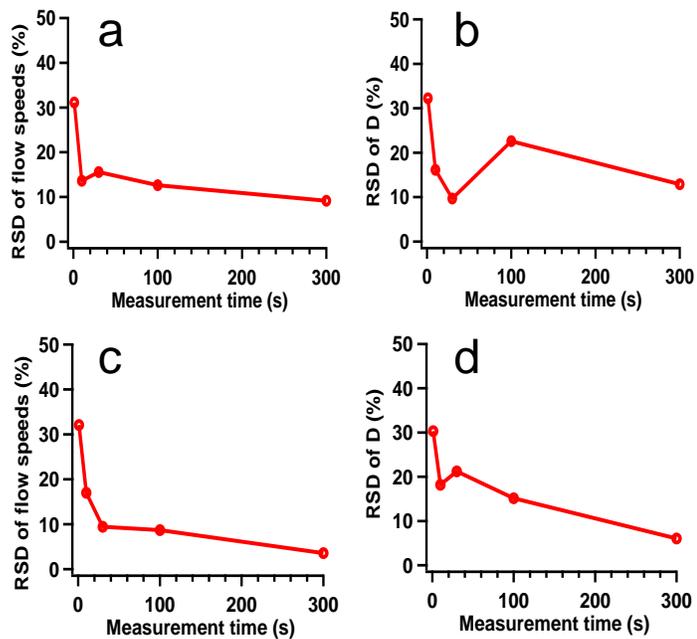
Figure S6 - Relative standard deviation of flow speeds and diffusion coefficients of 0.1 µm beads by FCS as a function of measurement time (FCS point fluorescence intensity trace length). (a) and (b) negative electronic current, (c) and (d) positive electronic current. The average flow speeds are ~45 µm/s, and the average diffusion coefficient is ~ 3 µm2/s.
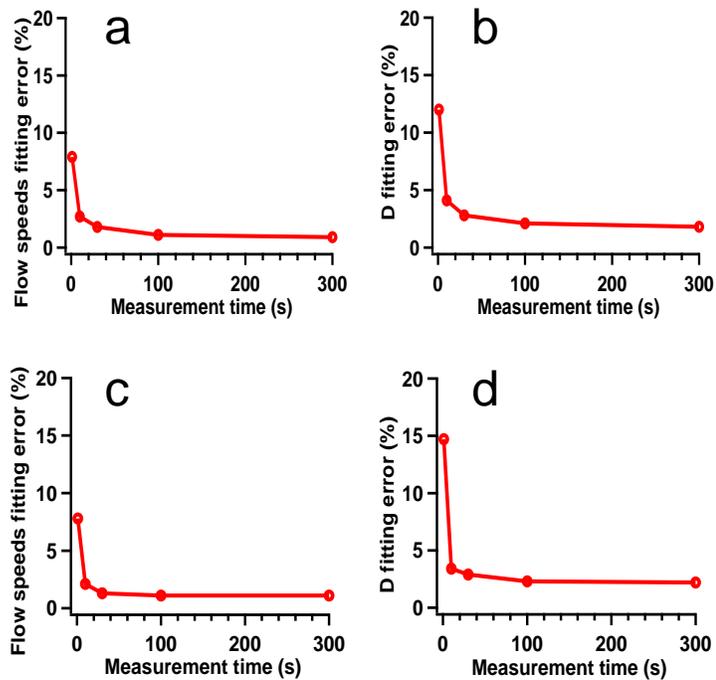
Figure S7 - fitting error of flow speeds and diffusion coefficients of 0.1 μm beads by FCS as a function of measurement time (FCS point fluorescence intensity trace length). (a) and (b) negative electronic current, (c) and (d) positive electronic current.
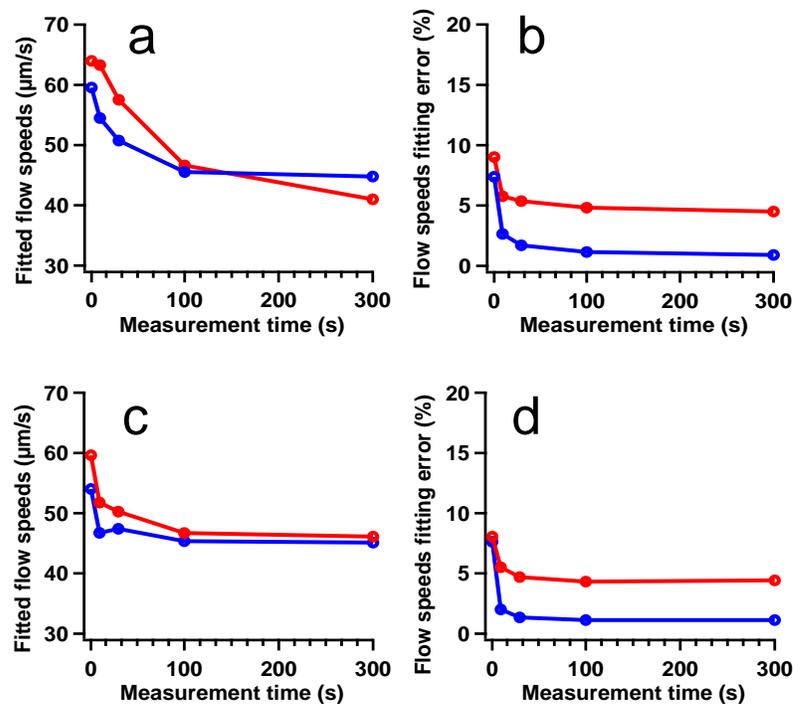
Figure S8 - Fitted flow speeds and fitting errors of 0.1 µm beads by FCS with diffusion coefficients D fixed (red curves) and flexible (blue curves) in equation S1 (equation 2 in the main text) as a function of measurement time (FCS point fluorescence intensity trace length). (a) and (b) negative electronic current, (c) and (d) positive electronic current. The flow speed values converge with shorter measurement time, and with a smaller fitting error, when allowing D to be flexible rather than fixed, due to the convolution of errors into a single parameter associated with the limited collection statistics.
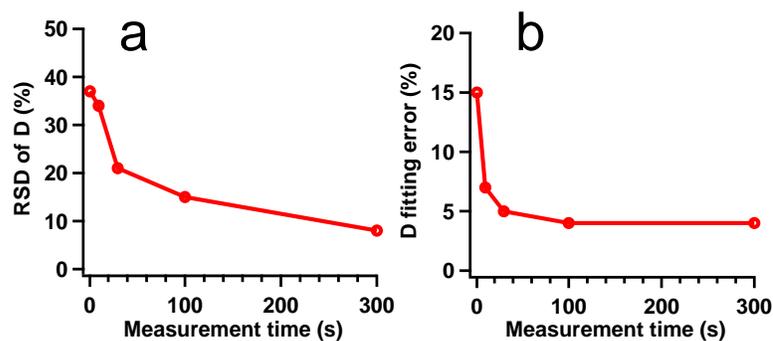
Figure S9 - Relative standard deviation (a) and fitting error (b) of the diffusion coefficient of 0.1 µm beads obtained by FCS with no applied electric or magnetic field, as a function of measurement time.
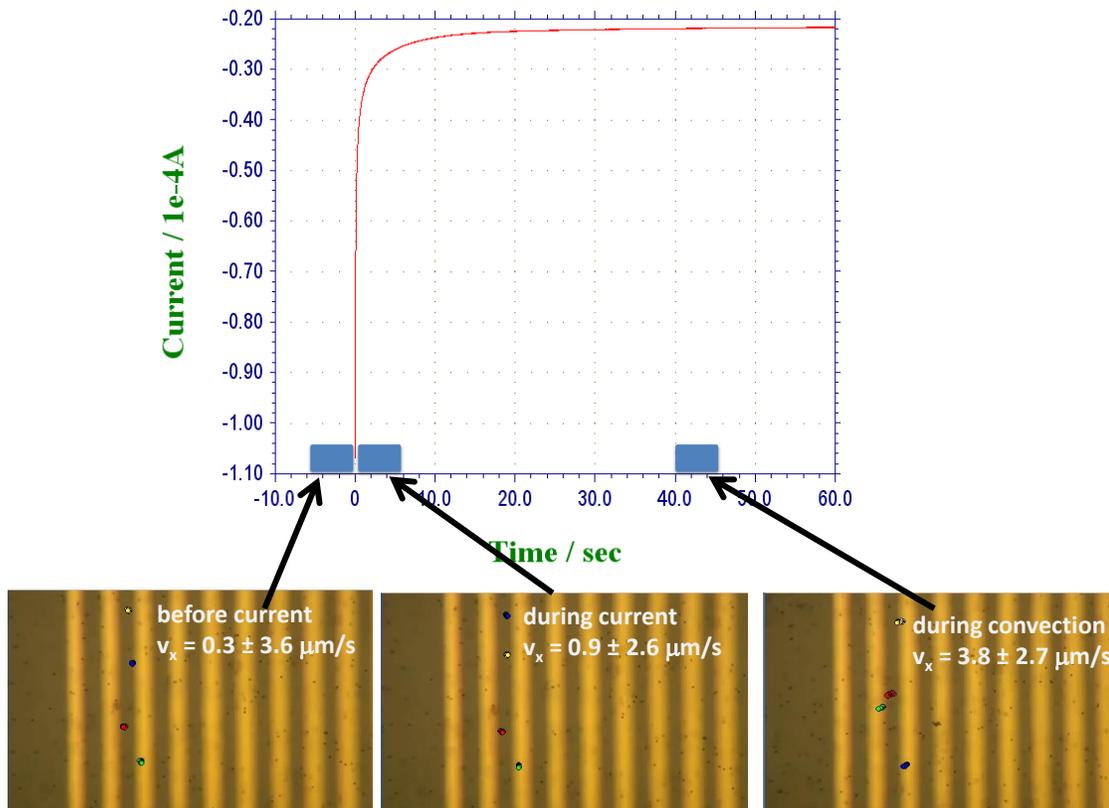
Figure S10 - PTV tracking of beads between the electrodes, parallel to the electric field (i.e. in the X-axis) of 6-µm sulfonated beads in the absence of a magnetic field for time periods before current (for the 4 s, before the potential is applied), during current (for 4 s, after the potential is applied), and during convection (for 4 s, starting at +40 s during the experiment) as indicated in the chronoamperogram. The locations of four beads in each of the micrographs (each bead is represented by a dot of a specific color) were taken during the 4 s measurement periods and visualize the displacement for each. Multiple dots of a single color for each bead superimposed on a given micrograph represent the location of the bead at 1 s time intervals. The colors assigned to the beads are arbitrary and do not reflect the same bead in different micrographs. The density gradient-induced convection had not started yet for the +4 s time window (center micrograph). The PTV data analysis reveals that the flow velocities of the four beads are ~0 µm/s in the X-direction before current and during current (within experimental error), showing that bead electrophoresis movement is negligible in our FCS and PIV experiments. The PTV data analysis also reveals that the flow velocities of the four beads during convection (density gradient-induced horizontal flow between active electrodes 1 and 4) are consistent with the PIV imaging of experimental results shown in Figure 6.

3.S2.6. Error in Flow Velocity and Diffusion Coefficient as a Function of Position from Figure 3 in the Main Text.

Each pixel contains an FCS curve similar to Figure S5, which results in a fitting error associated with flow and diffusion, which is plot as an "error map" to show how accurate we can determine each parameter in X, Y and Z, which is showin in Figure S8. Because 0.1 μm beads diffuse in the redox solution with D of ~3 μm2/s, it limits the slowest flow velocity that can be reliably measured with 0.1 μm beads. According to the average flow velocity fitting error, the slowest solution flow velocity that can be reliably measured by 0.1 μm beads is ~5 μm/s at the sides of the channel above the active electrodes.
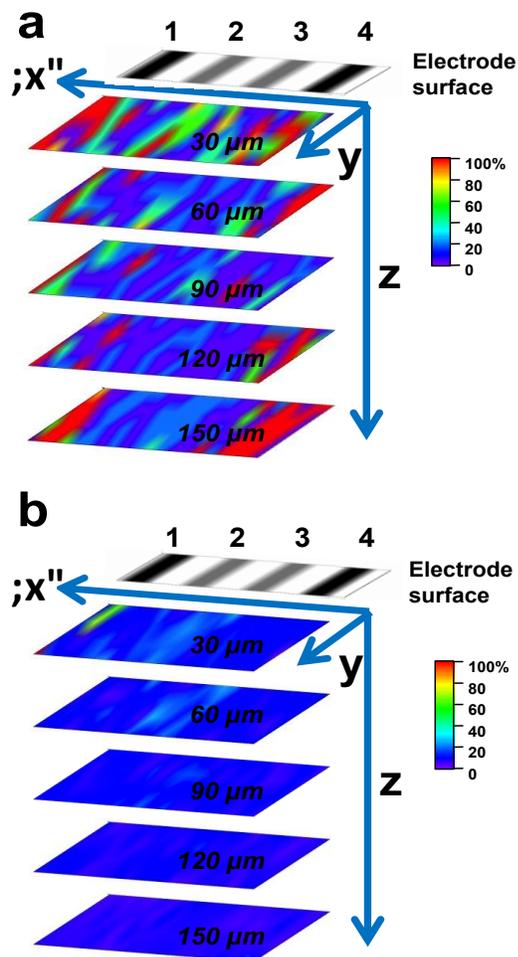
Figure S11 - Maps showing the relative standard deviations of fitted flow speeds (a) and diffusion coefficient (b) for the 0.1 µm beads shown in Figure 3.

3.S2.7. 3D Flow Velocity Map and Error as a Function of Position Obtained Using 1 µm Beads.

In contrast to 0.1 µm beads, we had anticipated that flow velocities smaller than 5 µm/s can be reliably measured with 1 µm fluorescent beads, since 1 µm beads do not diffuse, leading to fewer fitting parameters in equation 2. Figure S9 shows that the flow velocity errors associated with 1 µm beads at ~5 µm/s is just as high as for 0.1 µm beads. One challenge with 1 µm beads is that they rise much faster in the redox solution compared to 0.1 µm beads due to the lower

density of polystyrene compared to the aqueous electrolyte solution. This leads to a lower

effective concentration of beads in the solution at any given time, reducing the collection

statistics for a given measurement time (30 s). This effect also leads to the requirement for more

frequent exchanging of the beads in the electrochemical cell solution, significantly increasing the

experiment imaging times, and possibly introducing additional sources of error into the

experiment. Even with frequent changing of the solution, the fitting error was not reduced

compared to 0.1 μm beads. It appears that the errors associated with both the presence of

diffusion and varying the solution and collection statistics are similar, leading to a lower limit of

~5 μm/s for both sizes of bead.
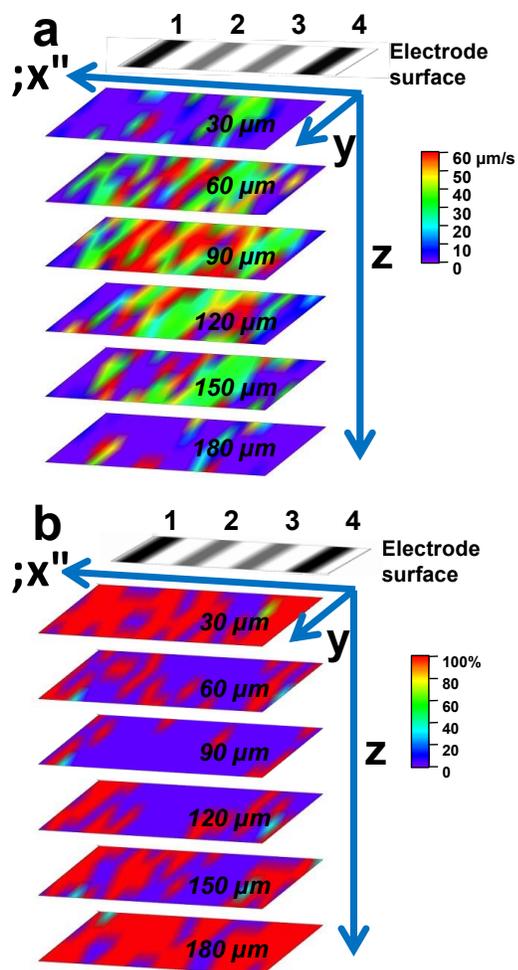
Figure S12 - (a) 3D map for fitted flow speeds obtained from 1 μm beads in redox MHD microfluidic flow cell. (b) error in flow speed recovered from each pixel obtained from fitting to equation S1.

3.S2.8. Distribution of Fitted Flow Speeds as a Function of Time at a Given Point.

Asymmetry in the distribution of fitted flow speeds at a given point as a function of time is shown in Figure S13 towards lower flow speeds highlight the complexity of redox-MHD flow. This effect may be indicative of fluctuations in the flow caused by temporal reduction in the redox reaction rates, but is still an open question.
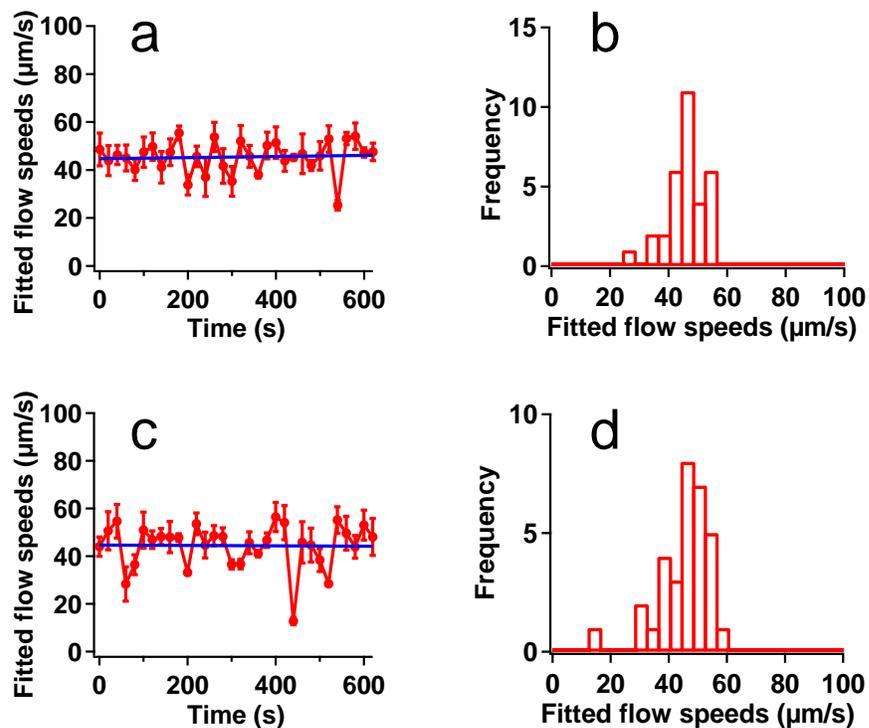
Figure S13 - (a) and (c) Fitted 0.1 µm beads redox MHD flow speeds and fitting errors vs time with positive and negative electronic current respectively, for the fixed position between electrode 2 and 3 at the central Z-plane of the cell. The blue lines highlight the average flow speeds. (b) and (d) the corresponding flow speeds histograms for (a) and (c).

3.S2.9. Diffusion Coefficient and Error at 2 µm Spatial Resolution for the 0.1 µm Beads.
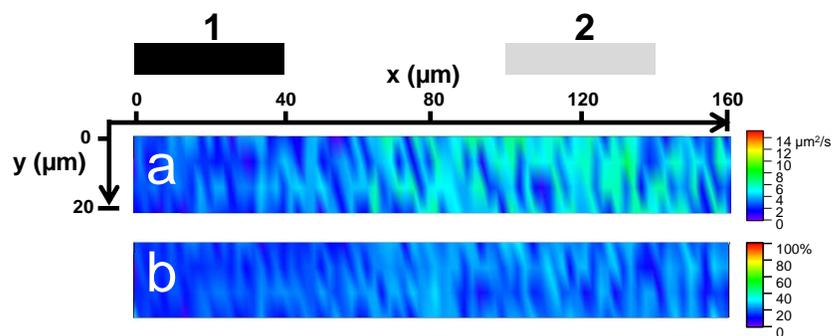
Figure S14 - maps of diffusion coefficient (a) and its fitting error (b) for Figure 4.

3.S2.10. Convection Caused by Density Gradients Using Opposite Electrode Polarity to the Main Text.

By the right hand rule, convection switches direction, as shown with PIV imaging, but the recovered velocities are negligibly affected. The vertical component of velocity measured by FCS is not possible to obtain with normal PIV imaging.
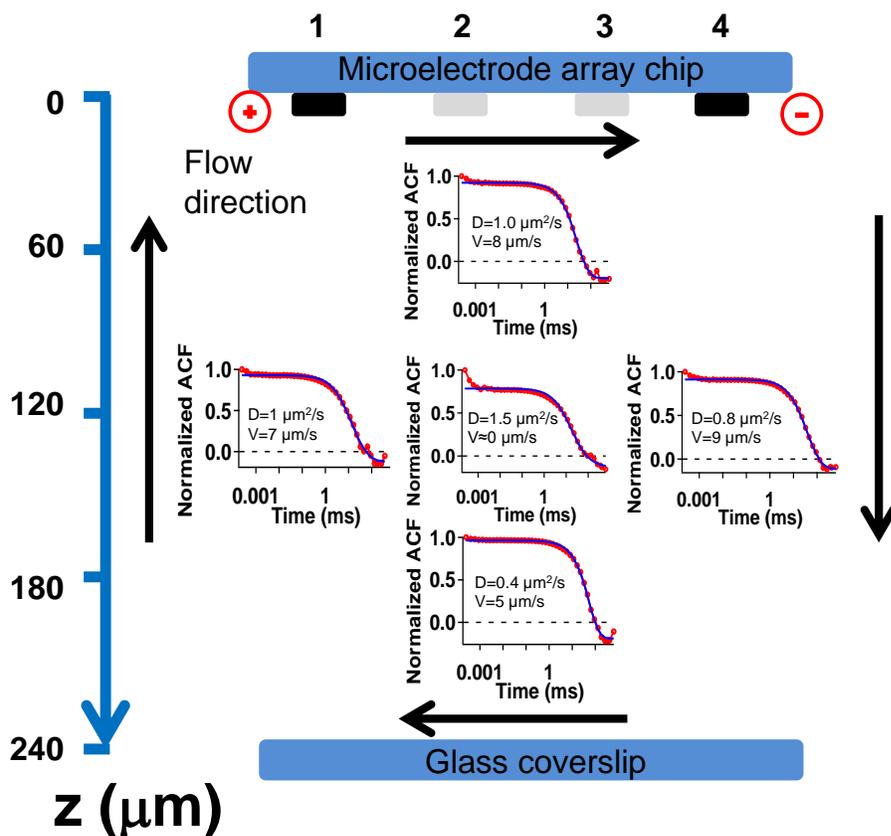
Figure S15 - FCS curves showing 3D density gradient flow between the active electrodes 1 and 4 acquired with current but no magnet. In this figure, the current polarity is opposite that of Figure 7, thus reversing the flow direction.
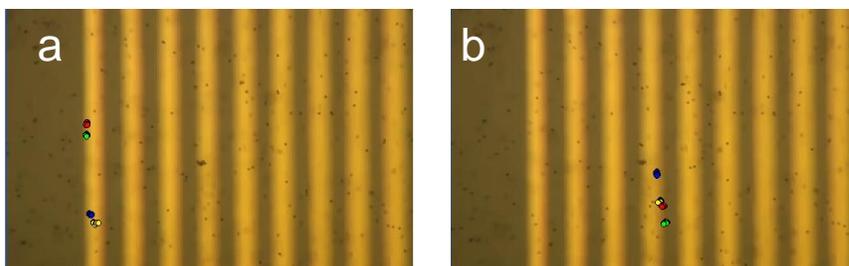
Figure S16 – Bead-tracking for determining horizontal bead movement over the active electrodes 1 and 4 (a and b) where beads are rising and falling because of the vertical density gradient-induced flow. The motion of the beads in each micrograph was followed from 40 s to 44 s and two other beads in the micrographs were followed from 44 s to 48 s. At these times during the potential step, natural convection has begun due to the density gradient. The locations of four beads in each of the micrographs (each bead is represented by a dot of a specific color) were taken during the 4 s measurement periods and visualize the displacement for each. Multiple dots of a single color for each bead superimposed on a given micrograph represent the location of the bead at 1 s time intervals. The colors assigned to the beads are arbitrary and do not reflect the same bead in the different micrographs. The four beads in (a) and (b) were tracked before they went out of focus in Z. The bead-tracking data analysis reveals that the average bead horizontal flow velocity is 1 ± 3 μm/s during the vertical density gradients induced flow, thus justifying that the simplified diffusion plus 1-D vertical flow FCS equation S1 (equation 2 in the main text) can be used to fit the vertical density gradient flow speeds (Figures 7 and S15). The experiment was performed in the absence of a magnet.

3.S3. References

[1] E.C. Anderson, M.C. Weston, I. Fritsch, Investigations of redox magnetohydrodynamic fluid flow at microelectrode arrays using microbeads, Anal. Chem., 82 (2010) 2643-2651.

[2] N. Durisic, A.G. Godin, D. Walters, P. Gruetter, P.W. Wiseman, C.D. Heyes, Probing the "Dark" Fraction of Core-Shell Quantum Dots by Ensemble and Single Particle pH-Dependent Spectroscopy, ACS Nano, 5 (2011) 9062-9073.

[3] J. Enderlein, I. Gregor, Using fluorescence lifetime for discriminating detector afterpulsing in fluorescence-correlation spectroscopy, Review of Scientific Instruments, 76 (2005) 033102.

[4] E. Haustein, P. Schwille, Fluorescence correlation spectroscopy: Novel variations of an established technique, Annual Review of Biophysics and Biomolecular Structure, Annual Reviews, Palo Alto, 2007, pp. 151-169.

[5] M.C. Weston, C.K. Nash, J.J. Homesley, I. Fritsch, Maximizing Flow Velocities in Redox-Magnetohydrodynamic Microfluidics Using the Transient Faradaic Current, Anal. Chem., 84 (2012) 9402-9409.

[6] M.C. Weston, I. Fritsch, Manipulating Fluid Flow on a Chip Through Controlled-Current Redox Magnetohydrodynamics, Sens. Actuat. B, (2012) in press.

4. Microfluidic Flow from Magnetoconvective and Gravitational Forces Using Electrochemical Deposition and Stripping of Paramagnetic Copper and Diamagnetic Lead with an Applied Current at Microband Electrodes in a Small Volume

4.1. Abstract

Magnetoconvective and gravitational forces on microfluidic flow were studied using experiments with paramagnetic copper(II) and diamagnetic lead(II) in a small volume system consisting of microband electrodes on an insulated silicon chip. Four contributions toward fluid flow were considered. The first is the magnetohydrodynamic force ($\mathbf{F_B}$), which is the magnetic component of the Lorentz force and governed by the right hand rule. The second is the gravitational force ($\mathbf{F_g}$), which causes convection under nonuniform density conditions, as by metal ions generated into or depleted from solution adjacent to the anode and cathode, respectively. The third is the magnetic gradient force ($\mathbf{F_{\nabla B}}$), and is present when there are paramagnetic species, such as Cu(II), in a nonuniform magnetic field. The fourth is the paramagnetic concentration gradient force ($\mathbf{F_{\nabla C}}$), over which there is controversy about its magnitude. It is present when a nonuniform concentration of paramagnetic species occurs, as during deposition and dissolution of copper, but not for lead. Two electrode configurations were used to investigate these forces: (1) one-band, where copper or lead was deposited on one microband electrode with counter and reference electrodes distant, and (2) two-band, where copper or lead was simultaneously deposited at one microband electrode and stripped off of another one, parallel to and near the former. Further insight is possible by comparing fluid flow during and after electrode activation, when the forces $\mathbf{F_{\nabla C}}$, $\mathbf{F_{\nabla B}}$, and $\mathbf{F_g}$ persist and $\mathbf{F_B}$ has ended.

4.2. Introduction

The uses of magnetic fields to induce magnetoconvection, provides unique possibilities for the manipulation of fluid flow on a chip [1]. Until recently, it had not been studied in small volumes confined to dimensions like those of lab-on-a-chip devices. Previous work by others to develop micropumps makes use of the magnetic portion of the Lorentz force, the magnetohydrodynamic force ($\mathbf{F_B}$), but those studies suffer from bubble formation and electrode corrosion [2]. Work in our laboratory has resolved that issue by adding redox species to the system, and is ongoing. We have shown that redox-MHD based convection can be used to pump fluids in a microchannel, [3, 4], can be useful in enhancing trace metal analysis [5-7], and can pump a fluid plug on a chip without requiring channel sidewalls [8, 9]. The movement of ions perpendicular to a magnetic field creates $\mathbf{F_B}$ as shown in eq. 1, where $\mathbf{F_B}$ is the magnetic component of the Lorentz force, $\mathbf{B}$ is the magnetic flux density, and $\mathbf{j}$ is the ionic current density, defined as the direction of movement of positive ions.

$$\mathbf{F_B} = \mathbf{j} \times \mathbf{B} \tag{1}$$

Although $\mathbf{F_B}$ has by far the largest influence on fluid movement in the previously reported magnetoconvective systems it is not the only force present. Experimental conditions that produce $\mathbf{F_B}$ can also produce the gravitational force ($\mathbf{F_g}$), the magnetic gradient force ($\mathbf{F_{\nabla B}}$), and the proposed paramagnetic concentration gradient force ($\mathbf{F_{\nabla C}}$).

This chapter focuses on metal deposition and stripping to investigate these forces. The reason for this is that switching between paramagnetic Cu^{2+} and diamagnetic Pb^{2+} changes the

magnetic susceptibility with minimal changes to the properties of the solution's ionic strength,

viscosity, and diffusion coefficients. There is also existing literature that focuses on the

magnetohydrodynamic effects on electrodeposition of metals [10-13]. However, the

magnetohydrodynamic effects are focused on large systems, not microfluidics. The very nature

of the small volume system used in this chapter and a means to follow the fluid flow while

activating different electrodes in a controlled fashion, should provide a better approach for

investigating these phenomena. Figure 1a has a diagram of the direction of the four forces

considered for copper reinforcing flow while Figure 1b shows the same thing for lead.
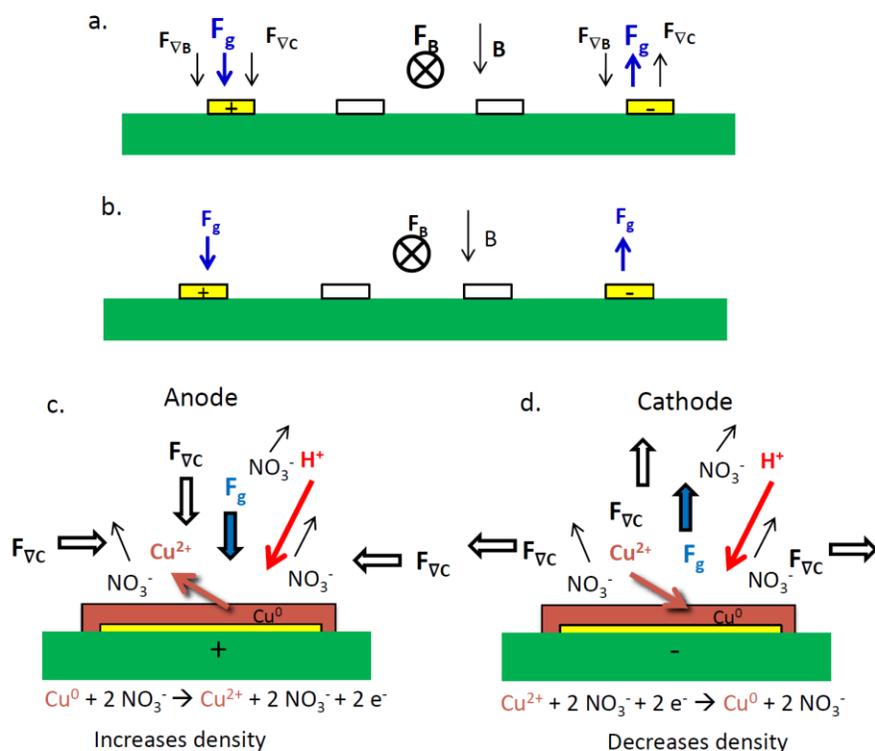
Figure 1. Diagrams showing the direction of the forces in the diffusion layer that are present
during experiments using two-band electrodes for the overall cross section view for copper (a)
and lead (b), and for the close-up view for copper at the anode (c) and at the cathode (d).

Convection caused by $\mathbf{F_g}$ during metal deposition is caused by depletion of the metal ion concentration near the electrode. The resulting charge difference will be compensated by the migration of ions in solution. Each species will compensate a fraction based on the transference numbers which were calculated using equation 2 where t_i is the transference of ion j, and μ_i and μ_j are the motilities of ions i and j. The calculated transference numbers are found in Table 1 for the solutions investigated here. For all the solutions, most of the charge is compensated by the movement of hydrogen ions, a smaller contribution is from the nitrate ions, and the smallest contribution is from the metal ions. The end result is a less dense fluid element than the surrounding solution that rises to the top of the cell. During metal stripping, the opposite phenomena occur, where higher metal ion concentration near the electrode results in a denser fluid element that sinks to the bottom of the cell. Convection caused by $\mathbf{F_g}$ has been studied using ferricyanide and ferrocyanide with a disk electrode and ring electrodes [14], as well as band electrodes (See Chapter 2). These studies have shown that the $\mathbf{F_g}$ affects the fluid adjacent to the electrode and expands to include the bulk solution well after the start of the current, in contrast to $\mathbf{F_B}$ which impacts the solution everywhere the cross product of $\mathbf{j}$ and $\mathbf{B}$ are nonzero and essentially immediately when the current starts.

$$t_j = \frac{|z_i|\mu_i C_i}{\sum_j |z_j|\mu_j C_j} \tag{2}$$

Table 1. Transference numbers for copper(II), lead(II), nitrate, and hydrogen ions in solutions containing 95.2 mM nitric acid and either 95.2 mM copper nitrate, 0.0952 M lead nitrate, 9.52 mM copper nitrate, or 9.52 mM lead nitrate. (Ion motilities used in the calculations are: 5.56×10^{-8} $m^2s^{-1}V^{-1}$ for copper [15], 4.28×10^{-8} $m^2s^{-1}V^{-1}$ for lead (calculated from diffusion coefficient [16]), 5.50×10^{-8} $m^2s^{-1}V^{-1}$ for nitrate [17], and 4.28×10^{-8} $m^2s^{-1}V^{-1}$ for hydrogen [17].

Solution	t metal	t NO_3^-	t H^+
95.2 mM copper	0.156	0.335	0.509
95.2 mM lead	0.125	0.348	0.528
9.52 mM copper	0.024	0.204	0.773
9.52 mM lead	0.018	0.205	0.777

$\mathbf{F_{\nabla B}}$ occurs when paramagnetic species interact with a non-uniform magnetic field. It can be described by equation 3 [18], where C_p is the paramagnetic species concentration, N_A is Avogadro's number, m^* is magnetic moment of the paramagnetic species, k is Boltzmann constant, and T is the temperature. The term $(\mathbf{B \cdot \nabla})\mathbf{B}$ in the equation gives $\mathbf{F_{\nabla B}}$ a complicated relationship with $\mathbf{B}$, but $\mathbf{F_{\nabla B}}$ usually points toward the higher magnetic flux density.

$$\mathbf{F_{\nabla B}} = 2C_p N_A \left[\frac{m^{*2}}{kT} \right] (\mathbf{B \cdot \nabla})\mathbf{B}$$

(3)

It has been proposed that $\mathbf{F_{\nabla C}}$ is created when a non-uniform concentration of paramagnetic species will interact with a magnetic field. A non-uniform concentration of paramagnetic can occur between the electrode and bulk solution during electrochemical experiments. The paramagnetic species are drawn toward the highest concentration [19], and $\mathbf{F_{\nabla C}}$ opposes the net diffusion. This force is defined by equation 4 [20]. Figure 1c and d shows the direction of the force at the anode and cathode. However, there is controversy in the literature over the magnitude of this force. Experimental results have been interpreted to demonstrate both its impact [19, 20], and lack of impact [21].

$$\mathbf{F}_{\nabla C} = N_A \frac{m^{*2}}{kT} |\mathbf{B}|^2 \nabla C_p$$

(4)

Each of these forces impact fluid flow in different ways and under different conditions, and thus it was hypothesized that their relative contributions could be determined. Because Cu(II) is paramagnetic and Pb(II) is diamagnetic, the forces $\mathbf{F}_{\nabla C}$ and $\mathbf{F}_{\nabla B}$ should be present only in the Cu(II) solutions in the presence of a magnetic field, where only the latter requires a nonuniform magnetic field. Further insight is possible by comparing bead movement when the current is on to movement after it is turned off when the forces $\mathbf{F}_{\nabla C}$, $\mathbf{F}_{\nabla B}$, and $\mathbf{F_g}$ persist and $\mathbf{F_B}$ has ended. $\mathbf{F_g}$ and $\mathbf{F}_{\nabla C}$ will continue until convection and diffusion create a homogenous solution. $\mathbf{F_g}$ is different from the other forces due to the fact that no magnetic field is required. When the metal concentration of the solution is lowered $\mathbf{F}_{\nabla B}$ decreases in proportion to the concentration while the other three forces decrease with the current, which during deposition is limited by the available metal ions.

Two different electrode geometries, one-band and two-band, were investigated that cause distinctly different MHD flow patterns, and therefore offset the other forces in different ways. When activating the one-band electrode as a cathode with a magnet field perpendicular to the chip, fluid rotates around the electrode due to $\mathbf{F_B}$. This geometry produces oval flow around the active electrode, simpler $\mathbf{F_g}$ based convection, and deposits the copper needed so that it can serve as the anode of the two-electrode geometry. The two co-planar band electrodes, one serving as working electrode and the other as counter electrode, provide linear flow between the working and counter due to $\mathbf{F_B}$ in the presence of the magnet [22, 23]. This geometry provides the opportunity to attain bead velocity data that are simpler and more quantitative that result from

F$_B$,, and therefore more definitive, so that its influence can be more easily separated out from the influence of the other forces, **F$_B$, F$_g$, F$_{\nabla B}$,** and **F$_{\nabla C}$**.

4.3. Experimental

4.3.1. Chemicals and Materials.

All chemicals were reagent grade and used as received. Aqueous solutions were prepared with high purity deionized water from Ricca Chemical Co. (Arlington, TX), resistivity 18 MΩ-cm. The copper(II) nitrate and lead(II) nitrate were from Sigma Aldrich (St. Louis MO). The nitric acid was acquired from VWR International (Radnor, PA). The 6 μm polystyrene latex microspheres (sulfonated, 2.5 wt% dispersion in water) were obtained from Alfa Aesar (Ward Hill, MA). The electrical connection of the potentiostat to the on-chip contact pads was made using an edge connector (solder contact, 20/40 position, 0.05 in. pitch) from Sullins Electronics Corp. (San Marcos, CA).

4.3.2. Microelectrode Array Design and Fabrication.

The microelectrode array chips were fabricated using the procedure reported previously [1]. The 2.54 cm × 2.54 cm silicon dioxide-coated silicon chip has 16 parallel, 40 μm × 2000 μm co-planar gold microband electrodes with 110 μm gaps separating them and which are individually addressable through contact pads at the edge of the device. A photolithographically-patterned benzocyclobutene layer over the gold electrodes, leads and contact pads defines the
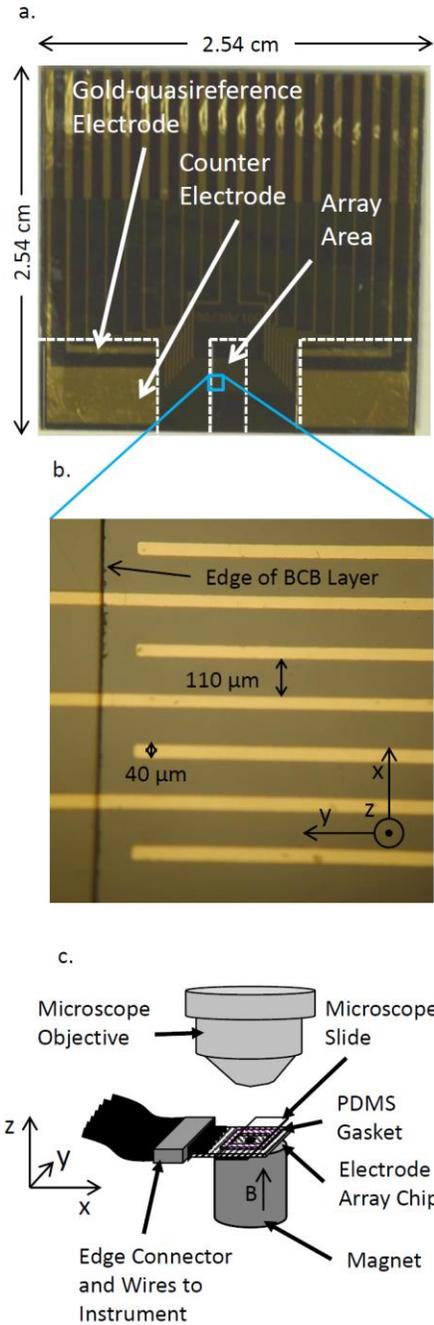
Figure 2. Electrode chip and experimental setup. a. Photograph of a chip used in the experiments. There are 16 gold microband electrodes in the array area with lengths of 2000 μm and widths of 40 μm with 110 μm gaps between them. There are two identical medium and large gold electrodes; one was used as the counter electrode and another as the quasi-reference electrode, as indicated. Dashed outlines emphasize the edge of the BCB insulating layer. b. Expanded view (microscope image) of array area. c. Diagram of the experimental setup.

lengths of the electrodes and insulates the leads. A diagram of the chip can be seen in Figure 2a. A close up view of the array area can be found in Figure 2b.

4.4.3. Magnet.

The magnet used for all studies was a cylindrical NdFeB magnet, 2.54 cm high × 2.54 cm diameter (Amazing Magnets, Irvine, CA). The north pole faced the electrochemical cell. The magnetic field of 0.501 T was measured at the surface of the north pole using a dc magnetometer (AlfaLab Inc.).

4.3.4. Experimental Setup.

An 810 µm PDMS gasket with an opening of 5.5 mm × 12.6 mm was set on top of the chip, and solution inserted to fill in the opening using a micropipette. A stock solution of 0.1 M nitric acid was used to prepare the copper and lead solutions. The Cu(II) and Pb(II) concentrations were 100 mM for the high concentration solutions, and 10 mM for the low concentration solutions. A 2.5% by weight solution of 10 µm polystyrene latex beads was added in a volume ratio of 1 to 20 of the stock solution on the chip. The final copper and lead concentrations were 95.2 mM for the "high concentration" and 9.52 mM for the "low concentration" in 95.2 mM nitric acid electrolyte. A glass microscope slide was placed over the solution and seated on the gasket to make an electrochemical cell. The cell was placed under a microscope as depicted in Figure 2c.

4.3.5. Electrochemical Control.

A CHI 760B potentiostat/galvanostat (CH Instruments, Austin, TX) was used for chronopotentiometry experiments. A band electrode in the array served as a working electrode in all experiments. In the one-band experiment, electrochemical deposition was performed at the working electrode, which served as the cathode. That working electrode was then used as the anode in the two-band experiment without changing solutions to avoid loss of the deposited material. The quasi-reference electrode was one of the medium-sized (800 × 6000 μm) bare gold electrodes labeled in Figure 2a. The counter electrode was one of the large (5000 × 8000 μm) gold electrodes labeled in Figure 2a for the one-band electrode experiment and served as the anode. A band electrode 260 μm away from the working band electrode in the array served as the counter (and cathode) electrode for the two-band electrode experiment. Applied currents of 10 μA for high metal concentration solutions and 2 μA for low metal concentration solutions were used in the chronopotentiometry experiments. To protect the gold electrodes, the galvanostat was set to end when the potential response went above 0.5 V or below -1.3 V vs the gold quasi-reference electrode. Otherwise, the experiment was ended manually by clicking the stop button.

4.3.6. Bead Video Microscopy Analysis.

The bead movement was observed with a Nikon Eclipse ME600P microscope, and movies were recorded using a Sony Handycam digital camera (model no. HDR-XR500V, 30 fps with 720 × 480 pixels per frame). For high concentration experiments every tenth frame recorded in a 3.3 s video segment was extracted as a still image Due to the slower bead speeds in the low

concentration experiments, every 30th frame recorded in a 10 s video segment was extracted as a still image. The extracted frames were loaded into DynamicStudio v.3.00 software (Dantec Dynamics, Copenhagen, Denmark) for particle image velocimetry (PIV) analysis as described in Scrape et al. [24]. Note that the term "PIV" used here refers to the processing of the optical microscopy videos of the microbeads.

Velocities for the one-band deposition studies were measured along the inactive electrode next to the working electrode on the right side in the images. Velocities for the two-band case were measured along the inactive electrode next to the anode on the right side. The beads in focus at a height of 150 μm from the chip were analyzed to determine fluid motion. The depth of focus for the microscope in all the experiments was ~150 μm, as measured in a separate study by focusing onto beads of known diameter immobilized on a glass slide.

4.4. Results and Discussion

4.4.1. Calculations of Forces for Density Gradients and Magnetoconvection for Copper and Lead Cases

Calculations using the equations for $\mathbf{F}_{\nabla C}$, $\mathbf{F}_{\nabla B}$, $\mathbf{F}_B$, and $\mathbf{F}_g$ can be performed to estimate the relative strengths of the forces for the electrochemical systems under investigation here. Their values can be used to aid in comparing their relative contributions to the experimentally obtained fluid velocities. First, the concentration profiles are obtained for a particular time, which is needed for determining $\mathbf{F}_{\nabla C}$, $\mathbf{F}_{\nabla B}$, and $\mathbf{F}_g$. Then, these forces, in addition to $\mathbf{F}_B$ are discussed.

4.4.1.1. Calculations of Concentration Profiles and the Density Gradient Force

The magnitudes of $\mathbf{F_g}$, $\mathbf{F_{\nabla B}}$, and $\mathbf{F_{\nabla C}}$ can be calculated using a similar method to obtain the concentration profile as that used Chapter 2, with the same limitations. For the sake of simplicity an existing equation was used that involves planer diffusion even though the diffusion is radial. Therefore these calculations are only crude estimates. The experiments with Cu^{2+} and Pb^{2+} involve applying a current instead of a potential, and require equation 5 to find the concentrations of Cu^{2+} and Pb^{2+} as a function of the distance from the electrode [17].. C_m is the concentration of Cu^{2+} or Pb^{2+} at a certain distance from the electrode, C_m^* is the concentration of Cu^{2+} or Pb^{2+} in the bulk solution, D_m is the diffusion coefficient of Cu^{2+} or Pb^{2+} (where D_{Cu2+} = 7.14×10^{-6} cm^2/s [17] and D_{Pb2+} = 5.50×10^{-6} cm^2/s [16] A is the area of the electrode, i is the applied current, d is the distance from the electrode, and n is the number of electrons transferred per atom, which is 2 for Cu^{2+} and Pb^{2+}.

$$C_m = C_m^* - \frac{i}{nFAD_m}\left\{2\left(\frac{D_m t}{\pi}\right)\exp\left(-\frac{d^2}{4D_m t}\right) - d\ \mathrm{erfc}\left[\frac{d}{2(D_m t)^{1/2}}\right]\right\} \tag{5}$$

The charge difference caused by the electrodeposition of copper or lead is found in equation 6, and is the difference between the concentration of Cu^{2+} or Pb^{2+} at a certain distance from the electrode and the bulk concentration. The equation also accounts for the fact that copper and lead are 2+ species in solution.

$$z_d = 2\left(C_m - C_m^*\right) \tag{6}$$

Each ionic species will compensate a fraction of the change in charge that occurs during the faradaic process. That fraction is the transference number, and is calculated using equation 2

113

for both the copper and lead systems. To keep the model simple here, however, it is assumed the charge is compensated for by the H^+ and NO_3^- only. The concentrations of the NO_3^- and H^+ are calculated using equation 7, where C_i is the concentration of NO_3^- or H^+ concentration at a certain distance, C_i^* is the bulk NO_3^- or H^+ concentration, and t_i is the transference number for NO_3^- or H^+.

$$C_i = C_i^* + t_i z_d \tag{7}$$

The concentrations were calculated for the Cu^{2+} and Pb^{2+} systems in both high and low concentrations. The results for Cu^{2+} and Pb^{2+} at the high concentration and for a constant current of 10 μA are found in Figures 3a and b. The concentration of metal ions near the cathode is much lower than in the bulk solution due to electrodeposition. The concentration of H^+ increases and that of NO_3^- decreases to compensate for the charge imbalance. The diffusion layer is thinner with Pb^{2+} due to its lower diffusion coefficient. The results for copper and lead at the low concentration ($1/10^{th}$ of the high concentration) and for which a lower current was used (2 μA, or $1/5^{th}$ of that used for the high concentration) are found in Figures 3c and d. The results are similar with one major exception, the concentrations of lead and copper ions become negative near the electrodes. This is due to the fact that the applied current is too high to be sustained by diffusional flux of the metal ions in this model. However, in the actual experiment, the diffusion is largely radial, and therefore allows for substantially higher flux.   If the current was set too high for the experiment, then some of that current would be supported by hydrogen reduction. The model does not involve any other faradaic processes other than metal reduction. In the experiment, however, the potential response for the copper solution at the lower concentration does not shift toward hydrogen reduction, and thus further suggests that the current is indeed
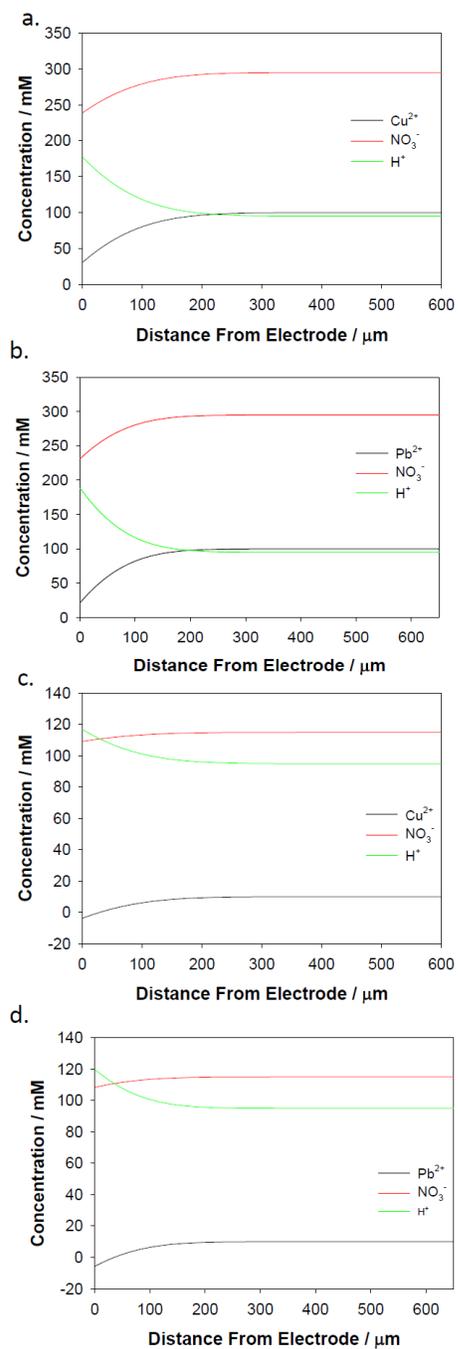
Figure 3 Calculated concentrations of Cu^{2+}, Pb^{2+}, H^+ and NO_3^- as a function of distance from electrode 10 s after the beginning of an applied current. The concentration of metal ions in the bulk that come from the metal nitrate and the current used are: (a) 100 mM Cu^{2+} and 10 µA, (b), 100 mM Pb^{2+} and 10 µA, (c) 10 mM Cu^{2+} and 2 µA, and (d), 10 mM Pb^{2+} and 2 µA. The bulk nitric acid concentration for all was 100 mM.

sustainable by diffusion. Therefore, the source of the error in the model is that it does not account for the higher radial flux.
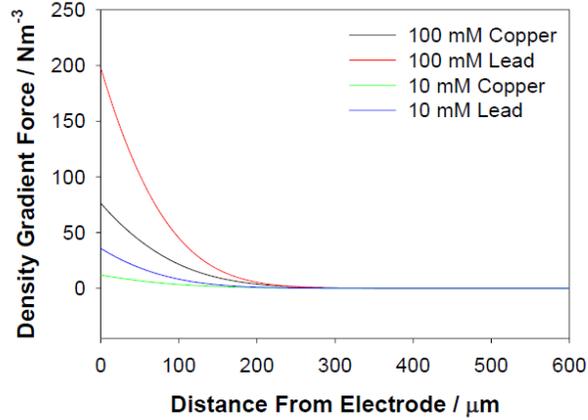
Figure 4. Calculated magnitude of $\mathbf{F_g}$ as a function of distance from the cathode using the concentrations from the four solutions from Figure 3.

The density gradient force, $\mathbf{F_g}$, is calculated in a similar manner to the ferri-ferrocyanide system as seen in equation 8 where m_{NO3}, m_H and m_m are the molecular weights of the nitrate ion, hydrogen ion, and the copper or lead ion, respectively.

$$\mathbf{F_g} = \mathbf{g}\left\{m_{NO_3}\left(C_{NO_3} - C_{NO_3}^*\right) + m_H\left(C_H - C_H^*\right) + m_m\left(C_m - C_m^*\right)\right\} \tag{8}$$

Figure 4 shows the resulting magnitudes of $\mathbf{F_g}$ as a function of the distance from the electrode. The magnitude of $\mathbf{F_g}$ for copper and lead is ten times larger than that for the ferri-ferrocyanide system found in chapter 2. When comparing the magnitudes of $\mathbf{F_g}$ in the high and low concentration solutions, $\mathbf{F_g}$ scales proportionally with applied current, which is expected.

Near the cathode, $\mathbf{F_g}$ points upward, which is supported by the upward motion of the less dense solution generated above the electrode.

4.4.1.2. Calculations of Magnetoconvective Forces for Copper and Lead Cases

Using equation 4, $\mathbf{F_{\nabla C}}$ near the cathode for the copper solution can be calculated. The magnitude of the magnetic flux density is obtained by using Amperes software, and is shown in Figure 5a. The $\mathbf{\nabla C_p}$ for copper ions in solution was determined the using equation 5 with the same conditions as $\mathbf{F_g}$. The results of calculations of $\mathbf{F_{\nabla C}}$ for both high and low concentration are found in Figure 5b. The maximum $|\mathbf{F_{\nabla C}}|$ is at the electrode surface. When comparing the magnitude of $\mathbf{F_{\nabla C}}$ for the high and low metal concentrations, it scales proportionally with applied current, just like $\mathbf{F_g}$, Also, $\mathbf{F_{\nabla C}}$ points toward the bulk solution, opposing diffusion of copper ions to the electrode, and in the same direction as $\mathbf{F_g}$ (Figure 1a and d). The magnitude of $\mathbf{F_{\nabla C}}$, is also two orders of magnitude larger than $\mathbf{F_g}$. Consequently, if $\mathbf{F_{\nabla C}}$ plays an important role, one would expect it to enhance the density gradient and therefore $\mathbf{F_g}$. Comparisons of fluid flow for the copper solution in experiments with and without a magnet would help to determine whether this prediction is valid.

Unlike $\mathbf{F_{\nabla C}}$, which only depends on the magnitude of $\mathbf{B}$, and not the direction, one must consider the x, y and z components to solve the $(\mathbf{B \cdot \nabla})\mathbf{B}$ term from equation 3 to calculate $\mathbf{F_{\nabla B}}$. The term has a complex relationship with the $\mathbf{B}$ as seen when ∇ and $\mathbf{B}$ are separated into x, y, and z components, resulting in the equation 9, where, $\mathbf{B_X}$, $\mathbf{B_y}$, and $\mathbf{B_z}$ are the x, y and z components of the magnetic flux density, and $\mathbf{i}$, $\mathbf{j}$, and $\mathbf{k}$ are unit vectors in the x, y, and z

117

direction. (Note: i and j here should not to be confused with electronic and ionic currents, respectively, that are assigned to these variables elsewhere in the chapter.)

$$(\mathbf{B}\cdot\nabla)\mathbf{B} = \mathbf{i}\left(\mathbf{B}_x\frac{\partial\mathbf{B}_x}{\partial x} + \mathbf{B}_y\frac{\partial\mathbf{B}_x}{\partial y} + \mathbf{B}_z\frac{\partial\mathbf{B}_x}{\partial z}\right) + \mathbf{j}\left(\mathbf{B}_x\frac{\partial\mathbf{B}_y}{\partial x} + \mathbf{B}_y\frac{\partial\mathbf{B}_y}{\partial y} + \mathbf{B}_z\frac{\partial\mathbf{B}_y}{\partial z}\right) +$$
$$\mathbf{k}\left(\mathbf{B}_x\frac{\partial\mathbf{B}_z}{\partial x} + \mathbf{B}_y\frac{\partial\mathbf{B}_z}{\partial y} + \mathbf{B}_z\frac{\partial\mathbf{B}_z}{\partial z}\right)$$

(9)

In the experiments B_z is orders of magnitude greater than B_x and B_y, allowing us to simplify the equation greatly as seen in the equation 10. It should be noted that the gradient of the x and y components of **B** may not be negligible.

$$(\mathbf{B}\cdot\nabla)\mathbf{B} = \mathbf{i}\mathbf{B}_z\frac{\partial\mathbf{B}_x}{\partial z} + \mathbf{j}\mathbf{B}_z\frac{\partial\mathbf{B}_y}{\partial z} + \mathbf{k}\mathbf{B}_z\frac{\partial\mathbf{B}_z}{\partial z}$$

(10)

The change in Bz across the length and width of the band electrode in the x and y plane is very small (gradient in the z direction is 41.2 T/m at the edges and 41.8 T/m with the magnitude for **Bz** at a constant 0.4834 T). This means the expanded form of $(\mathbf{B}\cdot\nabla)\mathbf{B}$ can be simplified even further, resulting in equation 11.

$$(\mathbf{B}\cdot\nabla)\mathbf{B} = \mathbf{k}\mathbf{B}_z\frac{\partial\mathbf{B}_z}{\partial z}$$

(11)

To calculate $\mathbf{F}_{\nabla B}$ the equation 11 is used for the term in equation 3. The value of B_z at a given distance, z, from the electrode and the change of B_z with z can be obtained from Figure 5a. The average gradient of B_z across the entire height of the cell is 0.462 T. The value of C_p was already calculated as a function of distance from the electrode and is shown in Figure 3a and d

for copper. The results of the calculations for $F_{\nabla B}$ for both high and low concentrations are found in Figure 5c. Unlike $F_{\nabla C}$ and F_g, $F_{\nabla B}$ is smallest at the electrode surface, increases to a maximum at the extent of the diffusion layer and then declines gradually into the bulk with the declining magnetic field where it scales proportionally with the copper concentration, not with current. Also, because the current used for $1/10^{th}$ the concentration was only $1/5^{th}$, drawing the concentration profile in the diffusion layer down faster relative to the bulk concentration, $F_{\nabla B}$ drops even more than $1/10^{th}$ at the lower concentration when compared to the conditions at the higher concentration.

$F_{\nabla B}$ also affects the whole solution. This is different from $F_{\nabla C}$, which affects only the diffusion layer. The direction of $F_{\nabla B}$ points towards the higher magnetic field; in this case, it is downward toward the electrode surface. Therefore if $F_{\nabla B}$ plays a significant role, it will draw copper ions toward the electrode from bulk, enhancing the net direction of diffusion, decreasing the concentration gradient in the diffusion layer, and therefore decreasing the density gradient. The net impact will likely cause F_g to be suppressed than it would be in the absence of the magnet. The $F_{\nabla B}$ is slightly lower, but same order of magnitude as F_g and points in the opposite direction. The calculations suggest that $F_{\nabla C}$ should dominate near the electrode surface where it is 150 times that of $F_{\nabla B}$. However, everywhere outside the diffusion later, where $F_{\nabla C}$ is zero, $F_{\nabla B}$ will play a significant role and oppose $F_{\nabla C}$ along that boundary. Consequently there could be an even steeper concentration profile at the electrode, which would enhance $|F_g|$. Monitoring how the resulting solution velocities change due to F_g in the presence and absence of the magnet will therefore be key in determining whether $F_{\nabla C}$ is really a valid force or not. Those changes in

119
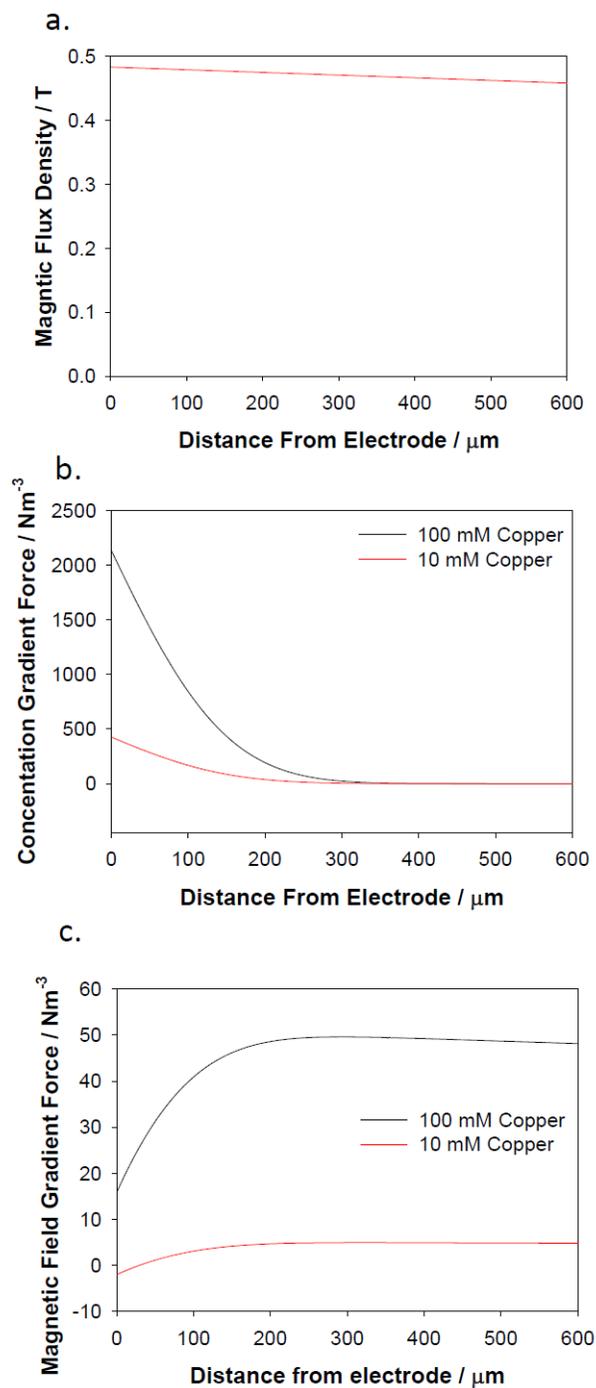
Figure 5. (a) Calculated magnitude of **B**, (b) $\mathbf{F_{\nabla C}}$, and (c) $\mathbf{F_{\nabla B}}$ as a function of distance from electrode using the concentrations and currents for the four solutions from Figure 3.

velocities for copper will be compared experimentally to ones in the lead solution, which are the controls.

The force $\mathbf{F_B}$ occurs only when ionic current is turned on in the presence of a perpendicular magnetic field. It is independent of the concentration and type of metal species, with the exception of where a change in composition alters the viscosity of the solution. In general, a lead solution of the same concentration as a copper solution would have a higher density. Likewise, a higher concentration of a solution with the same type of metal would increase the density and therefore increase the viscosity. Higher solution densities will result in lower MHD velocities for a fixed current and magnetic field. For the sake of simplicity we are doing the two-band setup and assume that the ion current runs exclusively between the anode and cathode, across a 1000×2000 micron cross section. These calculations of $|\mathbf{F_B}|$ at the electrode surface, where the B_z is largest and assuming the all ionic current is perpendicular to B_z, for a 10 μA current yields 2.42 N m^{-3}, and the value for a 2 μA current is 0.483 N m^{-3}. Values at the lid of the cell are only slightly lower because of the slightly lower magnetic field there 2.21 N m^{-3} and 0.441 N m^{-3}, respectively. The magnitude of $\mathbf{F_B}$ is two orders of magnitude smaller than $|F_g|$ and $|\mathbf{F_{\nabla B}}|$ but is pointed perpendicular to them, and is present everywhere there is ionic current (between the pair of electrodes in the two-band case and radially outward from the electrode in the one-band case). Comparing the fluid speed in the direction of the MHD between the copper and lead solutions will allow us to determine whether the viscosity is significantly different.

Fluid flow due to $\mathbf{F_B}$ will distort the developing concentration gradients and should be greater in the solutions with higher MHD speeds. When the current is turned off, $\mathbf{F_g}$, $\mathbf{F_{\nabla B}}$, and

121

$F_{\nabla C}$ forces remain for the copper solution and only the F_g force remains in the case of lead. A comparison of experimentally obtained fluid flow of the solution containing the paramagnetic species to that with the diamagnetic species will reveal whether $F_{\nabla B}$ or $F_{\nabla C}$ dominate.

4.4.2 Chronopotentiometry Responses and Timing of PIV Measurements.

Experiments herein involved applying a constant current to the electrodes, as opposed to a constant potential, to precisely control both $|\mathbf{j}|$, which is important in F_B, and the conversion rate of copper and lead at the electrodes, which is important in generating the other forces. Previous investigations of constant current control in small volumes have established a linear dependence of MHD fluid velocity [25] and allowed careful studies of MHD flow patterns and profiles [23, 26]. Applied current has also been used to investigate the effect of F_g in electrochemical systems due to density gradients [14, 27] (See Chapter 2). Before engaging in discussion about the forces contributing to the fluid motion, it is of interest to first examine the chronopotentiometry responses.

Figure 6 shows cyclic voltammetry responses for a one-band configuration in electrodeposition solutions having the high concentrations of copper and lead. Both show the characteristic reduction of metal on the forward sweep and subsequent stripping that produces a surface wave on the reverse sweep. The hysteresis between the forward and reverse sweeps is consistent with the change in the surface properties during the sweep where the electrodeposition begins on gold, and transitions to that on the lead or copper. A small amount of hydrogen reduction is present during the lead CV as there is a second redox species visible. In addition the lead CV has much higher current, this is due to the deposited lead creates spikes that increase the
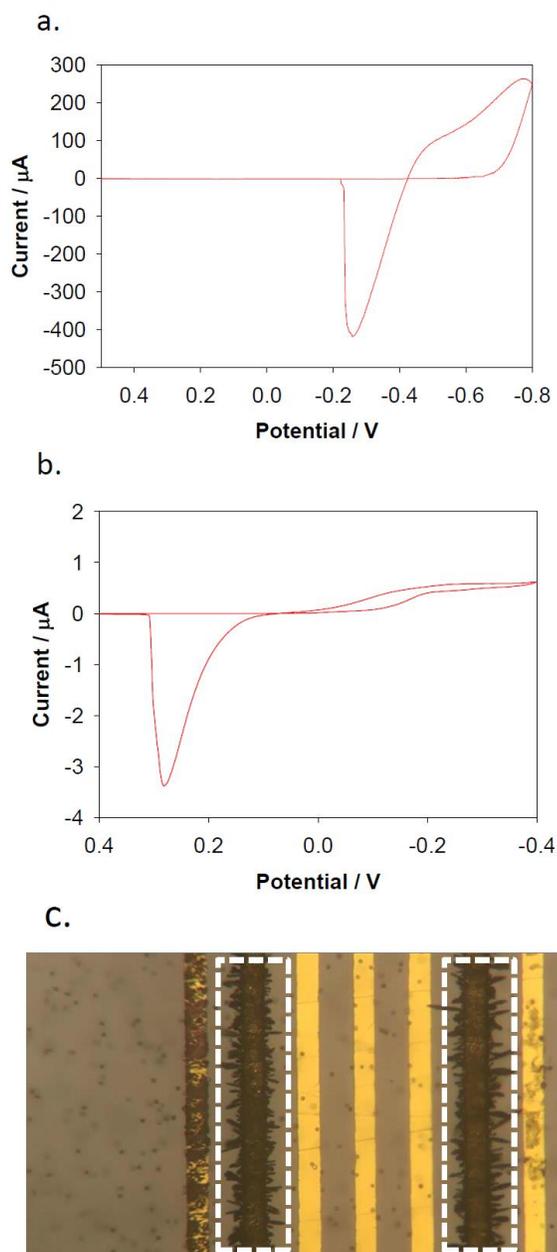
Figure 6. CV responses for a. lead and for b. copper at the high concentrations using a 12.5 μm Au disk working electrode Pt flag counter electrode and a Ag/AgCl sat. KCl reference electrode. The scan rate was 0.1 V/s. $Cu(NO_3)_2$ and $Pb(NO_3)_2$ concentrations were 100 mM with 100 mM HNO_3 c. Image of lead deposited on two band electrodes during a 30 s chronoamperometry experiment (-1 V) using same solution, cell, counter electrode, and working electrode as the deposition experiments in figures 9 and 10. The active electrode are outlined with a dashed white box.

Figure 7. Chronopotentiometry responses of copper (red curves) and lead (black curves) at a high concentration (95.2 mM) for deposition with a magnet (a and c) and without a magnet (b and d), for the one-band case (a and b), where the working electrode served as the cathode, and the two-band case (c and d), where the working electrode served as the anode. For a-c, black bars on the x axis indicate when PIV measurements were made for both the copper and lead solutions. For d, black bars indicate when PIV measurements were made for lead, and red bars for copper. PIV 1 is taken immediately before and PIV 2 is taken immediately after the end of the applied current.

124

electrode area result in a higher current. This can be seen in Figure 6c where deposited lead has created spikes on a band electrode and increased the area.

Figure 7 shows typical potential responses at the cathode for copper and lead in the presence and absence of the magnet and for the one-band and two-band cases. These were obtained for the high metal concentrations and an applied current of 10 µA. The measured potential during the experiment for lead is more negative than that for copper, because of its more negative standard reduction potential ($E° = -0.1251$ V for Pb(II/0) and 0.159 V for Cu(II/0) vs. NHE) [17]. The potential varies during the experiment, shifting more negative, as metal deposits on the electrode and metal ion concentration in the nearby solution is depleted, as would be expected from the Nernst equation. Also, in the presence of the magnet, the potential shifts slightly more positive, presumably because of increased delivery of metal ions from solution due to enhanced convection. The potentials are generally more positive for the two-band than the one-band experiment, because the working electrode switches from cathode to anode.

The one-band electrode and two-band electrode experiments were repeated for one-tenth of the metal concentration and one-fifth of the applied current. This allows us to get a better understanding of $\mathbf{F_{\nabla B}}$, $\mathbf{F_{\nabla C}}$, $\mathbf{F_B}$, and $\mathbf{F_g}$ because $\mathbf{F_{\nabla B}}$ decreases proportionally with concentration while $\mathbf{F_{\nabla C}}$, $\mathbf{F_B}$, and $\mathbf{F_g}$ decrease proportionally with current. The chronopotentiometric responses are shown in Figure 8. Overall, the trends in the potential responses are similar to those at the higher concentration and current. The potential for the one-band experiment using copper at low concentrations is 0.2 V more negative than at the high concentration. This is expected based on the Nernst equation. The potential for the one-band experiment using lead does not show a change in potential mainly due to the interference of hydrogen reduction. The sudden increase in

potential at the end of the experiment in Figure 8c is the result of stripping all the deposited lead off the electrode. The potential for the two-band electrode experiments do not change when the concentration is decreased most likely due to the fact that at the anode (the electrode where potential is measured) the concentration of copper or lead is much higher than the bulk concentration.

PIV analysis of the bead movement was obtained to determine the fluid velocity at two different times during each chronopotentiometry experiment. One analysis was performed during the last 3.3 s before the end of the applied current (PIV 1) and one for the first 3.3 s after the applied current ended (PIV 2). The times for these measurements are similar for both the copper and lead cases and are indicated in Figures 7 and 8. The one-band experiments are around 60 s long to ensure there is enough deposited metal for the 30 s two-band experiment. In three instances, the experiment for one metal lasted a few seconds longer than for the other metal (see Figure 7d and Figure 8a and c. This should not impact the results significantly as the velocity measurements are obtained immediately before and after the end of the applied current and at long times when a pseudosteady state appears to have been established. The resulting vector images of fluid velocity for all of the different experiments are shown in Figures 9-12. Convection during PIV 1 is caused by electrochemically generated density gradients for copper and lead and magnetoconvective forces for copper. Convection during PIV 2 cannot be due to $\mathbf{F_B}$, but may result from $\mathbf{F_g}$ for both metals, and $\mathbf{F_{\nabla B}}$, and $\mathbf{F_{\nabla C}}$ for copper alone. A more detailed discussion of the velocities under the different conditions is provided in the sections below.
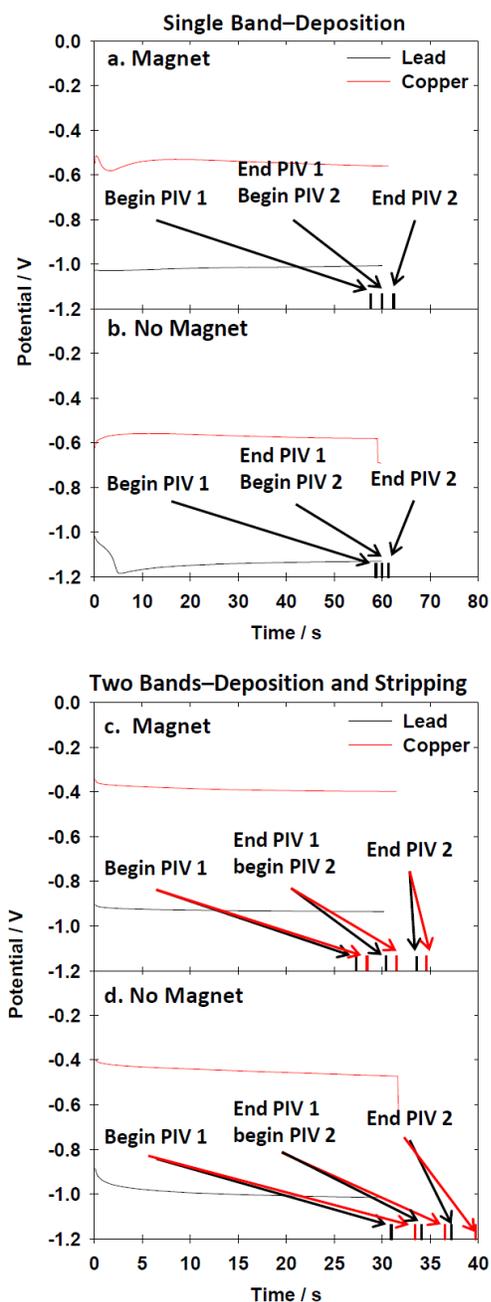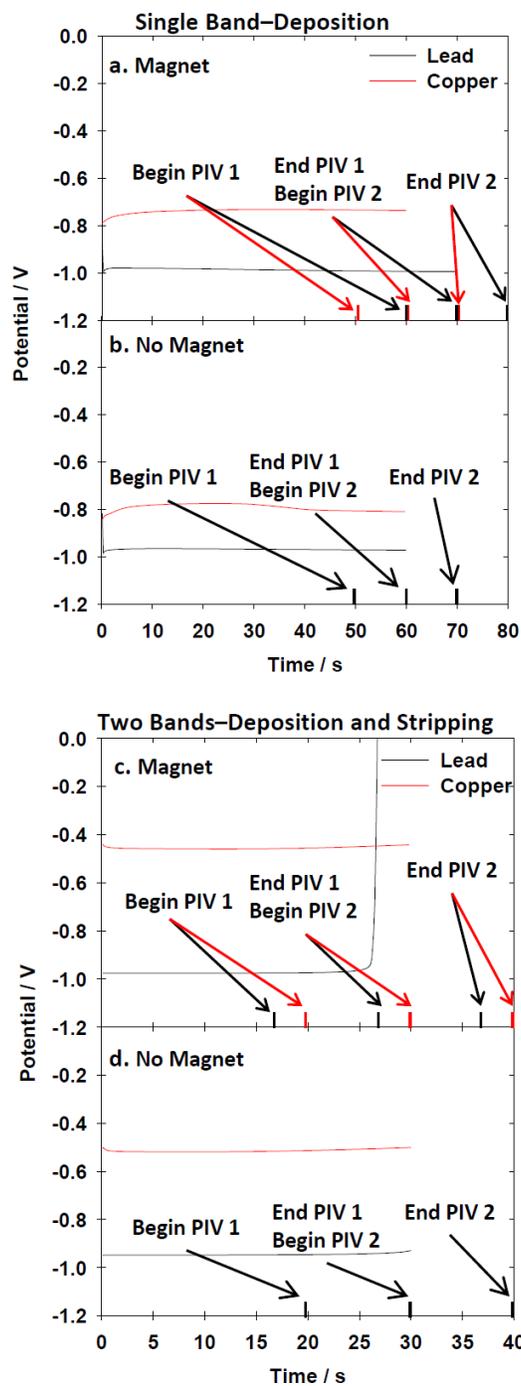
Figure 7. Chronopotentiometry responses of copper (red curves) and lead (black curves) for deposition at a low concentration (9.52 mM) with a magnet (a and c) and without a magnet (b and d) a magnet, for the one-band case (a and b), where the working electrode served as the cathode, and the two-band case (c and d), where the working electrode served as the anode. For a-c, black bars on the x axis indicate when PIV measurements are made. For d, black bars indicate when PIV measurements were made for lead, and red bars for copper. PIV 1 is taken immediately before and PIV 2 is taken immediately after the end of the applied current.

127

4.4.3 Fluid Motion for the One-Band Electrode Case at "High" Concentration and Current

The primary purpose of the one-band experiments is to deposit lead or copper on an electrode that is later used as an anode for the two-band experiments. However, it is also useful to study the fluid movement during and immediately following the deposition for this case. The electrochemically-generated density gradients are simpler because they originate at only one electrode, however, $\mathbf{F_B}$ produces an oval flow pattern that is more difficult to analyze than the straight flow for the two-band case. The velocity maps for the deposition of copper and lead in the presence and absence of the magnet for the one-band case are shown in Figure 9. The absolute magnitudes ($|\mathbf{u}|$), and the x (u_x) and y (u_y) components of the fluid velocities are shown in Table 2.

In the absence of the magnet for the high metal concentration ($C^* = 95.2$ mM) and current ($i = 10$ μA), electrodeposition at the electrode causes fluid convection with a magnitude in the x direction of $u_x = -16.1 \pm 0.5$ μm/s for copper (Figure 9c) and $u_x = -18 \pm 3$ μm/s for lead (Figure 9g). This $\mathbf{F_g}$-induced flow converges in a straight line directly over the electrode. This can be explained by the less dense solution rising from the electrode while solution from the sides flows in to replace it. Video microscopy at only 150 μm above the surface of the chip clearly shows this behavior. (At the lid, the solution spreads outward to complete the fluid circulation.) According to the calculations, the average ratio of $|\mathbf{F_g}|$ for Pb^{2+} / $|\mathbf{F_g}|$ for Cu^{2+} is 2.07. For comparison, the ratio of the x-components of the fluid speeds is 1.12, which is lower by almost a factor of two (1.8). It is unclear at this time as to the source of this error. One limitation of the simple model is that only H^+ and NO_3^- migrate to compensate charge during reduction. If in

Table 2. Averages and standard deviations of the x component, y component and magnitude of the fluid velocities obtained during and immediately after copper and lead deposition and stripping. Velocities were measured for the last 3.3 s before the end of the applied current and for the first 3.3 s after the applied current ended. The velocities were measured 200 μm from the cathode (right side of electrode) in the one-band case, and 200 μm from the cathode (left side of cathode and between the anode and cathode) in the two--band case. (Errors represent +/- one standard deviation of the component of the vectors in the PIV image along the entire length of that location along the electrode.)

			One-Band During Deposition Current (μm/s)	One-Band After Deposition Current (μm/s)	Two Bands During Deposition/ Stripping Current (μm/s)	Two Bands After Deposition/ Stripping Current (μm/s)
High Concentration						
Copper	With Magnet	x	-12 ± 8	-2 ± 2	3 ± 1	11.5 ± 0.9
		y	34 ± 4	19 ± 4	-35 ± 4	-2 ± 2
			37 ± 4	20 ± 4	36 ± 3	11.8 ± 0.8
	No Magnet	x	-16.1 ± 0.5	-15.2 ± 0.6	13 ± 1	15 ± 1
		y	0.6 ± 1.2	0.5 ± 1.3	-0.2 ± 0.3	0.07 ± 0.31
			16.2 ± 0.6	15.3 ± 0.5	13 ± 1	15 ± 1
Lead	With Magnet	x	-17 ± 10	-20 ± 3	19 ± 1	21.0 ± 0.5
		y	38 ± 9	5 ± 7	-66 ± 2	-1.0 ± 0.4
			43 ± 5	22.2 ± 0.7	69 ± 3	21.0 ± 0.5
	No Magnet	x	-18 ± 3	-19 ± 2	19 ± 1	21.0 ± 0.5
		y	1 ± 1	2.0 ± 0.8	2.1 ± 0.8	2.2 ± 0.8
			18 ± 3	19 ± 2	20 ± 1	19 ± 2
Low Concentration						
Copper	With Magnet	x	4 ± 2	-1 ± 1	0.4 ± 0.4	2.8 ±0.4
		y	7.0 ± 0.8	3 ± 1	-10 ± 2	1.7 ± 0.5
			8.4 ± 0.4	3.7 ± 0.5	10 ± 2	3.3 ± 0.3
	No Magnet	x	-1.6 ± 0.1	-2.2 ± 0.1	3.5 ± 0.1	4.9 ± 0.1
		y	0.03 ± 0.06	0.06 ± 0.29	-0.27 ± 0.07	-0.21 ± 0.09
			1.6 ± 0.2	2.2 ± 0.2	3.5 ± 0.1	4.9 ± 0.1
Lead	With Magnet	x	-5 ± 3	-8 ± 1	0.4 ± 0.2	6.2 ± 0.3
		y	6.2 ± 0.8	1 ± 2	-17 ± 1	-0.8 ± 0.3
			8.1 ± 0.9	8 ± 1	18 ± 1	6.3 ± 0.2
	No Magnet	x	-4 ± 0.4	-6.2 ±0.6	4.2 ± 0.3	6.3 ± 0.2
		y	0.8 ± 0.5	1.0 ± 0.7	0.9 ± 0.3	0.9 ± 0.2
			5.3 ± 0.3	6.3 ± 0.5	4.3 ± 0.3	6.3 ± 0.2

addition to diffusion, the divalent metal ions were allowed to migrate from the bulk into the diffusion layer, as well, the density gradient and therefore $|\mathbf{F_g}|$ would decrease. However, if we were to account for migration of the metal dications, the higher transference number for Cu(II) (Table 1) would cause a greater decrease in $|\mathbf{F_g}|$ for Cu(II) than for Pb(II), and thus, the ratio $|\mathbf{F_g}|$ for Pb^{2+} / $|\mathbf{F_g}|$ for Cu^2, would increase, not decrease. Another possibility is the fact that lead deposition

is likely to involve some hydrogen reduction, decreasing the density gradients for Pb(II) below that expected and thereby decreasing the actual ratio $\mathbf{F_g}|$ for Pb^{2+} / $|\mathbf{F_g}|$ for Cu^{2+}. Another explanation is if the viscosity of the lead solution is greater than that of the copper solution, the velocity of the lead solution would be slower for the same applied force.

When the current is turned off (without a magnet), convection continues in the same direction, with speeds of $u_x = 15.2 \pm 0.6$ μm/s for copper (Figure 9g) and $u_x = 19 \pm 2$ μm/s for lead (Figure 9h), which are within error of the values before the current was turned off. These results suggest that it may be possible in the presence of a magnet to separate out the contributions to fluid flow of forces that depend on concentration gradients, such as $\mathbf{F_g}$, simply by turning off the current, when $\mathbf{F_B}$ becomes zero. It would also be an indirect way to map out the impact that MHD has on concentration gradients.

When a magnet is placed below the chip, a different convection is observed during electrodeposition at the electrode. The fluid circulates in a horizontal plane in the direction that generally follows the right hand rule for MHD, and is dominated by flow in the y direction (to the side and along the length of the electrode), which is $u_y = 34 \pm 4$ μm/s for copper (Figure 9a)

Figure 9. Microscope images superimposed with velocity vectors from PIV analysis for copper (a-d) and lead (e-h) deposition for a high concentration (95.2 mM) at a one-band with a magnet (a,b and e, f) and without a magnet (c, d and g, h). PIV images were obtained during (a, c) and after (b, d) deposition of copper. Likewise, PIV images were obtained during (e, g) and after (f, h) deposition of lead. For PIV images taken during deposition, the velocity was measured during the last 3.3 s of the deposition. For PIV images taken after deposition, the velocity was measured for 3.3 s after the current was turned off and deposition ended. (See Figure 6a and b). The electrode undergoing deposition is outlined with a dashed white line (only ~1/5 of its entire length is shown) and is labeled with "-" when activated as a cathode and "X" when returned to open circuit.

and $u_y = 38 \pm 9$ µm/s for lead (Figure 9e) at 200 µm away. This flow circulates around a central point on the band electrode. This pattern has been observed previously for solutions containing both oxidized and reduced forms of freely diffusing redox species [22]. The speed reaches a maximum to the side of the electrode (at 225 µm from the edge of the electrode for both for copper and lead solutions) and then drops off with the increasing distance and therefore decreasing current density. Because the MHD force depends on the current density, it should not matter whether the redox species is Cu(II) or Pb(II) in solution, as long as their ionic current paths are the same, which we expect. However, differences in viscosities of the two solutions would cause differences in the MHD velocities between the metal solutions. If there is a sufficient $F_{\nabla B}$ force, it could establish a magnet-induced density gradient in the paramagnetic copper solution, increasing the density at the chip than in the absence of the magnet. Uhlemann and coworkers have reported this effect recently for a different system [28]. This could lead to a higher viscosity and therefore slower MHD fluid flow near the chip. This concept is further discussed in the two-band electrode configuration where the fluid flow due to the MHD force is easier to measure because it is parallel to the electrodes.

When the current is turned off in the presence of the magnet (Figures 9b and f), the fluid speed is similar for each metal as it was without a magnet ($|u| = 20 \pm 4$ µm/s for copper and $|u| = 22.2 \pm 0.7$ µm/s for lead), but the convergence point is shifted to the right of the electrode and the direction is no longer perpendicular to the length of the band. This is because the MHD disturbs the diffusion layer, pushing it in the direction of flow, such as upward on the right side of the electrode in the images shown in Figure 9a and e. The regions of lowest magnetoconvection however receive the least perturbation. The direction of fluid motion when
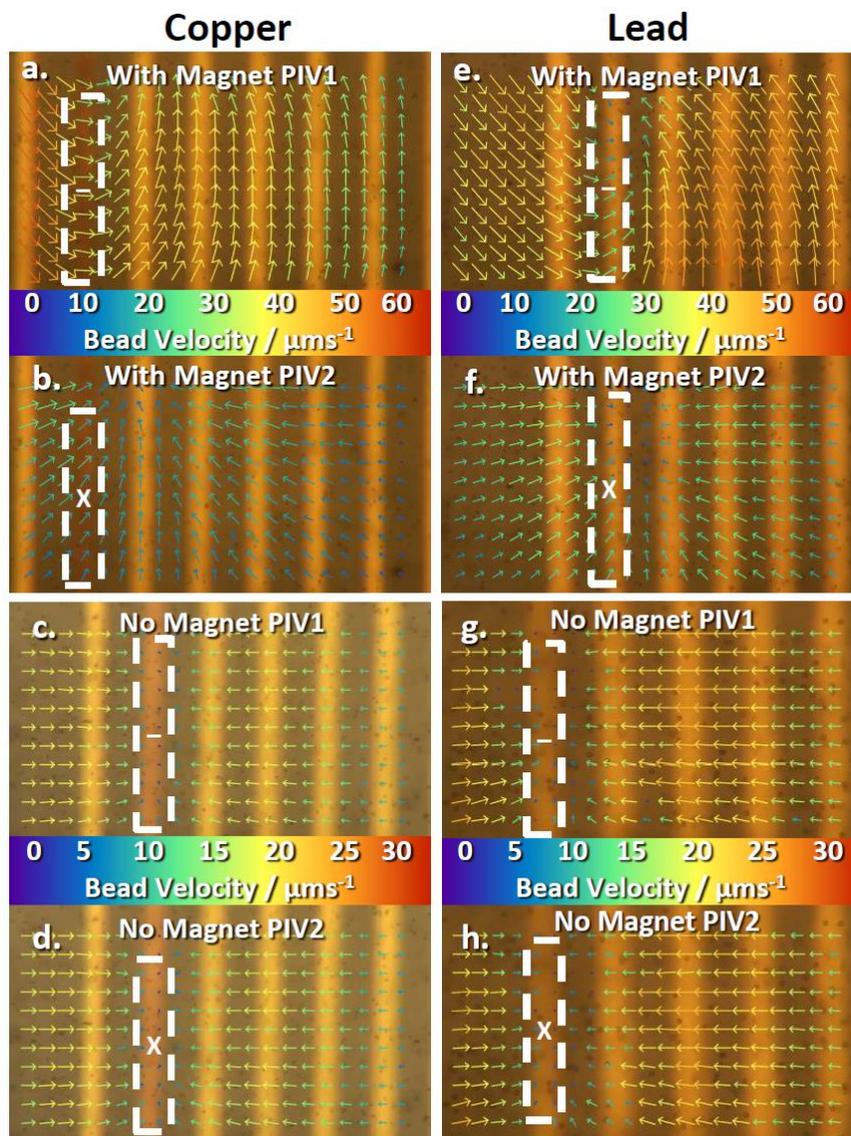
132
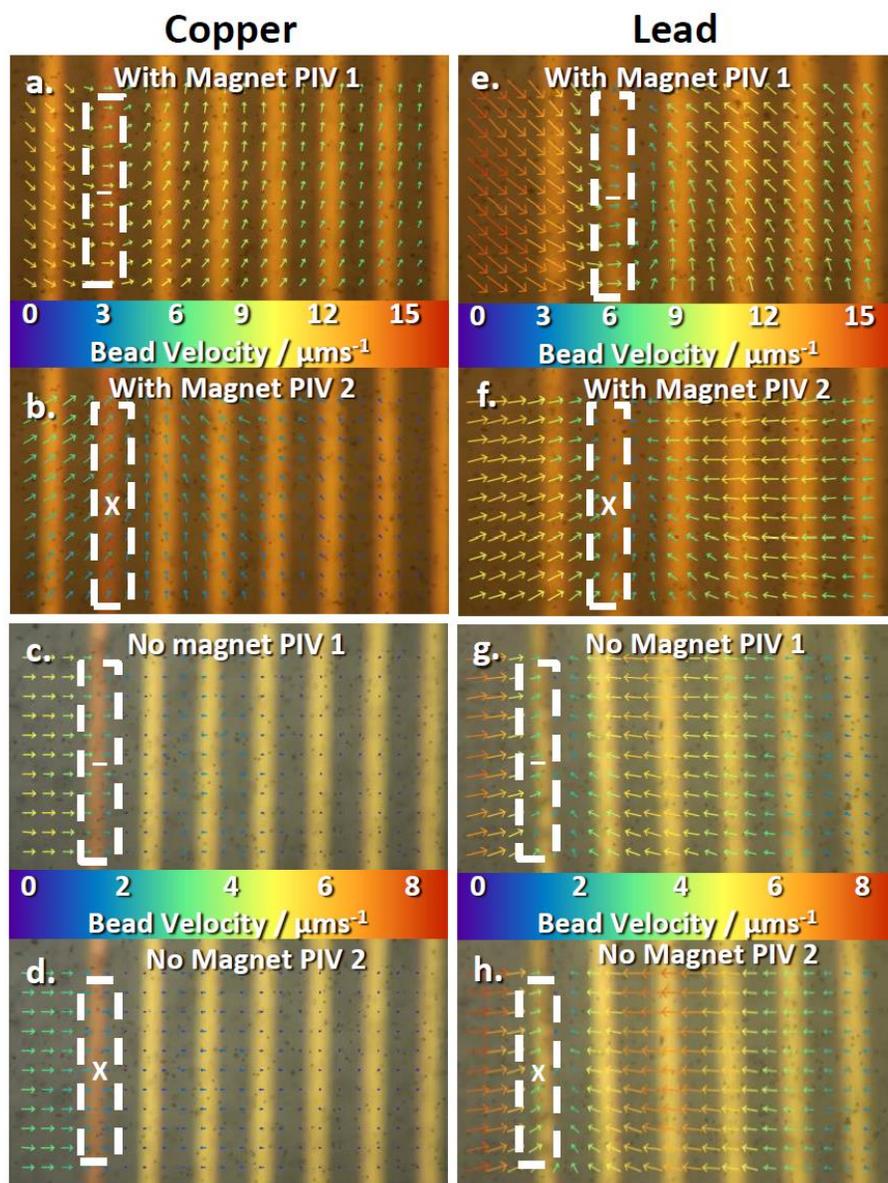
Figure 10. Microscope images superimposed with velocity vectors from PIV analysis for copper (a-d) and lead (e-h) deposition for a low concentration (9.52 mM) at a one-band with a magnet (a, b and e, f) and without a magnet (c, d and g, h). PIV images were obtained during (a, c) and after (b, d) deposition of copper. Likewise, PIV images were obtained during (e, g) and after (f, h) deposition of lead. For PIV images taken during deposition, the velocity was measured during the last 3.3 s of the deposition. For PIV images taken after deposition, the velocity was measured for 3.3 s after the current was turned off and deposition ended. (See Figure 8a and b). The electrode undergoing deposition is outlined with a dashed white line (only ~1/5 of its entire length is shown) and is labeled with "-" when activated as a cathode and "X" when returned to open circuit.

the current is turned off is consistent with this relocation of the largest density gradients for both

the paramagnetic and diamagnetic metal solutions, and thus, appears dominated by $\mathbf{F_g}$ in both

cases. If $\mathbf{F_{\nabla B}}$ made a significant contribution, then paramagnetic Cu(II) would be pulled toward

the chip in the direction of the highest magnetic field gradient, counteracting the

electrochemically generated density gradient and therefore $\mathbf{F_g}$. If $\mathbf{F_{\nabla C}}$ made a significant

contribution, then remaining paramagnetic species would move away from the depleted layer,

toward the higher concentration of Cu(II) in the bulk, enhancing the density gradient. It would

appear that if $\mathbf{F_{\nabla B}}$ and $\mathbf{F_{\nabla C}}$ do play a role, their effects on the fluid velocity in these one-

electrode experiments cancel out.

4.4.4 Fluid Motion for the One-Band Electrode Case at "Low" Concentration and Current

A change in the concentration of metal species and applied current would provide an

opportunity to determine the consistency of our interpretations and to vary the magnitudes of $\mathbf{F_{\nabla B}}$

and $\mathbf{F_{\nabla C}}$ relative to each other. The metal concentrations were decreased to $1/10^{th}$, and the current

was decreased to $1/5^{th}$ (a current of 10 µA is not sustainable by the mass transport at this lower

concentration). Calculations supporting how the forces depend on this change of conditions were

given in the Section 4.4.2. Assuming that the viscosity of the new solution is the same as the

more concentrated one, $|\mathbf{F_B}|$ should decrease to $1/5^{th}$, because it depends proportionally on $|\mathbf{j}|$.

Likewise, $|\mathbf{F_g}|$ and $|\mathbf{F_{\nabla C}}|$ should drop to $1/5^{th}$, because electrochemically-generated density

gradients also depend proportionally on current. However, we would expect $\mathbf{F_{\nabla B}}$ in the bulk

directed to the floor of the chip to decrease proportionally with concentration, to $1/10^{th}$, and to

achieve even smaller magnitudes at the electrode with greater applied current, and thus to have

an even weaker counteracting effect on the density gradients than for the case with the higher

concentration and current. Experimentally obtained velocity vectors are shown in Figure 10 and

the magnitudes of the x and y components are summarized in Table 2.

In the absence of the magnet for the low metal concentration ($C^* = 9.52$ mM) and at $1/5^{th}$

the current ($i = 2$ μA), the flow during electrodeposition converges in a straight line directly over

the electrode due to F_g, similar to the behavior observed at the higher concentration and current.

The velocity is primarily in the x direction with a speed of $u_x = -1.6 \pm 0.1$ μm/s for copper (Figure

10c) and $u_x = -4 \pm 0.4$ μm/s for lead (Figure 10g). The ratio of the speed for the lead solution to

that of the copper solution is 2.5, double that at the high concentration is 1.1, and greater than the

average ratio from the simulation, which is 2.07. The competition of hydrogen reduction should

be worse in this case because the Pb^{2+} concentration has been decreased, the H^+ concentration

has not, and the current is not scaled down as much as the Pb^{2+}. However, this effect should

make the ratios at low concentrations smaller not larger. This result lends more confidence in

the experimental design at high concentrations. Another factor that may play a role is migration,

not for the metal ions because they are a lower concentration relative to the supporting

electrolyte (see transference numbers in Table 1), but rather for the microbeads used to follow

the fluid flow. In past studies, we had not found firm evidence of bead migration. However, the

10 fold decrease in the metal nitrate lowers the ionic strength, μ, to a level (0.13 M) below that

of the lowest μ of the earlier density gradient studies in Chapter 2 (0.26 M). Ionic strength can be

calculated with the following equation:

$$m = \frac{1}{2} \left([A] \, Z_A^2 + [B] \, Z_B^2 + [C] \, Z_C^2 + ... \right)$$

where [A], [B], [C]… are the concentrations of the different ion species and Z_A, Z_B, and Z_C…are their charge, respectively. Thus, it is possible that the lower μ in the lower concentration studies here, which is 1/3 that of the higher concentration solutions, in combination with the greater relative demand to carry charge due to the ionic current, may start to exhibit enough force on the slightly negatively charged beads that their velocities are affected and measurable. Migration of the beads away from the cathode, in the opposite direction of convection induced by the electrochemically generated density gradients, would result in an apparently slower speed in the x direction. Because the Cu(II) has a higher ionic mobility than Pb(II), the phenomenon will have a greater impact in the lead than in the copper solution. Although the speeds are so slow and with large error, this hypothesis is further supported by the subsequent studies.

When the current is turned off (without a magnet), the behavior is similar to that for the higher current. The convection continues in the same direction. However, the speeds of u_x= -2.2 $\pm$ 0.1 µm/s for copper (Figure 10g) and u_x= -6.2 $\pm$ 0.6 µm/s for lead (Figure 10h) are larger for both metal solutions than before the current was turned off. Although the error in the measurements for the lead solution before the current was turned off is large and we hesitate to overinterpret the increased speed, the increase for the copper solution is outside of the error. This result further supports the idea that migration of beads has begun to play a role at the lower ionic strength, but only in the x-direction.

Electrodeposition at the lower current and concentration in the presence of the magnet produces flow patterns in solutions of both metals (Figures 10a and e) like the corresponding patterns at the higher current and concentration. The y-component of the circulating flow is produced by the MHD and is u_y = 7.1 $\pm$ 0.8 µm/s for copper (Figure 10a) and u_y = 6.1 $\pm$ 0.8 µm/s

for lead (Figure 10e). These values are closer to each other than they were at the higher

concentration and current. This result could be explained by a weaker $F_{\nabla B}$ and therefore a

smaller magnet-induced density gradient near the chip, allowing the MHD force in both metal

solutions to produce similar velocities. In addition, the u_y value for lead, which is not

significantly affected by $F_{\nabla B}$, is 1/5th the value at the higher current, as expected, because the

current is 1/5th. However, the value for copper is greater than 1/5th, which is consistent with a

higher magnet-induced density at the chip's surface that occurs at the higher concentration. The

contribution of migration on the bead movement orthogonal to the much faster MHD flow in the

y-direction is expected to be small, if any. In addition, the MHD fluid flow facilitates charge

compensation, and thus the beads a lower migration force than in a static fluid.

Once the current is turned off in the presence of the magnet, the directions of the fluid

flow for both copper and lead solutions are similar to the cases for the higher current and

presumably for the same reasons (see Figures 10b and f). The speeds for both lead and copper

solutions at low concentrations after the current is turned off with and without the magnet are

quite similar ($|u|$=6.3 ± 0.3 µm/s and $|u|$=3.3 ± 0.3 µm/s, with the magnet, and $|u|$=6.3 ± 0.5 µm/s

and $|u|$=2.3 ± 0.2 µm/s without the magnet, respectively).

4.4.5 Fluid Motion for the Two-Band Electrode Case at "High" Concentration and Current

In the two-band configuration, the electrode that was used in the one-band case serves as

the anode and underogoes stripping of the metal that was deposited onto it; and a second,

coplanar, parallel band electrode serves as the cathode and undergoes electrodeposition. This

arrangement is capable of producing highly linear MHD flow between and parallel to the
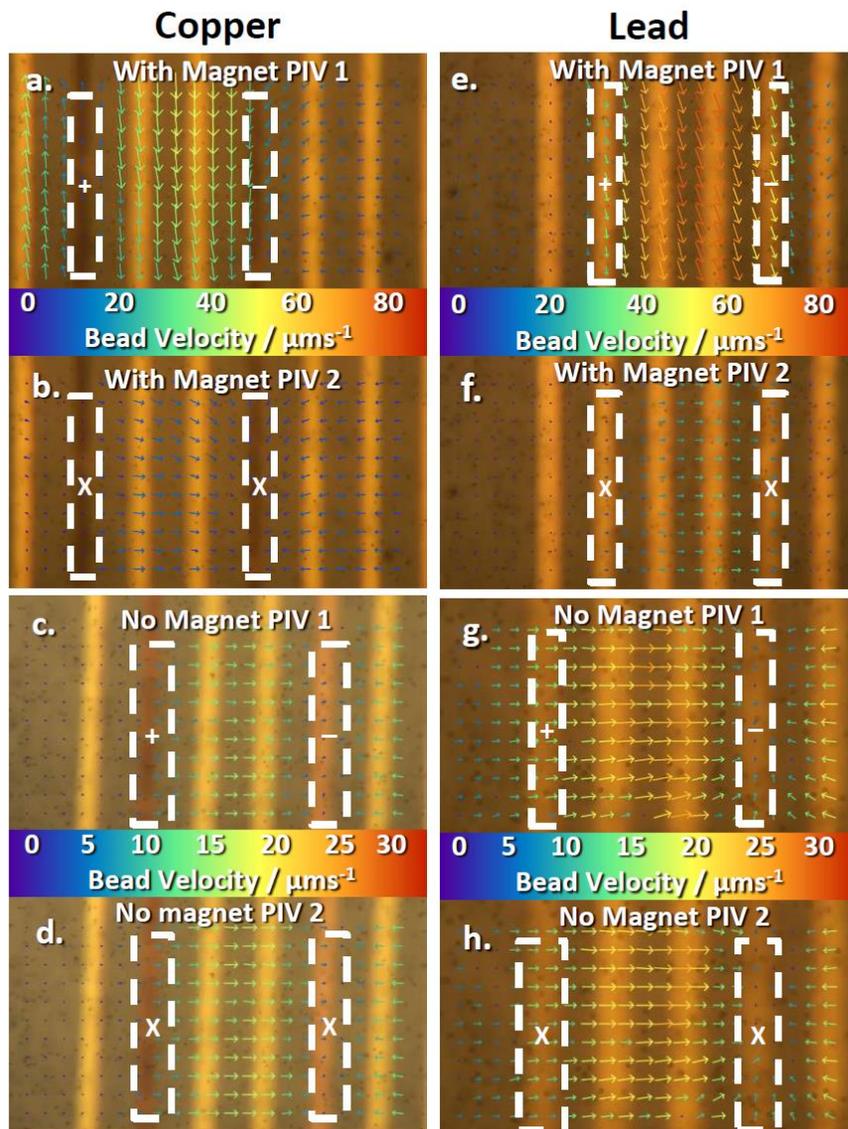
Figure 11. Microscope images superimposed with velocity vectors from PIV analysis for copper (a-d) and lead (e-h) deposition for a high concentration 95.2 mM) for the two-band case with a magnet (a and b) and without a magnet (g and h). PIV images were obtained during (a, c) and after (b, d) deposition of copper. Likewise, PIV images were obtained during (e, g) and after (f, h) deposition of lead. For PIV images taken during deposition/stripping, the velocity was measured during the last 3.3 s of the deposition. For PIV images taken after deposition/stripping, the velocity was measured for 3.3 s after the current was turned off and deposition ended. (See Figure 7c and d). Activated electrodes are outlined with dashed white lines (only ~1/5 of their entire length is shown). The cathode (-) is on the right and the anode (+) is on the left. Electrodes returned to open circuit are indicated with an "X". The anode served as the cathode in studies shown in Figure 9.

oppositely biased band electrodes in a similar small volume setup, unlike the one-band electrode case where the fluid circulates in an oval path and crosses over the electrode. Also, because the second electrode produces a density gradient, but in the opposite direction to the first, this will affect how $\mathbf{F_g}$ driven flow circulates vertically between the electrodes. Thus, convection caused by $\mathbf{F_B}$ and $\mathbf{F_g}$ can be better distinguished by using the x and y components compared to the one-band experiments and effects from $\mathbf{F_{\nabla B}}$ and $\mathbf{F_{\nabla C}}$ might be easier to determine. The PIV images are shown in Figures 11 and 12. Table 2 lists the absolute magnitudes and the x and y components of the velocities measured 200 µm from the anode.

In the absence of the magnet for the high metal concentration and current, convection due to $\mathbf{F_g}$ is observed between the two electrodes with a magnitude in the x direction of $u_x = 13 \pm 1$ µm/s for copper (Figure 11c) and $u_x = 19 \pm 2$ µm/s for lead (Figure 11g). These values are smaller than the speeds for a one-band electrode. The convection is dominated by the cathode as fluid converges from both sides directly over the electrode, which is similar to the behavior in the single-electrode case. However, there is no diverging line over the anode. Rather, there is a net flow across the anode toward the cathode. This can be explained by the more dense solution spreading outward on the chip's surface from the electrode while solution from above flows in to replace it, producing the faster horizontal velocity to the right of the anode when compared to its left. Also, for comparison, the ratio of the speeds of lead and copper solutions is 1.5. This value is slightly higher than the ratio for the single electrode at the high concentration and current.

When the current is turned off (without a magnet) for the two-band electrode case, the results are consistent with those for the one-band case. The convection continues in the same

direction as it did when the current was on, with speeds of $u_x = 15 \pm 1$ µm/s for copper (Figure 11d) and $u_x = 21.0 \pm 0.5$ µm/s for lead (Figure 11h), which are slightly higher and outside a standard deviation of the values before the current was turned off. The slightly higher velocity would be consistent with the small effect of migration on bead movement in the x direction.

With a magnet below the chip, a substantial increase in the y-component of the velocity occurs when the current is on. The speeds are much larger than for the single electrode case because the current density remains high and is mostly confined to the cross section between the activated electrodes. However, unlike the previous reports for MHD induced microfluidics [22, 23] the flow deviates from a parallel path between the two electrodes, with a substantial x-component that is 6 times greater for lead (Figure 11e, $u_x = 19 \pm 1$ µm/s) than for copper (Figure 11a, $u_x = 3 \pm 1$ µm/s). This can be attributed to the significantly greater contribution of $\mathbf{F_g}$ to the x-component of the fluid flow in the lead solution. (The contribution from density gradients to the fluid flow in the presence of a magnet is not easily noticeable in the single electrode case because of the more complicated rotational flow from MHD.) The large y-components of the velocities for lead ($u_y = 66 \pm 2$ µm/s) and copper ($u_y = 35 \pm 4$ µm/s) solutions should be due mostly to MHD. The reason for their dissimilarities can be explained by a more dense solution at the chip in the copper solution caused by $\mathbf{F_{\nabla B}}$.

When the current is turned off in the presence of the magnet, the velocity of the copper solution is, $|u| = 11.8 \pm 0.8$ µm/s (Figure 11b), and mostly in the x-direction ($u_x = 11.5 \pm 0.9$ µm/s), with a pattern of fluid flow consistent with distortion of the electrochemically generated density gradients by the previous MHD convection. Likewise, the fluid speed after the current is turned off in the lead solution ($|u| = 21.0 \pm 0.5$ µm/s, Figure 11b) with a significant x-component

(u_x= 19 ± 1 μm/s) that explains the non-parallel MHD flow when the current is on. However,

unlike the lead solution, the speed obtained with the magnet after the current is turned off in the

paramagnetic copper solution is much suppressed than that in the absence of the magnet (|u|=

11.8 ± 0.8 μm/s, Figure 11c). This suppression is further evidence of the effect of $\mathbf{F_{\nabla B}}$. (This

was not perceptible in the one-band case, because of the complicated MHD flow that

redistributes the concentration and therefore the density gradient.) Experiments at the lower

concentration and current, where $\mathbf{F_{\nabla B}}$ is weaker than the other forces should confirm whether this

interpretation is correct.

4.4.6 Fluid Motion for the Two-Band Electrode Case at "Low" Concentration and Current

In the absence of the magnet for the low metal concentration and current, convection due to $\mathbf{F_g}$

is observed between the two electrodes undergoing simultaneous electrodeposition and stripping

with a magnitude primarily in the x direction of $u_x = 3.5 ± 0.1$ μm/s for copper (Figure 12c) and

$u_x = 4.2 ± 0.3$ μm/s for lead (Figure 12g). These speeds are much slower than observed for the

higher current, due to generation of density gradients that are 1/5th as large. The ratio of the

speed for the lead solution to that of the copper solution is 1.2. For comparison, this ratio is

similar to the ratio of 1.5 for the higher current in the absence of the magnetic field. In addition,

this ratio is smaller than the average ratio from the simulation, which is 2.07, and lower than it is

for the single band electrode (2.5). The additional force from the higher density solution

spreading outward from the adjacent anode toward the cathode opposes the repulsion on the

beads from the cathode due to migration, with a greater impact on the lead solution than the

copper. Also, as in the higher current case, the flow in the x-direction in the lead solution

converges in a straight line directly over the cathode due to $\mathbf{F_g}$. However, that converging line is
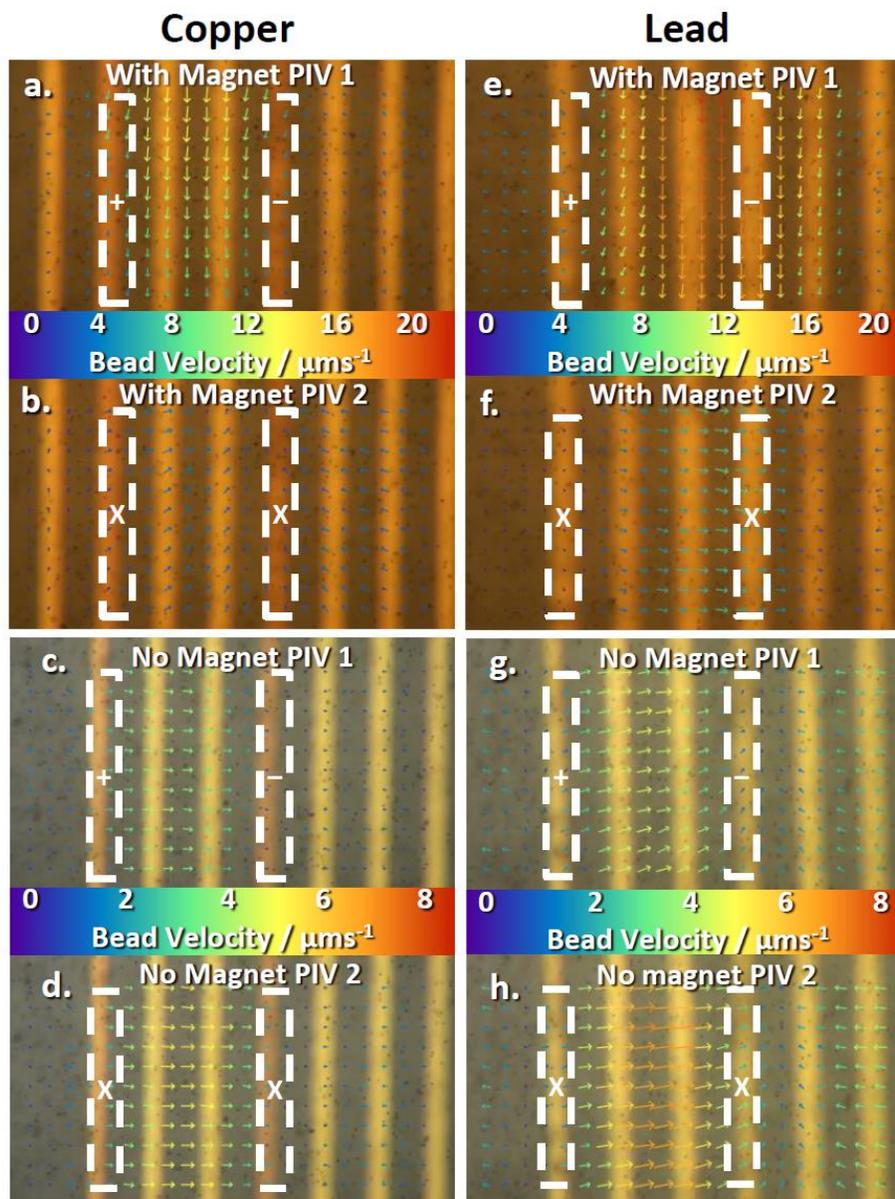
Figure 12. Microscope images superimposed with velocity vectors from PIV analysis for copper (a-d) and lead (e-h) deposition for a low concentration 9.52 mM) for the two-band case with a magnet (a and b) and without a magnet (g and h). PIV images were obtained during (a, c) and after (b, d) deposition of copper. Likewise, PIV images were obtained during (e, g) and after (f, h) deposition of lead. For PIV images taken during deposition, the velocity was measured during the last 3.3 s of the deposition. For PIV images taken after deposition, the velocity was measured for 3.3 s after the current was turned off and deposition ended. (See Figure 8c and d). Activated electrodes are outlined with dashed white lines (only ~1/8 of their entire length is shown). The cathode is on the right (-) and the anode (+) is on the left. Electrodes returned to open circuit are indicated with an "X". The anode served as the cathode in studies shown in Figure 10.

not visible for the copper solution, but this is probably because the speeds are below the measurement limit.

When the current is turned off (without a magnet), the fluid behavior is consistent with that for the higher current. The convection continues in the same direction, with speeds of $u_x = 4.9 \pm 0.1$ µm/s for copper (Figure 12d) and $u_x = 6.3 \pm 0.2$ µm/s for lead (Figure 12h), which are significantly higher than the values before the current was turned off. This is similar to the single band experiments without a magnet and is due to the influence of migration on suppressing bead movement in the x-direction when the current is on at the low concentrations.

Electrodeposition and stripping at the lower current and concentration for the two-electrode configuration in the presence of the magnet produces an MHD-dominated flow pattern in solutions of both metals (Figures 12a and e) that is much more parallel to the electrodes than for the higher current and concentration presumably because the electrochemically-induced density gradients are smaller. The y-component from MHD is $u_y = -10 \pm 2$ µm/s for copper (Figure 11a) and $u_y = -17 \pm 1$ µm/s for lead (Figure 12e). The ratio of u_y for lead solution to that of copper is 1.7 and is slightly lower than that at the higher concentration (1.9). The ratio of u_y at the lower concentration to that at the higher concentration is 0.29 for copper and 0.26 for lead, which are similar to the expected $1/5^{th}$ from the ratio of the applied currents.

Once the current is turned off in the presence of the magnet, the velocities for both copper and lead solutions continue to have a significant y-component, as did the cases with the higher current and presumably for the same reasons (see Figures 12b and f). However, the speeds ($|u|=3.3 \pm 0.3$ µm/s for copper and $|u|= 6.3 \pm 0.2$ µm/s for lead) at the lower concentration with the magnet are similar to those obtained without the magnet. This is also consistent with the

143

diminished influence of $\mathbf{F_{\nabla B}}$ at the lower concentration and current. The speed for the lead

solution to that of copper in the presence of the magnet after the current is turned off, however, is

larger, and is consistent with the larger atomic mass of lead.

4.5. Conclusion

Fluid velocity was monitored as a function of electrodeposition and stripping in solutions

of paramagnetic copper and diamagnetic lead in the presence and absence of a magnetic field, to

give insight into how the magnetoconvective forces and electrochemically generate density

gradients affect fluid movement in a microfluidic environment. Calculations were performed

using a simple model to determine the relative magnitudes of the different forces that are at play.

While the forces do not always translate into the relative magnitudes of the velocities, the

calculations revealed important aspects of the magnetoconvective systems that we could

compare with experiment. In particular, even though $\mathbf{F_{\nabla B}}$ was determined to be a smaller overall

force near the electrode, it is a substantial one everywhere else in the solution (outside the

diffusion layer). One-electrode and two-electrode configurations provided different directions

and magnitudes of the forces to help distinguish them from each other. Under the conditions

studied here, convection is dominated by $\mathbf{F_g}$ and $\mathbf{F_B}$ with contributions from $\mathbf{F_{\nabla B}}$. Evidence for

$\mathbf{F_{\nabla C}}$ was not observed. Changing the concentration and the applied current allowed the

confirmation of $\mathbf{F_{\nabla B}}$. It is enhanced by increasing concentration of paramagnetic species in the

bulk and lowering currents at the cathode. Although migration of the beads takes place at the

low concentrations where the ionic strength is substantially lower than at the high concentrations,

it is less prominent when MHD takes place and points in a different direction than the MHD. A

144

better understanding of these forces will allow them to be manipulated for future applications in microfluidics devices.

4.6. Acknowledgements

4.7. References

[1] M.C. Weston, M.D. Gerner, I. Fritsch, Magnetic Fields for Fluid Motion, Analytical Chemistry, 82 (2010) 3411-3418.

[2] S. Qian, H.H. Bau, Magneto-Hydrodynamics Based Microfluidics, Mechanics Research Communications, 36 (2009) 10-21.

[3] Z.P. Aguilar, P. Arumugam, I. Fritsch, Study of Magnetohydrodynamic Driven Flow Through LTCC Channel with Self-Contained Electrodes, Journal of Electroanalytical Chemistry, 591 (2006) 201-209.

[4] P.U. Arumugam, E.S. Fakunle, E.C. Anderson, S.R. Evans, K.G. King, Z.P. Aguilar, C.S. Carter, I. Fritsch, Characterization and Pumping - Redox Magnetohydrodynamics in a Microfluidic Channel, Journal of the Electrochemical Society, 153 (2006) E185-E194.

[5] E.A. Clark, I. Fritsch, S. Nasrazadani, C.S. Henry, Analytical Techniques for Materials Characterization, in: R.K. Ulrich, W.D. Brown (Eds.) Advanced Electronic Packaging 2nd edition, IEEE Press, Piscataway, NJ, 2006, pp. 725-791.

[6] E.C. Anderson, I. Fritsch, Factors Influencing Redox Magnetohydrodynamic-Induced Convection for Enhancement of Stripping Analysis, Analytical Chemistry, 78 (2006) 3745-3751.

[7] M.C. Weston, E.C. Anderson, P.U. Arumugam, P.Y. Narasimhan, I. Fritsch, Redox Magnetohydrodynamic Enhancement of Stripping Voltammetry: Toward Portable Analysis

Using Disposable Electrodes, Permanent Magnets, and Small Volumes, Analyst, 131 (2006) 1322-1331.

[8] M.C. Weston, C.K. Nash, I. Fritsch, Redox-Magnetohydrodynamic Microfluidics Without Channels and Compatible with Electrochemical Detection Under Immunoassay Conditions, Analytical Chemistry, 82 (2010) 7068-7072.

[9] V. Sahore, I. Fritsch, Redox-Magnetohydrodynamics, Flat Flow Profile-Guided Enzyme Assay Detection: Toward Multiple, Parallel Analyses, Analytical Chemistry, 86 (2014) 9405-9411.

[10] T. Weier, K. Eckert, S. Muhlenhoff, C. Cierpka, A. Bund, M. Uhlemann, Confinement of Paramagnetic Ions Under magnetic Field Influence: Lorentz Versus Concentration Gradient Force Based Explanations, Electrochemistry Communications, 9 (2007) 2479-2483.

[11] C. Cierpka, T. Weier, G. Gerbeth, M. Uhlemann, K. Eckert, Copper Deposition and Dissolution in Seemingly Parallel Electric and Magnetic Fields: Lorentz Force Distributions and Flow Configurations, Journal of Solid State Electrochemistry, 11 (2007) 687-701.

[12] K. Tschulik, J.A. Koza, M. Uhlemann, A. Gebert, L. Schultz, Effects of Well-Defined Magnetic Field Gradients on the Electrodeposition of Copper and Bismuth, Electrochemistry Communications, 11 (2009) 2241-2244.

[13] G. Mutschke, A. Hess, A. Bund, J. Frohlich, On the origin of horizontal counter-rotating electrolyte flow during copper magnetoelectrolysis, Electrochimica Acta, 55 (2010) 1543-1547.

[14] V. Sahore, A. Kreidermacher, I. Fritsch, Electrochemically Generated Density Gradient-Induced Natural Convection in Microfluidic Systems, Journal of Electrochemical Society, (2015) in preperation.

[15] P. Atkins, J. De Paula, Physical chemistry, 8th ed., Oxford university Press, New York, 2006.

[16] H. Sato, M. Yui, H. Yoshikawa, Ionic diffusion coefficient of Cs+, Pb2+, Sm3+, Ni2+, SeO42- and TcO4- in free water determined from conductivity measurements, J. Nucl. Sci. Technol., 33 (1996) 950-955.

[17] A.J. Bard, L.R. Faulkner, Electrochemical Methods : Fundamentals and Applications, 2nd ed ed., Wiley, New York, 2001.

[18] Y.C. Tang, A.J. Davenport, Magnetic Field Effects on the Corrosion of Artificial Pit Electrodes and Pits in Thin Films, Journal of the Electrochemical Society, 154 (2007) C362-C370.

[19] N. Leventis, X.R. Gao, Nd-Fe-B permanent magnet electrodes. Theoretical evaluation and experimental demonstration of the paramagnetic body forces, Journal of the American Chemical Society, 124 (2002) 1079-1088.

[20] N. Leventis, A. Dass, Demonstration of the Elusive Concentration-Gradient Paramagnetic Force, J. Am. Chem. Soc., 127 (2005) 4988-4989.

[21] J.M.D. Coey, F.M.F. Rhen, P. Dunne, S. McMurry, The Magnetic Concentration Gradient Force - Is it Real?, Journal of Solid State Electrochemistry, 11 (2007) 711-717.

[22] E.C. Anderson, M.C. Weston, I. Fritsch, Investigations of Redox Magnetohydrodynamic Fluid Flow at Microelectrode Arrays Using Microbeads, Analytical Chemistry, 82 (2010) 2643-2651.

[23] V. Sahore, I. Fritsch, Flat Flow Profiles Achieved with Microfluidics Generated by Redox-Magnetohydrodynamics, Analytical Chemistry, 85 (2013) 11809-11816.

[24] P.G. Scrape, M.D. Gerner, M.C. Weston, I. Fritsch, Redox-Magnetohydrodynamics for Microfluidic Control: Remote from Active Electrodes and Their Diffusion Layers, Journal of The Electrochemical Society, 160 (2013) H338-H343.

[25] M.C. Weston, I. Fritsch, Manipulating Fluid Flow on a Chip Through Controlled-Current Redox Magnetohydrodynamics, Sensors and Actuators B-Chemical, 173 (2012) 935-944.

[26] V. Sahore, I. Fritsch, Microfluidic rotational flow generated by redox-magnetohydrodynamics (MHD) under laminar conditions using concentric disk and ring microelectrodes, Microfluidics and Nanofluidics, 18 (2015) 159-166.

[27] V.M. Volgin, A.D. Davydov, Natural-Convective Instability of Electrochemical Systems: A Review, Russian Journal of Electrochemistry, 42 (2006) 567-608.

[28] J. Konig, K. Tschulik, L. Buttner, M. Uhlemann, J. Czarske, Analysis of the Electrolyte Convection inside the Concentration Boundary Layer during Structured Electrodeposition of Copper in High Magnetic Gradient Fields, Analytical Chemistry, 85 (2013) 3087-3094.

5. Different Magnet Arrangements Used to Study Magnetoconvective and Density Gradient Forces During Deposition and Stripping of Copper

5.1. Abstract

The effect of magnetoconvective and gravitational forces on fluid flow in a small volume system involving copper electrochemistry at microband electrodes on an insulated silicon chip was studied using different magnet arrangements. Copper was simultaneously deposited at one microband and stripped off another microband, which was parallel to and near the former. Different magnet arrangements cause the magnitude and gradient of the magnetic flux density to vary, altering the magnitude and direction of the magnetoconvective forces. Four possible contributions toward fluid flow were considered. The first is the magnetohydrodynamic force ($\mathbf{F_B}$), which is the magnetic component of the Lorentz force and governed by the right hand rule. The second is the magnetic gradient force ($\mathbf{F_{\nabla B}}$), which is expected to provide a significant contribution when paramagnetic species, like Cu(II), reside in a non-uniform magnetic field. The third is the paramagnetic concentration gradient force ($\mathbf{F_{\nabla C}}$), over which there is some controversy regarding its magnitude. It is present when there is a non-uniform concentration of paramagnetic species in a magnetic field, which occurs when depositing and stripping copper. Finally, the gravitational force ($\mathbf{F_g}$), which is independent of the magnetic field, and causes convection under non-uniform density conditions. In this paper, the non-uniform density is caused by Cu(II) generated into or depleted from solution adjacent to the anode and cathode, respectively.

5.2. Introduction

Different magnet arrangements were used to vary magnetic flux direction, density and gradients, thus facilitating the investigation of density gradient and magnetoconvective forces on fluid flow in small volume systems for a single redox species, copper(II), that is paramagnetic. The studies described in Chapter 4 used only one magnet configuration and compared results from solutions of different copper(II) and lead(II) concentrations to study magnetoconvective forces.

Magnetoconvection provides unique possibilities for manipulating fluid flow on a chip [1]. However, it had not been studied in small volumes confined to dimensions like those of lab-on-a-chip devices until recently. Work performed previously by others to develop micropumps to make use of the magnetic portion of the Lorentz force, the magnetohydrodynamic force (F_B), suffer from bubble formation and electrode corrosion [2]. The issue has been resolved in our laboratory by adding redox species. Convection due to redox-MHD has been shown to be useful in enhancing trace metal analysis [3-5]. It can be used to pump fluids in a microchannel [6, 7], and can also pump a fluid plug on a chip without requiring channel sidewalls [8, 9].

Other forces, including the gravitational force (F_g), the magnetic gradient force ($F_{\nabla B}$), and the paramagnetic concentration gradient force ($F_{\nabla C}$) can produce convection under experimental conditions that also produce F_B. Background, discussion, and the equations for each of the forces are provided in detail in Chapter 4. The F_g causes convection during metal deposition by the depletion of metal ions near the electrode and migration of metal ions from

farther away and cations from supporting electrolyte toward and anions away from the region to compensate charge. The result is a less dense solution that rises to the top of the cell. The opposite occurs during metal stripping when a high concentration of metal ions is produced near the electrode. The result is a more dense solution that sinks and spreads outward on the bottom of the cell. Convection due to density gradients has been studied using the ferricyanide-ferrocyanide redox couple with band electrodes (see Chapter 2), as well as disk and ring electrodes [10]. It has been shown that convection due to F_g becomes noticeable well after the start of the current (several seconds), in contrast to F_B where visible convection begins immediately at the onset of the current.

$F_{\nabla B}$ is the result of interactions between paramagnetic species and a non-uniform magnetic field [11]. The relationship between $F_{\nabla B}$ with B is complicated but usually points toward the higher magnetic flux density. Unlike other forces, $F_{\nabla B}$ exists as long as there are paramagnetic species in a non-uniform magnetic field.

$F_{\nabla C}$ is caused by a non-uniform concentration of paramagnetic species interacting with a magnetic field. Non-uniform concentration profiles of paramagnetic species are often produced during electrochemical experiments involving heterogeneous electron transfer events in the diffusion layer between the electrode and bulk solution. The paramagnetic species are drawn toward the highest concentration by $F_{\nabla C}$. The magnitude of this force and its ability to affect fluid movement is controversial, where experimental results have been interpreted to demonstrate both its impact [12, 13] and lack of impact [14].

151

In Chapter 4, experiments with applied current were conducted with paramagnetic copper(II) and diamagnetic lead(II), both with and without a disk magnet (2.54 cm diameter x 2.54 cm tall). By controlling the electronic current, unique control over the ionic current and concentration gradients was possible. The experiments were performed using two arrangements: metal deposition at a band electrode (one-band), and simultaneous deposition at one electrode and stripping at an adjacent one, parallel to the first (two-bands). The latter electrode arrangement proved more informative about the impact of the relative forces on fluid flow because the paths of $\mathbf{F_g}$ and $\mathbf{F_B}$ are more uniform and perpendicular to each other. The vast majority of the observed convection was due to $\mathbf{F_g}$ and $\mathbf{F_B}$. $\mathbf{F_{\nabla B}}$ influenced fluid flow by increasing the density, and therefore the viscosity, of the solution near the magnet. This results in suppressing convection caused by $\mathbf{F_B}$ between the cathode and anode on the floor of the cell, while suppressing $\mathbf{F_g}$ at the cathode and enhancing $\mathbf{F_g}$ at the anode. The influence that $\mathbf{F_{\nabla B}}$ has on fluid flow increases with increasing concentration of the paramagnetic species and increasing current that changes the concentration of the parmagnetic species faster. There was no evidence that $\mathbf{F_{\nabla C}}$ affected fluid flow, even though its magnitude is an order greater at the electrode surface than $\mathbf{F_{\nabla B}}$.

Here, rather than comparing fluid movement with and without magnetoconvective effects, comparisons are made for a single metal species, copper, using different magnet arrangements to create different conditions under which the different forces will dominate. The deposition and stripping of copper in a two-band configuration was used. The supporting electrolyte was sulfate instead of nitrate. (Nitrate was needed in studies involving lead in Chapter 4 because lead sulfate is insoluble in water.) By changing the arrangement of the

152

magnet, the magnetic flux direction density and gradients can be altered. As a result, the

magnitudes and directions of $\mathbf{F_B}$, $\mathbf{F_{\nabla B}}$, and $\mathbf{F_{\nabla C}}$ can be varied. The magnitude of $\mathbf{F_B}$ is

proportional to the magnitude of the magnetic flux density. The magnitude of $\mathbf{F_{\nabla C}}$ is proportional

to the square of the magnetic flux density. The magnitude of $\mathbf{F_{\nabla B}}$ is proportional to the

magnitude and gradient of the magnetic flux density. Controlling the quantity of paramagnetic

species produced or removed by the electrode as a function of time might allow further control of

$\mathbf{F_{\nabla C}}$ in the vicinity of the electrode. Here, Amperes software was used to simulate the magnetic

fields of three magnet arrangements that were used in the experiments: a single disk magnet, two

ring-shaped magnets, and one ring and one disk magnet. Fluid flow in the absence of a magnet

was also evaluated to give further insight into $\mathbf{F_g}$. The single disk magnet yields results that are

similar to those described in Chapter 4. Two ring magnets generate a magnetic field that is an

order of magnitude weaker than when a single disk magnet is used, but without vertical

gradients. One ring and one disk produce a stronger vertical gradient than the single disk magnet

arrangement. Here, we describe how different magnet arrangements and therefore different

magnetoconvective forces affect microscale systems.

5.3. Experimental

5.3.1. Chemicals and Materials.

All chemicals were reagent grade and used as received. Aqueous solutions were prepared

with high purity deionized water from Ricca Chemical Co. (Arlington, TX), resistivity

18.2 MΩ/cm. The copper sulfate was from Sigma Aldrich (St. Louis MO). The sulfuric acid

came from VWR International (Radnor, PA). The 6 μm polystyrene latex microspheres

(sulfonated, 2.5 wt% dispersion in water) were obtained from Alfa Aesar (Ward Hill, MA).

Electrical connection of the potentiostat to the contact pads on the chip was made using an edge

connector (solder contact, 20/40 position, 0.05 in. pitch) from Sullins Electronics Corp. (San
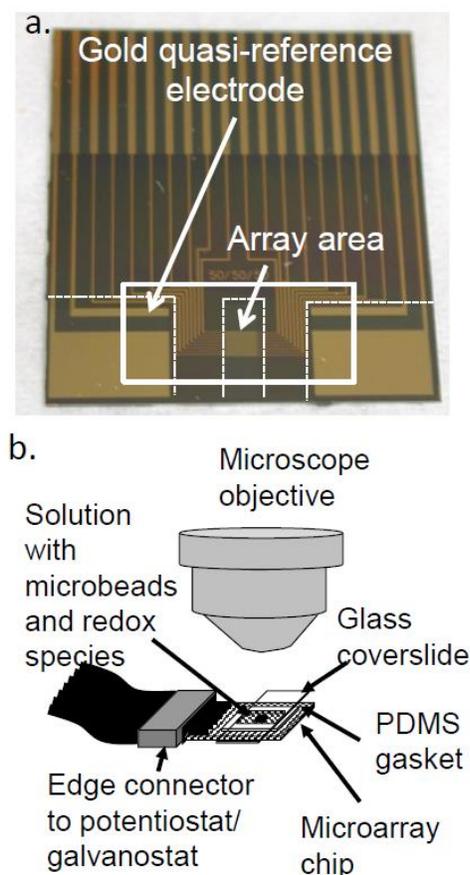
Marcos, CA).

Figure 1. (a) Microfluidic chip used in the experiments herein. The array area is patterned with 16 gold microband electrodes in the array having lengths of 2000 μm, width of 40 μm, and separated by 60 μm. There are two identical medium and large gold electrodes, and quasi-reference (used for both the electrodeposition at a single band and deposition/stripping at parallel bands) as indicated. Dashed white lines emphasize the edge of the BCB insulating layer. Solid white line defines the opening for the solution in the PDMS gasket. (b) Side view diagram of the experimental setup for the density gradient experiments.

5.3.2. Microelectrode Array Design and Fabrication.

The electrode array chips were microfabricated using the procedure reported previously [1]. The 2.54 cm × 2.54 cm silicon dioxide-coated silicon chip has sixteen 40 μm × 2000 μm gold microband electrodes with 60 μm gaps separating them. The electrodes are individually addressable through contact pads at the edge of the device. A photolithographically-patterned benzocyclobutene layer over the chip is used to define the lengths of the electrodes and insulates the leads. A diagram of the chip design can be seen in Figure 1a and a close up view of the array area can be found in Figure 1b.

5.3.3. Magnet and Magnetic Field Simulation.

There were two types of NdFeB magnets used in the studies: a disk magnet, with a height of 1.27 cm and a diameter of 3.81 cm) and a ring magnet, with a height of 1.91 cm and a diameter of 3.81 cm with a 1.91 cm hole in the center. The magnets were used in four different arrangements: (1) single disk magnet (Figure 2a), (2) two ring magnets (Figure 2b), (3) and disk and ring magnets (Figure 2c). For the single disk arrangement the magnet was directly below the chip. For the two ring magnet arrangement there was one ring below the chip and one ring above the chip. The disk and ring magnet arrangement had one disk magnet below the chip and one ring magnet above. A spacer made from layers of cardboard kept the magnets in the multiple magnet arrangements separated from each other by 5 mm. All three magnet arrangements were simulated using Amperes software (Enginia Research Inc. Winnipeg, MB, Canada). The magnetic flux density was measured using a dc magnetometer (AlfaLab Inc.) and found to be within 1% of the simulated values.
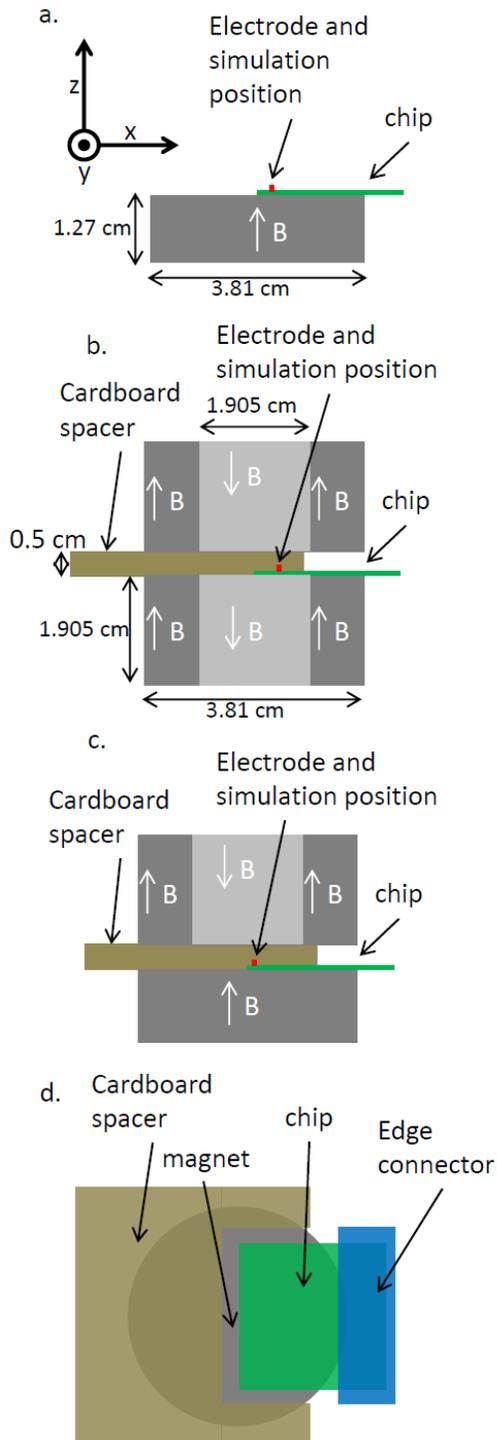
155

Figure 2. Diagram of magnet(s) and chip with the locations where the magnetic field simulations were performed and the anode is indicated for (a) single disk magnet, (b) two ring magnet, and (c) ring and disk magnet arrangements. (d) A top down view showing the location of the spacer with respect to the chip and the magnet.

5.3.4. Electrochemical Apparatus and Control.

A CHI 760B potentiostat/galvanostat (CH Instruments, Austin, TX) was used for all electrochemical experiments. The working electrode was one of the 40×2000 μm electrodes in the array. The reference electrode was the medium sized bare gold electrode, having an electroactive area of 1.88 mm^2 exposed to solution and labeled in Figure 1a.

Electrodeposition on band electrodes of the chip was performed in a beaker with a Pt flag counter electrode in a solution containing 0.1 M copper sulfate and 0.1 M sulfuric acid. A potential of -0.8 V vs. the gold quasi-reference electrode was applied for 60 s.

For experiments where deposition and stripping occurred simultaneously at oppositely biased, parallel electrodes (i.e. a two-band experiment) an 810 μm thick PDMS gasket with a rectangular opening of 5.5 mm $\times$ 12.6 mm was set on top of the chip. The outline of the opening in gasket can be seen in Figure 1a. The counter electrode was another 40×2000 μm band electrode in the array so that there were two inactive electrodes between the working and the counter. Activated electrodes are labeled in the corresponding particle image velocimetry (PIV) figures. The electrode that served as the cathode in the electrodeposition step became the anode in the two-band electrode experiment. Into the opening of the PDMS gasket, a 50 μL aliquot of a 2.5% by weight solution of 6 μm polystyrene latex beads was added to each 1000 μL volume of 0.1 M copper sulfate in 0.1 M sulfuric acid (a 1 to 20 volume ratio). This dilution produces a solution of 95.2 mM each of sulfuric acid and copper sulfate. A glass microscope slide, from VWR International (Radnor, PA), was placed on the gasket to serve as a lid and enclose the

solution, forming an electrochemical cell. The cell was placed under the microscope as shown in Figure 1b. An anodic current of 10 µA was applied to the working electrode–the one onto which copper had been deposited previously. To protect the gold electrodes, the galvanostat was set to end the run when the potential response went above 0.5 V or below -1.3 V. If the potential limit was not reached after 60 s, the applied current was ended manually. The experiments were performed in pairs with a one-band experiment to electrodeposit and a two-band experiment to obtain data and without removing the chip from the solution.

5.3.5.   Bead Video Microscopy Analysis

The bead movement was observed using a Leica DM2500 M microscope with a Leica EL6000 light source and movies were recorded using a Sony Handycam digital camera (model no. HDR-XR500V, 30 frames per second with 720×480 pixels per frame). The microscope was focused 150 µm above the chip surface for all the bead video microscopy experiments. Every tenth frame recorded in a 3.3 s video segment was extracted as a still image. The extracted frames were loaded on to DynamicStudio v.3.00 software (Dantec Dynamics, Copenhagen, Denmark) for PIV analysis as described in Scrape et al. [15].   Velocities for the parallel electrodes were measured halfway between the anode and the cathode as shown by the solid white box in Figure 3. The dashed white boxes indicate the active electrodes. Electrodes where copper has been deposited appear dark in the microscope image. Those without copper appear light. Studies with beads on a glass slide (deposited by placing a drop of bead solution on the glass slide and allowing it to dry) were used to measure a focal depth of 300 µm for the microscope used in all the experiments.

5.4. Results and Discussion

5.4.1 No Magnet

The first series of experiments did not involve a magnet. The main force contributing to the convection is $\mathbf{F_g}$, similar to the experiments described previously, (see Chapters 2 and 4) with similar results. This can be seen in Figure 3, where fluid movement near the chip surface is toward the deposition electrode (i.e. the cathode) to replace the less dense solution that has risen to the top of the cell, and fluid movement away from the anode being displaced by the more dense solution that has spread out along the floor of the cell. The average velocity of the fluid halfway between the two active electrodes is 12.4 ± 0.9 μm s^{-1}.

Table 1. Transference numbers for the ions in solution used for the parallel electrode experiments using Equation 2 from chapter 4. H$^+$ concentration was measured with a pH electrode and used along with pKa of 1.99 of the bisulfate ion [16] to get the concentration of SO$_4^{2-}$ and HSO$_4^-$

t Cu^{2+}	t H$^+$	t SO$_4^{2-}$	t HSO$_4^-$
0.0779	0.7471	0.0729	0.1022

The ferricyanide-ferrocyanide redox couple used in Chapter 2 produces smaller density gradients because both forms of the redox species remain in solution. The velocity is higher because the measurements are made closer to the electrode. Chapter 4 uses copper deposition and stripping in a nitric acid electrolyte with the same concentrations as the copper sulfate and sulfuric acid used here. Copper deposition and stripping in Chapter 4 show density gradients with a similar direction and velocity. How the change in electrolyte affects development of the density gradients depends on the transference numbers and the molecular mass of the ions. Transference numbers for the solutions in this chapter are given in Table 1.
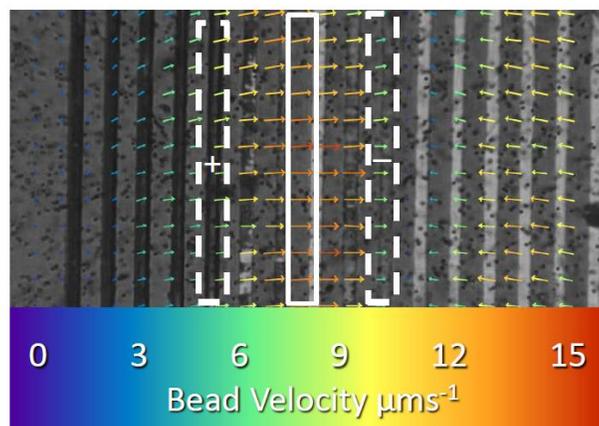
Figure 3. PIV image of bead movement superimposed on a microscope image of a portion of the electrode array during the deposition and stripping of copper in the absence of a magnet. The dashed white boxes indicate the active electrode. The solid white box shows where the velocity was measured. The section of the electrodes shown here is only 800 μm long. (Total length of electrodes is 2000 μm.)

5.4.2 Single Disk Magnet

Another arrangement is a single magnet below the chip, as illustrated in Figure 2a. The magnetic field at the center of the electrode is 0.313 T. This arrangement creates strong field gradients in the vertical direction. The magnetic field gradient in the negative z direction was calculated to be 14.1 T/m using the data from the Amperes simulation. This results in a relatively strong $\mathbf{F_{\nabla B}}$ pointing in the negative z direction when copper is used. There are small gradients, about 2.91 T/m, in the horizontal direction, causing a weaker $\mathbf{F_{\nabla B}}$ pointing toward the edges of the magnet in the horizontal direction. Figure 3b shows the simulated magnetic flux density. The plot shows a 1 mm × 2 mm area with the working electrode positioned on the bottom and the

160

solution above it. The x component of **B,** B_x**,** is in Figure 4a, the y component, B_y, in Figure 4b,

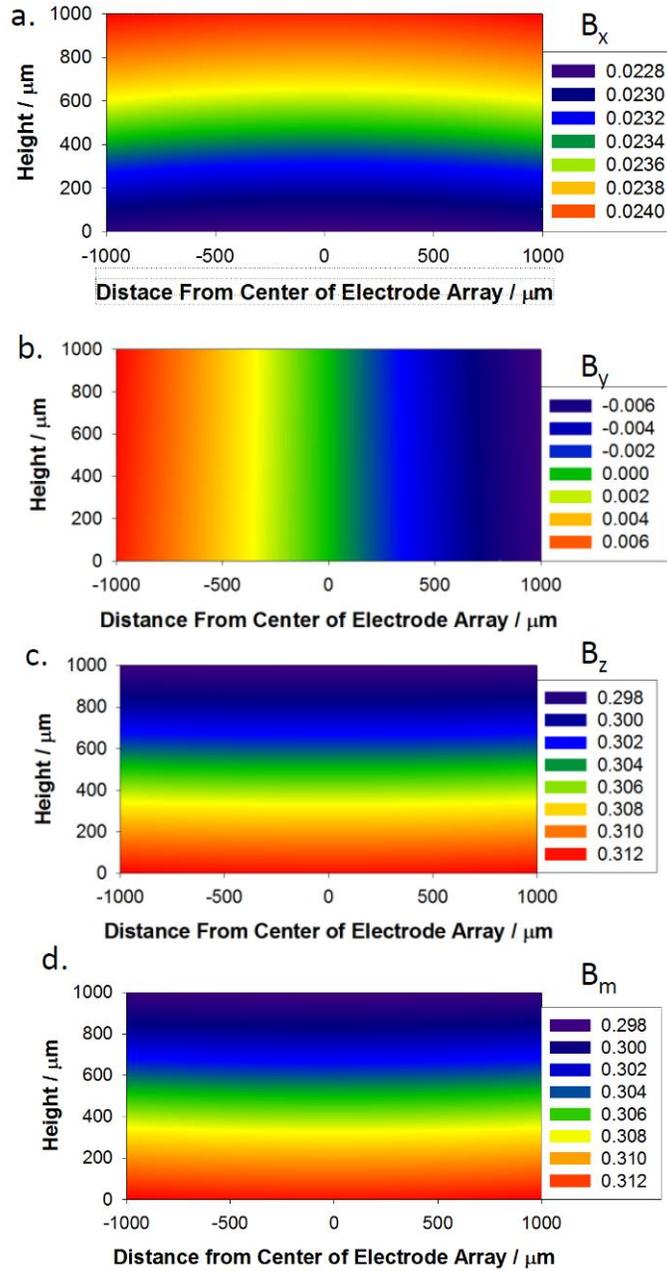the z component, B_z, in Figure 4c, and the magnitude $|\mathbf{B}| = B_M$ in Figure 4d.

Figure 4. Disk magnet arrangement. (a) The magnetic flux density in the x, direction (b) The
magnetic flux density in the y, direction. (c) The magnetic flux density in the z, direction. (d)

Plot of the magnitude of the magnetic flux density created using an Amperes simulation. The x axis in the plots is the y axis in the diagram in Figure 2a. Both the electrode and the magnet are centered in x axis of the graph (y axis in figure 2a).
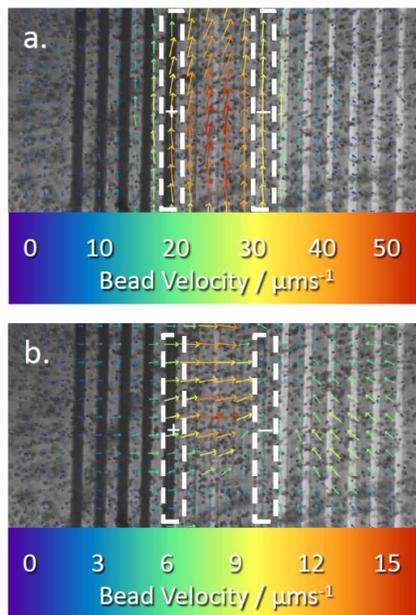

Figure 5. PIV images for a two-electrode experiment in a copper solution with the disk magnet arrangement: (a) during, and (b) after deposition and stripping. PIV images are superimposed on a microscope image of the array, where the length shown is 800 μm.

Parallel electrode experiments show a reinforcing flow pattern caused by $\mathbf{F_B}$ while deposition and stripping is occurring. The fluid moves in the negative y direction (downward in the figure) with a velocity of the fluid halfway between the two active electrodes of 44 ± 4 μms^{-1}. This can be seen in the PIV image in Figure 5a. Studies with a different disk in Chapter 4 magnet resulted in a velocity of 31 ± 3. The difference is most likely the result of the velocity being measured in a different location relative to the active electrodes. This different location does not affect the density gradient velocities as seen in the no magnet arrangement and with the disk magnet when deposition and stripping has stopped. Fluid movement caused by density gradients at 10 ± 3 μm s^{-1} can be easily observed after current has stopped in Figure 5b, with similar

direction and slightly slower velocity (although not outside of error) to the no magnet

arrangement. This would indicate that the effect of $\mathbf{F_{\nabla B}}$ on convection is not measurable outside

of error in this case. The previous disk magnet studies in Chapter 4 show a decrease in speed

with $(11 \pm 1 \ \mu ms^{-1})$, when compared to the no magnet results $(15 \pm 1 \ \mu ms^{-1})$ caused by $\mathbf{F_{\nabla B}}.$

The different result can be attributed to the different magnets used. The magnet used in Chapter

4 had a much higher flux density (0.4833 T) and gradient in the negative z direction (42.1 T/m).

The result is that $\mathbf{F_{\nabla B}}$ is approximately five times larger in Chapter 4.

5.4.3 Two Ring Magnets

An alternative to the single magnet arrangement is with a pair of ring magnets placed

above and below the chip as shown in Figure 2b. According to the simulation, this arrangement

produces no magnetic field gradients in the z direction and as a result, $\mathbf{F_{\nabla B}}$ is zero in that

direction. Field gradients of 28.4 T/m in the horizontal direction cause $\mathbf{F_{\nabla B}}$ in the direction

pointing away from the center of the hole in the magnet, with very similar magnitude, due to the

complicated relationship $\mathbf{F_{\nabla B}}$ has with $\mathbf{B}.$ The magnetic field, 0.0306 T at the center of the

electrode, is an order of magnitude weaker than the single magnet arrangement. As a result, $\mathbf{F_B}$ is

an order of magnitude weaker, while $\mathbf{F_{\nabla C}}$ is two orders of magnitude weaker due to its second

order dependence on the magnetic flux density. The magnetic flux reverses direction in the holes,

which reverses $\mathbf{F_B}.$ Plots of simulated B_x, B_y, B_z, and B_M are shown in Figure 6.

Parallel electrode experiments show both reinforcing flow and flow caused by density

gradients while deposition and stripping occurs as demonstrated in Figure 7a. The velocity is

also slower due to the decreased magnetic flux density at $10 \pm 1 \ \mu m \ s^{-1}$, and in the opposite
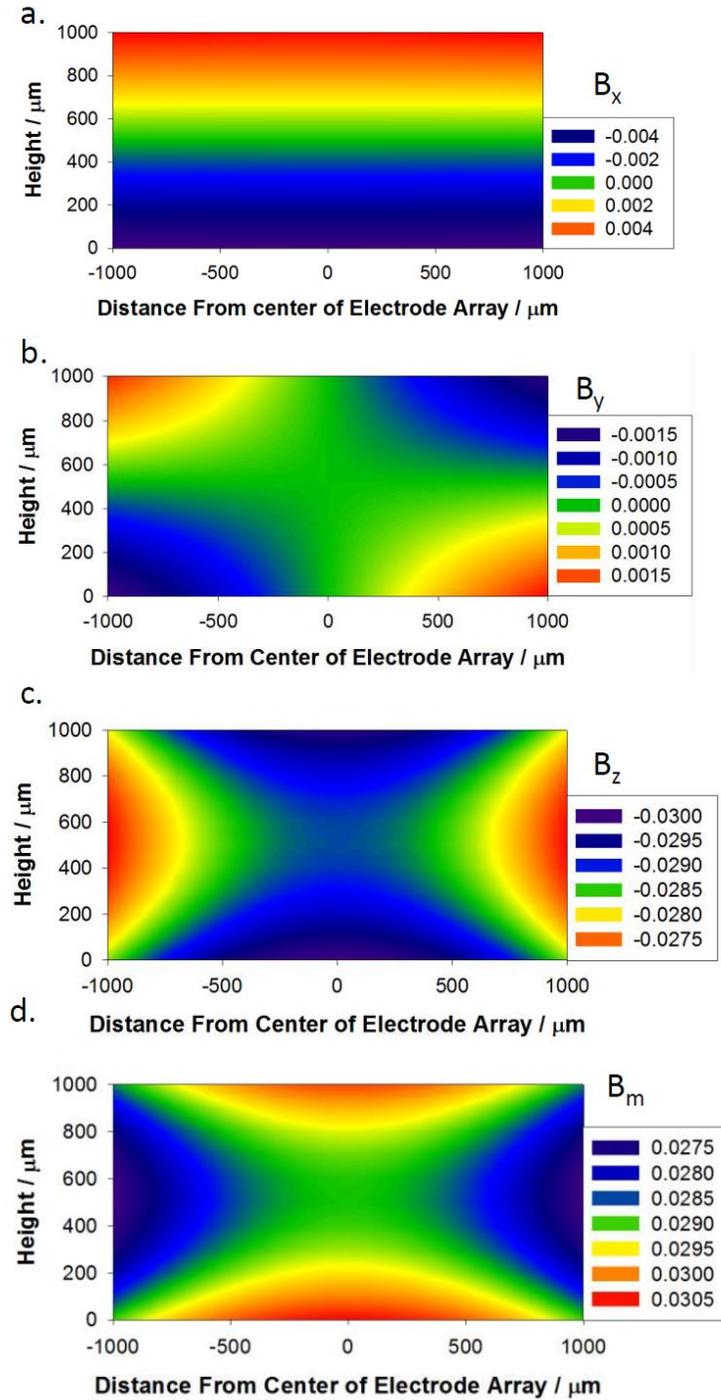
Figure 6. Two ring magnet arrangement. (a) The magnetic flux density in the x direction. (b) The magnetic flux density in the y, direction. (c) The magnetic flux density in the z, direction. (d) Plot of the magnitude of the magnetic flux density created using an Amperes simulation. The x axis in the plots is the y axis in the diagram in Figure 2b.

direction due to the magnetic field reversing direction in the hole of the magnet. The speed is

higher than the expected based on the order of magnitude difference in magnetic flux density.

This is the result of density gradient based motion that also occurs. When deposition and

stripping is stopped, fluid movement caused by density gradients continues and is observed, with

a lower velocity than the cases without the magnet and with the disk magnet, with a velocity of

5 ± 2 µm s^{-1}. This can be seen in the PIV image in Figure 7b. The lower velocity after current is

mostly due to the convection during current altering the density gradients. This can be seen with

the disk magnet, although it is not as dramatic, and is discussed in Chapter 4. In addition $\mathbf{F_{\nabla B}}$ in

the horizontal direction would pull copper solution towards the anode and increase the velocity

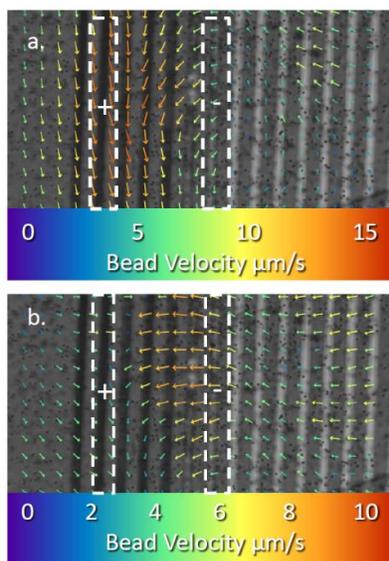reducing the effect of convection when the current is being applied.

Figure 7. PIV images for a two-electrode experiment in a copper solution with the two-ring magnet arrangement: (a) during, and (b) after deposition and stripping. PIV images are superimposed on a microscope image of the array, where the length shown is 800 µm.
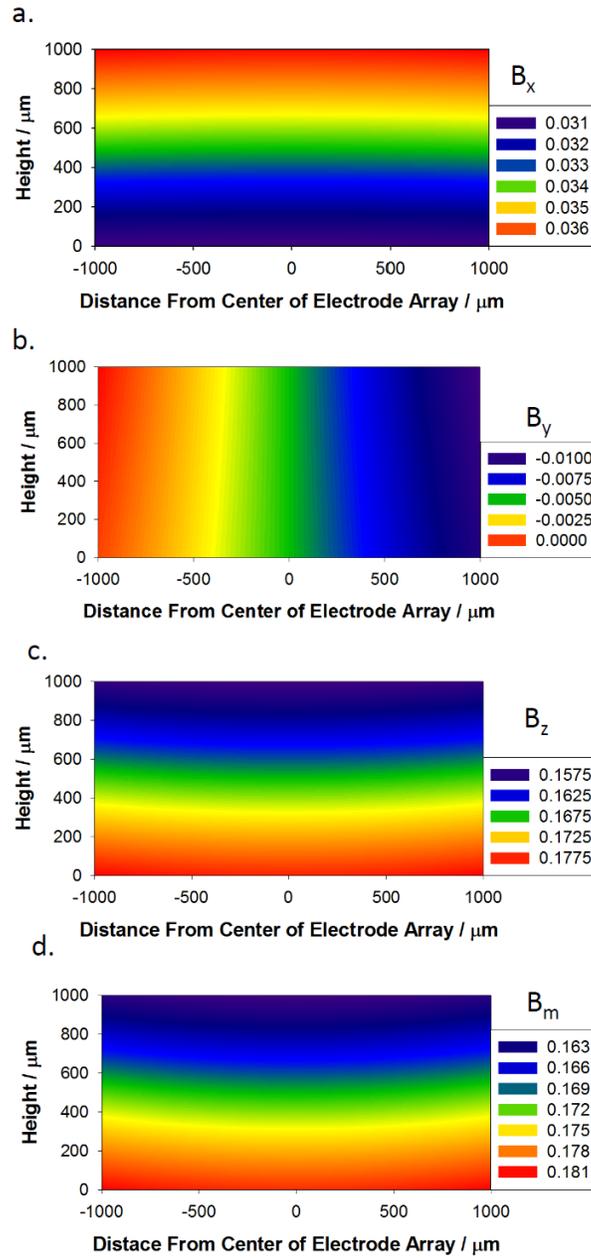
5.4.4 Ring and Disk Magnets

Figure 8. Disk and ring magnet arrangement. (a) The magnetic flux density in the x, direction. (b) The magnetic flux density in the y, direction. (c) The magnetic flux density in the z, direction. (d) plot of the magnitude of the magnetic flux density created using an Amperes simulation. The x axis in the plots is the y axis in the diagram in Figure 2c.

When a ring magnet is placed above and a disk magnet is placed below the chip, as illustrated in Figure 2c. The magnetic field gradients in the z direction are 31% stronger than the single disk magnet arrangement. As a result of the complicated relationship $\mathbf{F_{\nabla B}}$ has with $\mathbf{B}$, $\mathbf{F_{\nabla B}}$ actually decreases by 50% in the z direction. According to the simulation the magnetic field gradient in the negative z direction is 20.37 T/m. There is a gradient in the horizontal direction of 2.42 T/m pointing away from the center of the magnet. The magnetic field, at 0.180 T at the center of the electrode, is 42% weaker than the single magnet arrangement; as a result, $\mathbf{F_B}$ is 42% weaker and $\mathbf{F_{\nabla C}}$ and is 67% weaker. Figure 8 shows the simulated values of B_x, B_y, B_z, and B_M.
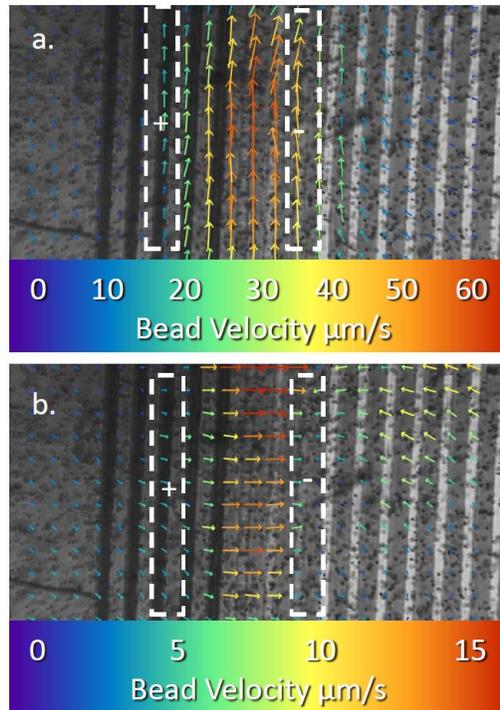

Figure 9. PIV images for a two-electrode experiment in a copper solution with the one-ring and one-disk magnet arrangement: (a) during, and (b) after deposition and stripping. PIV images are superimposed on a microscope image of the array, where the length shown is 800 μm.

Copper deposition and stripping experiments show reinforcing flow, similar to the disk magnet arrangement. The direction and speed (47 ± 7 μms^{-1}) are not significantly different from the disk magnet. See Figure 9a. When deposition and stripping stops, the density gradient based fluid movement is easily observable, as seen in Figure 9b. The direction and speed, at 11 ± 1 μm s^{-1}, are not significantly different from those for the disk magnet case. The 50% decrease in $\mathbf{F_{\nabla B}}$ in the z direction does not appear to affect fluid flow.

5.5. Conclusions

A parallel paired electrode configuration, one depositing and one stripping, with different magnet arrangements was used to gain insight into how the magnetoconvective forces effect fluid movement in a microfluidic environment. The convection is dominated by $\mathbf{F_g}$ and $\mathbf{F_B}$, and no visible contribution to fluid flow from $\mathbf{F_{\nabla C}}$. Unlike the results in Chapter 4, $\mathbf{F_{\nabla B}}$ is too weak to cause significnat change in convention in any of the magnet arrangements. The single disk magnet and ring and disk magnet arrangements show only a reinforcing flow pattern caused by $\mathbf{F_B}$ while deposition and stripping is occurring and fluid movement caused by density gradients occurs after the current has ended. The two-ring magnet arrangement shows a density gradient during the current due to the diminished magnetoconvective forces.

5.6. Acknowledgments

the major research component of the Arkansas Tobacco Settlement Proceeds Act of 2000. The use of the High Density Electronics Center microfabrication facilities is also acknowledged.

5.7. References

[1] M.C. Weston, M.D. Gerner, I. Fritsch, Magnetic Fields for Fluid Motion, Analytical Chemistry, 82 (2010) 3411-3418.

[2] S. Qian, H.H. Bau, Magneto-Hydrodynamics Based Microfluidics, Mechanics Research Communications, 36 (2009) 10-21.

[3] E.A. Clark, I. Fritsch, S. Nasrazadani, C.S. Henry, Analytical Techniques for Materials Characterization, in: R.K. Ulrich, W.D. Brown (Eds.) Advanced Electronic Packaging 2nd edition, IEEE Press, Piscataway, NJ, 2006, pp. 725-791.

[4] E.C. Anderson, I. Fritsch, Factors Influencing Redox Magnetohydrodynamic-Induced Convection for Enhancement of Stripping Analysis, Analytical Chemistry, 78 (2006) 3745-3751.

[5] M.C. Weston, E.C. Anderson, P.U. Arumugam, P.Y. Narasimhan, I. Fritsch, Redox Magnetohydrodynamic Enhancement of Stripping Voltammetry: Toward Portable Analysis Using Disposable Electrodes, Permanent Magnets, and Small Volumes, Analyst, 131 (2006) 1322-1331.

[6] Z.P. Aguilar, P. Arumugam, I. Fritsch, Study of Magnetohydrodynamic Driven Flow Through LTCC Channel with Self-Contained Electrodes, Journal of Electroanalytical Chemistry, 591 (2006) 201-209.

[7] P.U. Arumugam, E.S. Fakunle, E.C. Anderson, S.R. Evans, K.G. King, Z.P. Aguilar, C.S. Carter, I. Fritsch, Characterization and Pumping - Redox Magnetohydrodynamics in a Microfluidic Channel, Journal of the Electrochemical Society, 153 (2006) E185-E194.

[8] M.C. Weston, C.K. Nash, I. Fritsch, Redox-Magnetohydrodynamic Microfluidics Without Channels and Compatible with Electrochemical Detection Under Immunoassay Conditions, Analytical Chemistry, 82 (2010) 7068-7072.

[9] V. Sahore, I. Fritsch, Redox-Magnetohydrodynamics, Flat Flow Profile-Guided Enzyme Assay Detection: Toward Multiple, Parallel Analyses, Analytical Chemistry, 86 (2014) 9405-9411.

[10] V. Sahore, A. Kreidermacher, I. Fritsch, Electrochemically Generated Density Gradient-Induced Natural Convection in Microfluidic Systems, Journal of Electrochemical Society.

[11] Y.C. Tang, A.J. Davenport, Magnetic Field Effects on the Corrosion of Artificial Pit Electrodes and Pits in Thin Films, Journal of the Electrochemical Society, 154 (2007) C362-C370.

[12] N. Leventis, X.R. Gao, Nd-Fe-B permanent magnet electrodes. Theoretical evaluation and experimental demonstration of the paramagnetic body forces, Journal of the American Chemical Society, 124 (2002) 1079-1088.

[13] N. Leventis, A. Dass, Demonstration of the Elusive Concentration-Gradient Paramagnetic Force, J. Am. Chem. Soc., 127 (2005) 4988-4989.

[14] J.M.D. Coey, F.M.F. Rhen, P. Dunne, S. McMurry, The Magnetic Concentration Gradient Force - Is it Real?, Journal of Solid State Electrochemistry, 11 (2007) 711-717.

[15] P.G. Scrape, M.D. Gerner, M.C. Weston, I. Fritsch, Redox-Magnetohydrodynamics for Microfluidic Control: Remote from Active Electrodes and Their Diffusion Layers, Journal of The Electrochemical Society, 160 (2013) H338-H343.

[16] Activity Coefficients of Acids, Bases, and Salts in CRC Handbook of Chemistry and Physics, 96th Edition (Internet Version 2016), in: M. Haynes W (Ed.), CRC Press/Taylor and Francis, Boca Raton, FL, 2015.

6. Conclusions and Future Work

6.1. Conclusion

The results described in this dissertation give valuable insight into the extent that magnetoconvective forces (the magnetohydrodynamic force, $\mathbf{F_B}$, the magnetic gradient force, $\mathbf{F_{\nabla B}}$, and the paramagnetic concentration gradient force, $\mathbf{F_{\nabla C}}$) and those due to electrochemically generated density gradients ($\mathbf{F_g}$) influence fluid flow in small volume systems. The approach taken was to follow the impact of these forces on both the electrochemical response and the fluid flow.

The effects of convection induced by electrochemically generated density gradients were studied with band microelectrodes and using the ferri-ferrocyanide redox couple in a microfluidic environment. Because fluid movement was visualized during the electrochemical experiments, a better understanding of natural convection was possible. We have found that for electrodes of smaller dimensions, natural convection occurs for lower concentrations, and at shorter time scales than previously reported by monitoring current alone. Increases in fluid velocity tracks increases in current, whether it is produced by increased concentration or electrode size at a mass-transport limited applied potential, or by directly applying a constant current. However, the velocity does not necessarily scale linearly with current. The complex interplay of factors can explain these results. For example, mass transfer dominated by diffusion at early times is influenced by natural convection at later times. Also, the transference numbers also evolve while concentration gradients develop. There is also a change in viscosity that will accompany increases in density that will alter the localized fluid velocities. In addition, the close proximity of the lid of the cell plays an important role in determining the overall fluid circulation. Computer simulations of these systems are especially needed for a more quantitative

171

understanding. Nonetheless, these multiple factors provide a great deal of flexibility in tuning the magnitude of convection for microfluidic applications.

To get a better understanding of the various forces involved, it is important to get accurate measurements of fluid movement in all three dimensions. This can be accomplished with the combination of bead video microscopy and fluorescence correlation spectroscopy (FCS) and was demonstrated at microband electrodes in a small volume containing ferri- and ferrocyanide redox species in the solution, both with and without the presence of a magnetic field. The FCS can give a high resolution 3D map of the fluid movement with measurements conducted as close as 1 μm apart. Theoretically, the beads can be as close as 200 nm in the horizontal directions and 1 μm in the vertical direction without overlap of the focal regions. Time is the limiting factor in the resolution of the FCS measurements because the points are measured one at a time. In addition, the direction of the movement cannot be determined with FCS alone. Bead video microscopy can offset these limitations by giving 2D fluid velocity information over a large area with directional information and lower resolution. Combining the two methods can give us a more complete picture of fluid movement in microfluidic systems than the methods individually by using bead video microscopy over a large area and FCS to sample fluid speed with high resolution in small sections that are of particular interest.

By using copper and lead deposition and stripping at microelectrodes, further insight into how magnetoconvective forces affect fluid movement in a microfluidic environment has been achieved. One-electrode and two-electrode configurations provided different directions and magnitudes of the forces to help distinguish them from each other. Also, the paramagnetic copper(II) and diamagnetic lead(II) allowed forces that depend strongly on magnetic

susceptibility, $\mathbf{F_{\nabla B}}$ and $\mathbf{F_{\nabla C}}$, to be compared. Under the conditions studied here, convection is dominated by $\mathbf{F_g}$ and $\mathbf{F_B}$ with small contributions from $\mathbf{F_{\nabla B}}$. Evidence for $\mathbf{F_{\nabla C}}$ was not observed. Changing the concentration and the applied current allowed the confirmation of $\mathbf{F_{\nabla B}}$. A better understanding of these forces will allow them to be manipulated for future applications in microfluidics.

Different magnet arrangements were used with the two-band electrode configuration in a copper solution to gain insight into how $\mathbf{F_{\nabla B}}$, $\mathbf{F_{\nabla C}}$, $\mathbf{F_B}$, and $\mathbf{F_g}$ affect fluid movement by altering the magnitude, direction, and gradients of the magnetic field. A disk magnet arrangement as well as the ring and disk magnet arrangement show convection while the current was on and immediately after the current was turned off, similar to the two-band electrode experiment using copper with a disk magnet from Chapter 4. The two-ring magnets show convection caused by density gradients during the current due to the decreased magnetoconvective forces. Fluid movement for all three magnet arrangements appears to be the result of, $\mathbf{F_B}$ and $\mathbf{F_g}$ only, the impact of $\mathbf{F_{\nabla B}}$ in these arrangements was too weak to affect fluid movement.

6.2. Future work

The problem with comparing magnetoconvection in solutions of copper and lead is the more than three fold difference in molecular weight, which leads to correspondingly different density gradients and values of $|\mathbf{F_g}|$. Decreasing the current for the lead solution to decrease $|\mathbf{F_g}|$, so that this force is similar for both copper and lead solutions would allow a means to better determine its contribution to fluid flow compared to the other forces. If we use a 10 μA applied current for copper, and assume the atomic weight of metal deposited or stripped is proportional to $\mathbf{F_g}$, then we can get a rough estimate that the applied current for lead should be 3.07 μA so that

this force is the same in both situations. The way to determine if $\mathbf{F_g}$ is equal is to run the experiment with no magnet to determine if the velocity for copper and lead are the same. The experiment can be run with a magnet to get a better idea of the relative contributions from $\mathbf{F_{\nabla B}}$, and $\mathbf{F_{\nabla C}}$

This proposed experiment as well as the experiments in this dissertation could be complemented by simulations that calculate the magnitude and direction of the forces necessary to match the velocity measurements, giving further insight on how the various forces manipulate fluid flow. COMSOL muitiphysics software can accomplish this. It has been used to simulate electrochemical responses [1], and can do so in a microfluidic setting [2].

Simulations of convection caused by $\mathbf{F_B}$ [3, 4] and $\mathbf{F_g}$ [5] separately have been reported; they have also been simulated together for copper deposition [6, 7]. The simulation of all the forces including $\mathbf{F_{\nabla B}}$ and $\mathbf{F_{\nabla C}}$ for the deposition of copper has been conducted by Lioubashevski et.al. [8] The simulation of diamagnetic lead and the comparison to paramagnetic ions can also be made using the simulations. The problem is that the contribution to fluid movement from all four forces must be calculated simultaneously because the interactions between the forces have to be taken into account. In addition, the effects of diffusion and migration near the electrode will also have to be taken into account, complicated by the effects of $\mathbf{F_B}$, $\mathbf{F_g}$, $\mathbf{F_{\nabla B}}$, and $\mathbf{F_{\nabla C}}$.

6.3. References

[1] E.J.F. Dickinson, H. Ekstrom, E. Fontes, COMSOL Multiphysics (R) : Finite element software for electrochemical analysis. A mini-review, Electrochemistry Communications, 40 (2014) 71-74.

[2] A.E. Khabbazi, A.J. Richards, M. Hoorfar, Numerical study of the effect of the channel and electrode geometry on the performance of microfluidic fuel cells, J. Power Sources, 195 (2010) 8141-8151.

[3] K.M. Isaac, C. Gonzales, D. Sen, Modeling of redox electrochemical MHD and three-dimensional CFD simulations of transient phenomena in microfluidic cells, Microfluidics and Nanofluidics, 17 (2014) 943-958.

[4] C. Amatore, C. Pebay, L. Thouin, A.F. Wang, J.S. Warkocz, Difference between Ultramicroelectrodes and Microelectrodes: Influence of Natural Convection, Analytical Chemistry, 82 (2010) 6933-6939.

[5] V.M. Volgin, A.D. Davydov, Numerical simulation of natural convection of electrolyte solution with three types of ions in the electrochemical cell with vertical electrodes, Russian Journal of Electrochemistry, 46 (2010) 1360-1372.

[6] G. Mutschke, A. Hess, A. Bund, J. Frohlich, On the origin of horizontal counter-rotating electrolyte flow during copper magnetoelectrolysis, Electrochimica Acta, 55 (2010) 1543-1547.

[7] S. Muhlenhoff, G. Mutschke, D. Koschichow, X.G. Yang, A. Bund, J. Frohlich, S. Odenbach, K. Eckert, Lorentz-force-driven convection during copper magnetoelectrolysis in the presence of a supporting buoyancy force, Electrochimica Acta, 69 (2012) 209-219.

[8] O. Lioubashevski, E. Katz, I. Willner, Effects of magnetic field Directed orthogonally to Surfaces on electrochemical processes, J. Phys. Chem. C, 111 (2007) 6024-6032.